

**Molecular Dynamics Study of Stability
of Intramolecular Hydrogen Bonding
Structure of Malonaldehyde in Solution
and Its Quantum Reaction Dynamics of
Proton Transfer**

Hidekazu KOJIMA

CONTENTS

I. GENERAL INTRODUCTION	6
II. METHOD	14
A. Molecular dynamics calculations of free energy surface for rotamers.....	14
1. Extension of torsional force field based on OPLS-aa.....	14
2. Free energy calculations	15
2-1. <i>Thermodynamic integration method</i>	15
2-2. <i>Umbrella sampling method</i>	16
B. Molecular dynamics calculations of proton transfer reaction in solution	16
1. Equation of motion	16
1-1. <i>Reaction coordinate</i>	16
1-2. <i>Hamiltonian</i>	18
1-3. <i>Equation of motion</i>	19
1-3-1. <i>Mixed quantum-classical approximation</i>	19
1-3-2. <i>Fully classical approximation</i>	21
2. Potential model of solute	21
3. Numerical representation of wave function in QCMD	22
4. Analysis	23
III. AN IMPROVED TORSIONAL FORCE FIELD FOR <i>CIS</i> -ENOL MALONALDEHYDE.....	33
A. Introduction.....	33
B. <i>Ab initio</i> molecular orbital calculations.....	33
C. Results and discussion	34
IV. FREE ENERGY SURFACE FOR ROTAMERS OF <i>CIS</i> -ENOL MALONALDEHYDE IN WATER.....	43
A. Introduction.....	43

B. Molecular dynamics calculations	43
C. Results and discussion	45
1. Reliability of the free energy calculations	45
2. Contribution of intramolecular vibrations to the free energy	46
3. Stability in water and in vacuum	46
4. Stability of the rotamer I	47
D. Conclusion	47
V. INTRAMOLECULAR PROTON TRANSFER REACTION OF MALONALDEHYDE IN WATER	55
A. Introduction	55
B. Molecular dynamics calculations	55
C. Results and discussion	56
1. Examples of trajectory of reaction	56
<i>1-1. FCMD calculation</i>	56
<i>1-1-1. Thermal activation reaction</i>	57
<i>1-1-2. Barrier vanishing reaction</i>	58
<i>1-2. QCMD calculation</i>	59
<i>1-2-1. Tunneling reaction</i>	59
<i>1-2-2. Thermal activation reaction</i>	60
<i>1-2-3. Barrier vanishing reaction</i>	61
2. Statistics of the reaction	62
<i>2-1. Potential energy curve in solution and its thermal fluctuation</i>	62
<i>2-2. Reaction rates</i>	64
<i>2-3. Reaction mechanisms</i>	66
D. Conclusion	67
VI. INTRAMOLECULAR PROTON TRANSFER REACTION OF MALONALDEHYDE IN NON-POLAR SOLVENT.	84

A. Introduction	84
B. Molecular dynamics calculations	84
C. Results and discussion	85
1. Reaction trajectories	85
<i>1-1. FCMD</i>	85
<i>1-2. QCMD</i>	86
<i>1-2-1. Tunneling reaction</i>	86
<i>1-2-2. Thermal activation reaction</i>	87
<i>1-2-3. Comparison with the fluctuations in water</i>	88
2. The reaction potential energy curve in neon	89
<i>2-1. Shape</i>	89
<i>2-2. Barrier height and ZPE difference</i>	89
3. Reaction rate	91
<i>3-1. Definition of reaction</i>	91
<i>3-2. Reaction rate</i>	92
4. Reaction mechanism	94
<i>4-1. Tunneling reaction</i>	94
<i>4-2. Thermal activation reaction and barrier vanishing reaction</i>	96
<i>4-3. Hydration structure</i>	97
D. Conclusions	98
VII. CONCLUSION	115
ACKNOWLEDGEMENTS	118
APPENDIX	119
A. Equation of motion of mixed quantum-classical molecular dynamics	119
B. Potential model	121
1. Effective one-dimensional potential energy curve of solute	121

2. Solute-solvent and solvent-solvent interactions.....	123
C. Division of potential energy curve into reactant and product wells	124
1. Recipe of the division V_0 into V^R and V^P	124
2. Detail of the procedure of the division	125
REFERENCES.....	129
LIST OF PUBLICATIONS.....	133

I. GENERAL INTRODUCTION

Most chemical reactions utilized in industry and living cells occur in solution. Among various chemical reactions, proton transfer reactions are one of the very important reactions found, for example, in biomolecular systems such as proton pump in bacteriorhodopsin [1] and in polymer electrolyte fuel cell, that is, proton transportation from anode to cathode through ion exchange membranes [2]. Furthermore, artificial proton pumps mimicking natural photosynthesis have been studied for production of energy [3, 4].

Chemical reactions in solution, including proton transfer reaction, may be described generally by the transition from a reactant state to a product state on a double-well potential. The potential in solution is perturbed by solute-solvent interactions and thus it is a function of time. From a view point of the mechanism, reaction occurs by thermal activation going over the potential barrier, and by tunneling through the barrier by penetration of quantum wave function. The reaction rate depends much on the solvent, however, little has been clarified about the molecular mechanism of the reaction, in particular, from a view point of the interaction with the solvent.

Solvent effect has been traditionally investigated through the relation between reaction rate and statistical properties of the solvents, i. e. dielectric constant. Reaction models described by the transition state theory [5] and the Marcus theory [6] have been explaining various reactions in solution. In the transition state theory, height of the transition state between the reactant well and the product one is essential for the reaction. This theory has been improved to incorporate quantum effect such as zero point energy or tunneling effect in the framework of variational transition state theory [7-10]. In the Marcus theory, on the other hand, destabilization of the reactant state by the fluctuation of the solvation structure which equalizes the energies of the reactant and the product is essential for the reaction. This reaction model was first applied to the electron transfer reactions and, then, it was also applied to the proton transfer reactions [11]. In these reaction theories, the solvent is

implicitly included in the reaction dynamics. Thus, molecular picture of the reactions described by the solvent dynamics cannot be obtained within the framework of these theories.

Molecular dynamics calculations provide dynamics of the reacting systems at a molecular level by numerically solving equation of motion of atoms. Using this method, chemical reactions in solution have been investigated. Since 1980, all degrees of freedom were treated classical mechanically in order to investigate reaction dynamics, e.g. S_N2 reaction [12-14]. After that, mixed quantum-classical approximation, in which a few degrees of freedom are treated quantum mechanically and the others classical mechanically, was proposed and has been applied to the proton transfer reactions [19-25].

There are two types of mixed quantum classical molecular dynamics calculations. In the first type of the calculations, the system is described by linear combination of all quantum state [19-21]. The packet is dispersed by the interactions with the solvent and finally occupies simultaneously both reactant and product wells. In the second one the system is described by an eigen state in a double well potential [22-25]. In the eigen state, the system of interest is found in both in the reactant and product states. In these two representations, the picture is not in accordance with the chemical reaction.

Yamada and Okazaki proposed an equation of motion based upon the mixed quantum classical approximation where the quantum system is found in an eigen state in either of the reactant and product states [26,27]. When electronic excited state is not important, the reactant and product states are described by an adiabatic double well potential in the electronic ground state and, then, the double well potential was divided into two single potential wells, i.e. the reactant well and the product one [27]. Combining this equation with the surface-hopping approximation, in which the quantum system occupying one eigen quantum state at one time interacts with solvent, the chemical reaction dynamics is clearly represented.

In the present study, we have applied the mixed quantum-classical molecular dynamics (QCMD) calculation [27] to the intramolecular proton transfer reaction of malonaldehyde (see Fig. 1-1) in the electronic ground state in solutions. Solvent effects on the reaction dynamics is discussed in detail by comparing the calculations of the proton transfer in different solvents. Quantum effects is also investigated comparing the QCMD calculation with the molecular dynamics calculation in which the all degrees of freedom is treated by classical mechanics, i.g. fully classical molecular dynamics (FCMD) calculations.

Malonaldehyde is well known by its intramolecular proton transfer reaction. The reaction of this molecule has been studied so far [28-41]. For example, its tunneling splitting [28,29] in vacuum has been investigated based on various approaches such as molecular orbital calculations of reaction potential surface [30-32], semi-classical calculations on the tunneling path [33-35], and full-dimensional calculations [36,37]. The reaction in vacuum [38,39] and in water [40,41] have been reported by the molecular dynamics calculations in which the proton is treated by classical mechanics. However, little has been investigated quantum mechanically for the reaction in solution. Now, it is interesting to investigate the quantum dynamics.

In the case of malonaldehyde, the proton transfer reaction occurs only where it has an intramolecular hydrogen bond. Thus, stability of the hydrogen bond in solution must be investigated prior to the investigation of the proton transfer reaction. Malonaldehyde forms enol and keto tautomers and also forms *cis*-enol and *trans*-enol isomers. The hydrogen bonding structure is of the *cis*-enol form shown as rotamer I in Fig. 1-2. The *cis*-enol form has three rotamers, II, III, and IV as shown in Fig. 1-2, which are formed by rotating two dihedral angles, ϕ_1 and ϕ_2 .

In vacuum, *cis*-enol form is much more stable than *trans*-enol one [28]. In solutions, *cis*- and *trans*-enol forms are in thermal equilibrium depending on the solvent [42]. However, it may be assumed that the isomerization from the *cis*-enol to the *trans*-enol form does not occur due to the high torsional potential barrier around the carbon-carbon double bond. Further, barrier heights

between the enol and the keto form have been evaluated to be as high as 47.3 kJ/mol by *ab initio* calculation [43], implying that the molecule with the enol form keeps its configuration for a long time.

Thus, the last thing to do is to test the relative stability of rotamer I with respect to the other rotamers, II, III, and IV, and barrier height among them. Free energy of the rotamers in water has been reported based on the PCM model [44]. However, the estimation may include large error because it was calculated based on the continuum model without explicit solvent molecule. Further, investigation has not yet been done for the free energy barriers among the rotamers.

In the present study, the free energy has been evaluated by the umbrella sampling method combined with molecular dynamics calculation for the flexible malonaldehyde molecule in water, where the solvent water molecules were described explicitly by an all-atom model such as TIP4P. However torsional potential energy function of the malonaldehyde was not available in the literature other than the conventional force fields such as CHARMM, Amber, and OPLS-aa, which have been determined so as to describe the torsional energy of the other molecule, in particular, amino acids. Therefore, the torsional potential energy function suitable to the free energy calculation has been developed.

The purpose of the present study is to investigate quantum and solvent effect on intramolecular proton transfer reaction in solution at a molecular level. Further, in addition to the proton transfer reaction mechanism in solution, relative thermodynamic and kinetic stability of the intramolecular hydrogen bond.

This paper consists of seven chapters including this introduction.

In chapter II, methods for investigating stability of the rotamers, and those for intramolecular proton transfer reaction are described.

In chapter III, a new OPLS-aa based force field for malonaldehyde molecule is presented.

This force field is used for the torsional free energy calculation in water in chapter IV.

In chapter IV, two-dimensional free energy surface was calculated as a function of two dihedral angles. Then, two models of malonaldehyde, flexible and rigid models, were investigated, where the former allows intramolecular vibrations and the latter constrains the intramolecular degrees of freedom except for ϕ_1 and ϕ_2 . The free energy surfaces have been evaluated by umbrella sampling method, and the free energy surface for the rigid model used as a biasing potential for the umbrella sampling calculation has been calculated preliminarily by the thermodynamic integration method. The stability of the hydrogen bonding structure of malonaldehyde is discussed. Furthermore, contribution of the intramolecular vibrations of malonaldehyde to the free energy surface is also presented.

In chapter V, molecular dynamics calculations based upon mixed quantum-classical approximation for the proton transfer reaction of malonaldehyde in water, that is protic polar solvent, have been carried out. Three reaction mechanisms, i.e. tunneling, thermal activation, and barrier vanishing reactions, have been analyzed in detail. Statistical analyses of the reaction rate and its mechanisms have also been investigated. The results are compared with the reaction obtained from quantum wave packet simulations in vacuum and FCMD calculations in solution in order to examine quantum effect as well as solvent effect on the reaction.

In chapter VI, we have performed QCMD and FCMD calculations, which are in the same way as in chapter V, for the intramolecular proton transfer reaction of malonaldehyde in non-polar solvent, neon. Further, the results are compared with water in chapter V. Thus, the solvent effect as well as the quantum effect on the proton transfer reaction has been investigated in detail. In particular, tunneling and thermal activation mechanisms and the resultant reaction rate have been analyzed statistically based on the satisfactorily long trajectories where thousands of reactions were observed. Solvent dependence observed in the present studies was consistent with that by the

experiment [45,46] and the reaction rate theories [5,6].

We conclude in chapter VII.

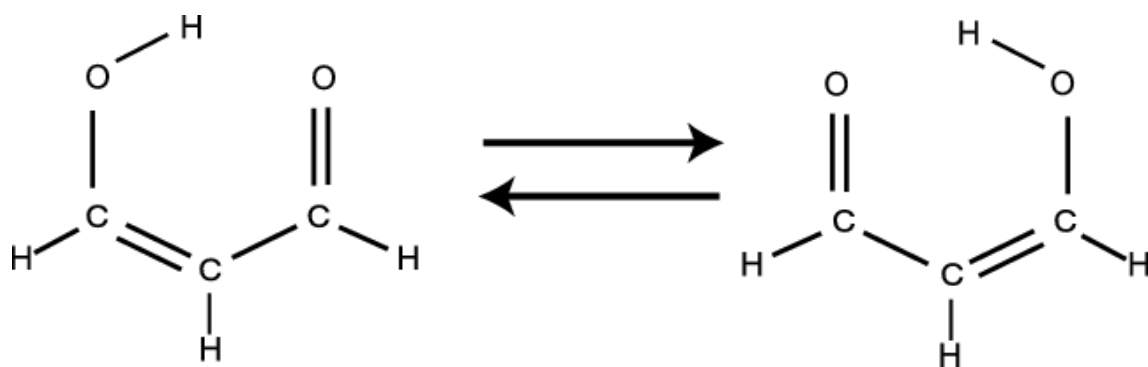


FIG. 1-1. Intramolecular proton transfer reaction of malonaldehyde.

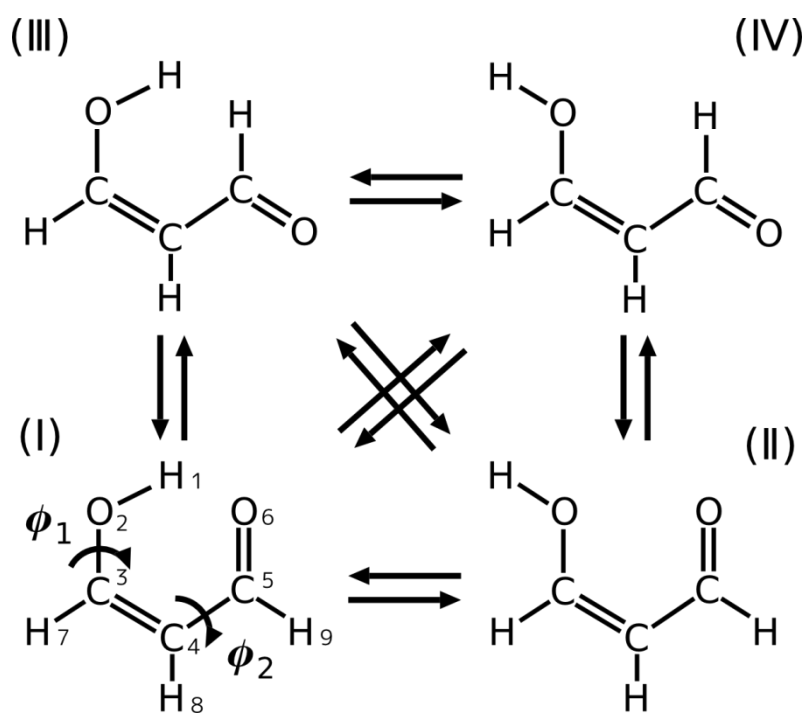


FIG. 1-2. Four rotamers, I, II, III, and IV of *cis*-enol malonaldehyde and the definition of the dihedral angles, ϕ_1 and ϕ_2 . The rotamer I is in the same structure as in Fig. 1-1.

II. METHOD

In this chapter, methods of molecular dynamics calculations of free energy surface for rotamers to investigate their stability and molecular dynamics calculations for proton transfer reaction are described. In section A, methods of parameter fitting to extended OPLS-aa force field for free energy calculations, which is employed in chapter III, and free energy calculation methods, which are employed in chapter IV, are described. In section B, methods of mixed quantum-classical molecular dynamics and fully classical molecular dynamics for proton transfer reaction dynamics in solution, which are employed in chapter V and VI, are described. In this section, definitions of state, reaction and reaction mechanism are also described.

A. Molecular dynamics calculations of free energy surface for rotamers

1. Extension of torsional force field based on OPLS-aa

Torsional potential function of the ordinary OPLS-aa [52-55] is given by

$$V_{dihedral}(\{\phi_i\}) = \sum_{i=1}^2 \left[\frac{V_1^{(i)}}{2} (1 + \cos(\phi_i)) + \frac{V_2^{(i)}}{2} (1 - \cos(2\phi_i)) + \frac{V_3^{(i)}}{2} (1 + \cos(3\phi_i)) \right] \quad (2-1)$$

However, in order to reproduce the potential energy surface from the present *ab initio* calculations, extended terms for ϕ_1 and ϕ_2

$$V_{dihedral}^{ext}(\phi_1, \phi_2) = \frac{V_4^{(1)}}{2} [1 - \cos(4\phi_1)] + \frac{V_4^{(2)}}{2} [1 - \cos(4\phi_2)] + \sum_{n,m=1}^4 V_{n,m} \cos(n\phi_1) \cos(m\phi_2) \quad (2-2)$$

were added to the ordinary OPLS-aa model. The first and second terms are for the extension of Fourier expansion up to the wave number of four. The third term is the cross term of two cosine functions of ϕ_1 and ϕ_2 .

In the fitting, ordinary OPLS-aa parameters [52-55] were used for the force constant of stretching and bending, torsion of the double bond, improper torsion, and Lennard-Jones potential.

The point charges for the carbon and oxygen atoms in the conjugated system were modified by averaging the calculated ESP charges keeping the total charge to be zero since the difference from the original OPLS-aa is great. The equilibrium bond length and the equilibrium bond angle are given by the average of the optimized parameters obtained so as to minimize the sum of square of the forces on the atoms of four plane rotamers. The torsion potential parameters for ϕ_1 and ϕ_2 were determined by least square method for the potential energy surface obtained by the *ab initio* calculations.

2. Free energy calculations

Free energy surface as a function of two-dihedral angles, ϕ_1 and ϕ_2 shown in Fig. 1-2, has been calculated, as follows.

2-1. Thermodynamic integration method

In the frame work of thermodynamic integration method [47], two-dimensional free energy surface of two integration valuables, ϕ_1' and ϕ_2' , is given for rigid malonaldehyde in the form of a line integral by

$$\Delta G_{TI}^{(rigid)}(\phi_1, \phi_2) = \int_0^{\phi_1} \left\langle \frac{\partial V(\phi_1', \phi_2')}{\partial \phi_1'} \right\rangle_{\phi_1'=\phi_1', \phi_2'=\phi_2} d\phi_1' + \int_0^{\phi_2} \left\langle \frac{\partial V(\phi_1', \phi_2')}{\partial \phi_2'} \right\rangle_{\phi_1'=0, \phi_2'=\phi_2'} d\phi_2' \quad (2-3)$$

where $\Delta G_{TI}^{(rigid)}(\phi_1, \phi_2)$ is the free energy difference between the conformations at (ϕ_1, ϕ_2) and $(0^\circ, 0^\circ)$. The integration path is, here, chosen to be $(0^\circ, 0^\circ) \rightarrow (0^\circ, \phi_2) \rightarrow (\phi_1, \phi_2)$. $V(\phi_1, \phi_2)$ is the potential energy of the total system including solute malonaldehyde and solvent water molecules.

$\langle \dots \rangle_{\phi_1'=\phi_1', \phi_2'=\phi_2}$, for example, denotes the ensemble average where the torsion angle ϕ_1' and ϕ_2' are

fixed at ϕ_1' and ϕ_2 , respectively. Mean forces, i. e. mean torques $-\langle \partial V / \partial \phi_1 \rangle_{\phi_1'=\dots, \phi_2'=\dots}$ and $-\langle \partial V / \partial \phi_2 \rangle_{\phi_1'=\dots, \phi_2'=\dots}$, are calculated by averaging $\partial V / \partial \phi_1$ and $\partial V / \partial \phi_2$ over the trajectories obtained from the MD calculations where the two dihedral angles are fixed.

2-2. Umbrella sampling method

In the umbrella sampling MD calculations [47], weighting function

$$\omega(\phi_1, \phi_2) = \exp \left[-\frac{\Delta U_{bias}(\phi_1, \phi_2)}{kT} \right] \quad (2-4)$$

was employed where ΔU_{bias} is the biasing potential. Then, the free energy by umbrella sampling method, $\Delta G_{US}(\phi_1, \phi_2)$, is calculated from the distribution $P(\phi_1, \phi_2)$ of ϕ_1 and ϕ_2 in this biased simulation and is given by

$$\Delta G_{US}(\phi_1, \phi_2) = -\Delta U_{bias}(\phi_1, \phi_2) - kT \ln \left[\frac{P(\phi_1, \phi_2)}{P(0, 0)} \right]. \quad (2-5)$$

B. Molecular dynamics calculations of proton transfer reaction in solution

First, we define reaction coordinate. Then, Hamiltonian and equation of motion for QCMD and FCMD as well as potential energy curve and its division into the reactant and product potential wells are presented. Calculation conditions are also presented. Definition of the reaction and classification of the reaction into three reaction mechanisms are also presented.

1. Equation of motion

1-1. Reaction coordinate

In the mixed quantum-classical approximation, chemical reaction is simplified to be

transitions from the reactant state to the product state defined on the potential energy surface as a function of reaction coordinate. The reaction coordinate must be chosen from the total nuclear degrees of freedom.

In general, a chemical reaction path of solute is given by intrinsic reaction coordinate (IRC), that is, the minimum energy path from the stable point in the reactant well to that in the product well through the saddle point at the barrier top on the adiabatic potential energy surface. Proton transfer of malonaldehyde is the reaction of heavy-light-heavy type, which has a long distance between the two stable points along the IRC because the reaction path is largely curved in the $3N$ -dimensional Cartesian coordinate space. Here, N denotes the number of atoms of the solute molecule. On the other hand, semi-classical theories for malonaldehyde at 0 K in vacuum give the tunneling paths a little different from the IRC. The tunneling paths connect the two stable points through a higher energy region of the barrier and don't go through the saddle point [33,34]. Thus, in principle, both the IRC and tunneling path must be taken into account when we choose the reaction coordinate. However, potential energy surface in solution changes by the solute-solvent interactions. In fact, as shown later, most frequently observed shape of the potential curve in the protic polar solvent is asymmetric double well. This is caused by the stabilization of the reactant well by solvation. When the potential curve is asymmetric, tunneling reaction scarcely occurs because vibrational energy level is different between the reactant and product wells. The reaction occurs only when the vibrational energy level is close to each other and the barrier height is low as discussed later. The condition is satisfied only occasionally in the trajectory by thermal fluctuation of the solvent. This is the main rate-determining process for the tunneling reaction. On the other hand, considering thermal activation reaction, a model based on the IRC is reasonable. In non-polar solvent, shown later, stabilization of the occupied well is very small and the double well potential is nearly symmetric. In the non-polar solvent, the tunneling path may be important. However, the

qualitative discussion is possible choosing IRC because, shown later, the tunneling reaction in the non-polar solvent is independent of the choice of the IRC. Although it is interesting to construct a realistic model including the above two factors, such model is too complex. Here we adopt the IRC in vacuum as the reaction path. The choice will be discussed again later in this section.

1-2. Hamiltonian

Hamiltonian of the form

$$H(\mathbf{r}, \mathbf{R}, \mathbf{p}, \mathbf{P}) = H_0(\mathbf{r}, \mathbf{p}) + H_S(\mathbf{R}, \mathbf{P}) + V_I(\mathbf{r}, \mathbf{R}), \quad (2-6)$$

is used commonly in QCMD and FCMD, where \mathbf{r} is the Cartesian coordinate of the solute molecule, \mathbf{R} the Cartesian coordinate of the solvent molecules, and \mathbf{p} and \mathbf{P} the conjugated momenta of \mathbf{r} and \mathbf{R} , respectively. H_0 is the Hamiltonian of the solute molecule, H_S the Hamiltonian of the solvent molecules, and V_I the interaction Hamiltonian between the solute and solvent.

Here, we approximate H_0 by the reaction path Hamiltonian [48,49]. Then, coordinate of the solute is the IRC in vacuum presented by mass-weighted coordinate, q , and the other $3N - 7$ normal modes perpendicular to the IRC. As shown later, the vibrational frequencies in the solute potential well around the stable point along q are low. Then, fast vibrational motions perpendicular to q can be integrated out assuming that they are found in their ground states. This gives the zero-point energies (ZPEs), that is, the adiabatic approximation is introduced for the vibrational motions normal to the IRC. Then, the Hamiltonian of the solute is given by

$$H_0(q, p_q) = \frac{1}{2} p_q^2 + V_0^q(q) + \sum_k^{3N-7} \frac{1}{2} \hbar \omega_k(q), \quad (2-7)$$

where p_q represents conjugated momentum of q . The first term of the right hand side of Eq. (2-7) is the kinetic energy of q , the second term, V_0^q , represents the solute potential energy along q in vacuum, and the third term is the summation of ZPEs for the normal modes perpendicular to q ,

where $\omega_k(q)$ represents q -dependent angular frequency for the k -th normal mode. The effect of the centrifugal force in the kinetic energy term in Eq. (2-7) due to the large curvature of q axis in Cartesian coordinate space is ignored. As a result, Eq. (2-7) is reduced to the model depending on two variables, q and p_q , then, the second and third terms of the right hand side of Eq. (2-7) may be regarded as the effective one-dimensional potential energy in vacuum,

$$V_0^{eff}(q) = V_0^q(q) + \sum_k^{3N-7} \frac{1}{2} \hbar \omega_k(q). \quad (2-8)$$

Thus, degrees of freedom of the solute coordinate, \mathbf{r} , are reduced to the one-dimensional q axis in the $3N$ -dimensional Cartesian coordinate space and degrees of freedom of the other normal modes perpendicular to q vanished.

The Hamiltonian for the solvent molecules, $H_S(\mathbf{R}, \mathbf{P})$, may be described by the ordinary classical force field and kinetic energy. The interaction Hamiltonian, V_I , is given by the sum of Lenard-Jones (LJ) potential energy, V_I^{LJ} , and Coulombic potential energy, V_I^{CL} , between the solute and solvent,

$$V_I(\mathbf{r}(q), \mathbf{R}) = V_I^{LJ}(\mathbf{r}(q), \mathbf{R}) + V_I^{CL}(\mathbf{r}(q), \mathbf{R}). \quad (2-9)$$

1-3. Equation of motion

1-3-1. Mixed quantum-classical approximation

In the mixed quantum-classical approximation, degree of freedom, q , is treated quantum mechanically, while \mathbf{R} classical mechanically. Thus, q and p_q in Eq. (2-7) are operators, q and $-i\hbar \frac{\partial}{\partial q}$, respectively, whereas \mathbf{R} is dealt with a time dependent parameter, $\mathbf{R}(t)$, for the quantum system. This evolves following the classical equation of motion. Details of the calculation method are presented in Appendix and our previous paper [27].

Adiabatic potential energy curve of the solute in solution

$$V_0(q; \mathbf{R}(t)) = V_q^{eff}(q) + V_l(\mathbf{r}(q); \mathbf{R}(t)) \quad (2-10)$$

was divided into reactant potential, $V^R(q; \mathbf{R}(t))$, and product potential, $V^P(q; \mathbf{R}(t))$, every time step as shown in Fig. 2-1. Then, the vibrational eigen states in the reactant and product potential wells, $\{|\xi_n^{(R)}\rangle\}$ and $\{|\xi_n^{(P)}\rangle\}$, respectively, are obtained from the stationary state Schrödinger equation. The wave function may be expanded by the vibrational eigen functions in the reactant and product wells,

$$|\Psi(t, q; \mathbf{R}(t))\rangle = \sum_n C_n^{(R)}(t) |\xi_n^{(R)}(q; \mathbf{R}(t))\rangle + \sum_n C_n^{(P)}(t) |\xi_n^{(P)}(q; \mathbf{R}(t))\rangle, \quad (2-11)$$

where $C_n^{(R)}$ and $C_n^{(P)}$ are the expansion coefficients for the n -th vibrational state within the reactant well and the product one, respectively. Substituting Eq. (2-11) into the time-dependent Schrödinger equation, the equation of motion for the quantum system is presented by differential equation for $C_n^{(R)}$ and $C_n^{(P)}$ with respect to time t .

The Newtonian equation of motion

$$m_j \frac{d^2 \mathbf{R}_j}{dt^2} = \mathbf{F}_j \quad (2-12)$$

is solved to obtain the trajectory of the classical system, where m_j and \mathbf{R}_j represent the mass and position vector of the j -th classical atom, respectively, and \mathbf{F}_j denotes the force on the j -th atom.

According to the surface-hopping approximation, force on the classical atom j is given by Hellmann-Feynman force from a specified vibrational state of the quantum system, that is, when the quantum system is in the state k in the reactant well,

$$\mathbf{F}_j = - \left\langle \xi_k^{(R)} \left| \frac{\partial V_l}{\partial \mathbf{R}_i} \right| \xi_k^{(R)} \right\rangle - \frac{\partial V_S}{\partial \mathbf{R}_i}, \quad (2-13)$$

where the first term of the right hand side is the force from the quantum system, and the second term is the force from the classical solvent. The transition from the current state to the other is decided by the transition probability obtained from Eq. (A-5) in Appendix and a random number according to the fewest-switches algorithm.

1-3-2. Fully classical approximation

Time evolution of the classical system is obtained by solving the Newton's equation of motion for q and \mathbf{R} . The equation of motion for q is given by

$$\begin{aligned}\ddot{q} &= -\frac{\partial V_0(q, \mathbf{R})}{\partial q} \\ &= -\frac{\partial V_0^{eff}(q)}{\partial q} - \frac{\partial V_I(\mathbf{r}(q), \mathbf{R})}{\partial q}.\end{aligned}\quad (2-14)$$

The second term of the right hand side of Eq. (2-14) is the force on the solute by the interaction with the solvent molecules. The term is written by

$$-\frac{\partial V_I}{\partial q} = -\sum_i^{3N} \frac{\partial V_I}{\partial r_i} \frac{\partial r_i(q)}{\partial q}.\quad (2-15)$$

Derivative of V_I with respect to the i -th Cartesian degree of freedom of the solute atom, r_i , of the right hand side of Eq. (2-15) is the force obtained from an ordinary classical MD calculation, and $\partial r_i(q)/\partial q$ is the element of the coordinate transformation matrix. Thus, Eq. (2-15) is the inner product of the force vector on the solute atoms represented by the Cartesian coordinate system and the eigen vector of q , that is, the projection of the force on the q axis. Coordinate $\mathbf{r}(q)$ is given by the third order Lagrange interpolation for the Cartesian coordinates data of the molecular structure at grid points on the IRC.

Equation of motion for the solvent molecules, $\{\mathbf{R}_j\}$, is the Newtonian equation of motion, and the force is presented by

$$\mathbf{F}_j = -\frac{\partial V_I}{\partial \mathbf{R}_i} - \frac{\partial V_S}{\partial \mathbf{R}_i}.\quad (2-16)$$

2. Potential model of solute

In order to obtain effective one-dimensional potential of the solute molecule $V_0^{eff}(q)$ in Eq. (2-8), we used *ab initio* calculation data of $V_0^q(q)$ and Hessian matrices along the IRC at the

MP2/6-31g** level by Yagi *et. al.* [32]. Normal modes perpendicular to q were integrated out assuming that the motion of the normal modes is fast, that is, ZPEs were added to $V_0^q(q)$. This is reasonable because the wave number of the normal modes perpendicular to q , ranges from 280 cm^{-1} to 3560 cm^{-1} , which is greater than that of q , 280 cm^{-1} , around the stable point.

Figure 2-2 shows $V_0^q(q)$ by Yagi *et al.* [32] and the calculated $V_0^{eff}(q)$. Potential barrier height of $V_0^{eff}(q)$ was 6.3 kJ/mol after adding ZPEs, which is significantly lower than that of the original $V_0^q(q)$, 15.1 kJ/mol . The minimum value of $V_0^q(q)$ without ZPEs correction is presented at $q = \pm 0.87\text{ \AA}(\text{g/mol})^{1/2}$, whereas it is shifted to $q = \pm 0.80\text{ \AA}(\text{g/mol})^{1/2}$ after the ZPEs correction.

The Coulomb and LJ interaction parameters of the solute molecule depend much on q . In order to evaluate partial charges on the reacting solute atoms, quantum chemical calculations have been done at the MP2/6-31G** level [51], where ESP point charges were obtained for the solute atoms as a function of q . With respect to the LJ interaction parameters, OPLS-aa force field parameters [52-55] were used. Linear q dependence of the parameters was assumed between the stable points in the reactant and product wells.

For details including the division of potential energy curve V_0 into reactant and product wells, V^R and V^P , respectively, see Appendix.

3. Numerical representation of wave function in QCMD

801 grid points on q axis ranging from -8.0 to $8.0\text{ Bohr amu}^{1/2}$ (-4.23 to $4.23\text{ \AA}(\text{g/mol})^{1/2}$) with the interval of $0.02\text{ Bohr amu}^{1/2}$ ($0.011\text{ \AA}(\text{g/mol})^{1/2}$) were used to describe the wave function in QCMD. Vibrational eigen states in each potential well were described by the linear combination of 30 Laguerre polynomial functions. The wave function in Eq. (2-11) was expanded by the vibrational eigen functions whose energy level is below the one higher than the barrier top by 1.5 kcal/mol (6.3 kJ/mol). Then, the function includes two or three vibrational states above the barrier

for each well. This must be sufficient to describe the reacting vibrational states at room temperature.

4. Analysis

First, we define the type of potential energy curve V_0 . Three types of potential energy curves were typically found in the trajectories. For example, for QCMD, Fig. 2-3 show (a) double-well, which has two deep potential wells such that ZPEs in both wells are below the barrier, (b) strongly-asymmetric-single-well, which has a deep well on one side such that the ZPE is found below the barrier (or an effective barrier whose position is indicated by the vertical dotted line) while a shallow well (or no well) on the opposite side does not give the ZPE below the barrier (or the effective barrier), and (c) quasi-symmetric-single-well, which has no more than shallow well or no wells divided by the barrier (or an effective barrier whose position is indicated by the vertical dotted line). The definition for FCMD is similar as shown in Figs. 2-4(a), (b), and (c).

In the present calculation, proton transfer reaction may be regarded as a transition from a reactant state to a product state. Thus, we must define the reactant and product states. After the definition of the states is given, definition of the reaction and its classification with respect to the reaction mechanisms are presented.

Several definitions may be possible for a reactant state and a product state in the fluctuating potential energy curve by the interactions with the solvent. For example, a simple definition where the reactant and product states are divided at the barrier top [22,23] is one choice. However, this is not appropriate for the system where single-well potential appears. Further, this definition cannot be applied to the quantum system.

Thus, we defined the reactant and product states for QCMD to be the vibrational state whose energy level is lower than the barrier top and the vibrational state whose energy level is higher than the barrier top was defined to be the transient one. According to this definition,

vibrational states drawn by blue and red lines are the reactant and product state, respectively, when, for example, the system was initially in the left well as shown in Fig. 2-3(a) for regular double-well. The states drawn by gray lines are the transient ones. In the same way, the states drawn in blue are the reactant state and in gray the transient states as shown in Fig. 2-3(b) for strongly-asymmetric-single-well and in Fig. 2-3(c) for quasi-symmetric-single well.

In Fig. 2-4(a), (b) and (c), three typical shapes of V_0 (solid line) found in FCMD, and V^R and V^P (broken lines) are presented. Their shapes are the same as those in QCMD in Fig. 2-3(a), (b) and (c), respectively. The vertical dotted line at $q = q^\ddagger$, the crossing point of V^R and V^P , in Fig. 2-4 divides potential well into the reactant well and the product one and gives the location of the (effective) barrier.

A potential curve with a barrier higher than $kT/2$ is illustrated in Fig. 2-4(a). This may be considered to be regular double-well potential because, in order to get over this barrier higher than the thermal energy, extra activation energy is required. The reactant and product states are defined by the value of $q(t)$. The border is q^\ddagger at the barrier top. Thus, the blue line represents, for example, reactant state and the red line the product state. For the strongly-asymmetric-single-well in Fig. 2-4(b), no barrier higher than $kT/2$ is found. In this case, the left well colored in blue represents, for example, reactant state but the right well colored in gray the transient state. For the quasi-symmetric-single-well in Fig. 2-4(c), no barrier or well is found. In this case, the state is regarded as transient for all q .

For these three states, i.e. reactant state, product state, and transient state, we can define proton transfer reaction, by a transition between the reactant and product states. However, when the system makes a transition from a reactant state to a transient one and returns back to the reactant state, this is not regarded as reaction. When the system goes back and forth between the reactant and product states in a short time, it is regarded as recrossing.

Reactions may be classified into three mechanisms for QCMD, that is, tunneling reaction, thermal activation reaction, and barrier vanishing reaction. For FCMD, they are classified into two mechanisms, that is, thermal activation reaction and barrier vanishing reaction. The classifications are made on the basis of the type of V_0 and vibrational states at the moment when the reaction occurs. When a number of transitions occur in the transient states, the reaction mechanism is decided based on the shape of V_0 in the last transition to the product state.

Tunneling reaction can be defined to be the direct transition from the reactant state to the product one below the barrier of double-well potential surface in Fig. 2-3(a). Thermal activation reaction in QCMD is defined by transition from the reactant state to the product one via transient states over the barrier higher than ZPE in the regular double-well potential, for example, excitation of the vibrational state in the reactant well to the states above the barrier, that is the transient state, followed by transition to the transient states in the product well and succeeding energy relaxation there. In FCMD, the thermal activation reaction is given by the crossing of the system over the barrier higher than $kT/2$ through the border q^\ddagger between two wells of the regular double-well potential shown in Fig. 2-4(a). Upward translation of the system in the strongly-asymmetric-single-well in Fig. 2-4(b) followed by the stabilization of the transient state in the product well by solvation is also assigned to the thermal activation reaction.

The barrier vanishing reaction is defined by a reaction where the transition between the reactant and product states in the quasi-symmetric-single-well potential in Figs. 2-3(c) and 2-4(c) is followed by the stabilization of the transient state in the product well by solvation. Downward transition in the strongly-asymmetric-single-well potential in Figs. 2-3(b) and 2-4(b) is also assigned to the barrier vanishing reaction.

Definition of the state, type of the potential energy curve, and the reaction mechanism explained in this section are summarized in Table A-1 in Appendix.

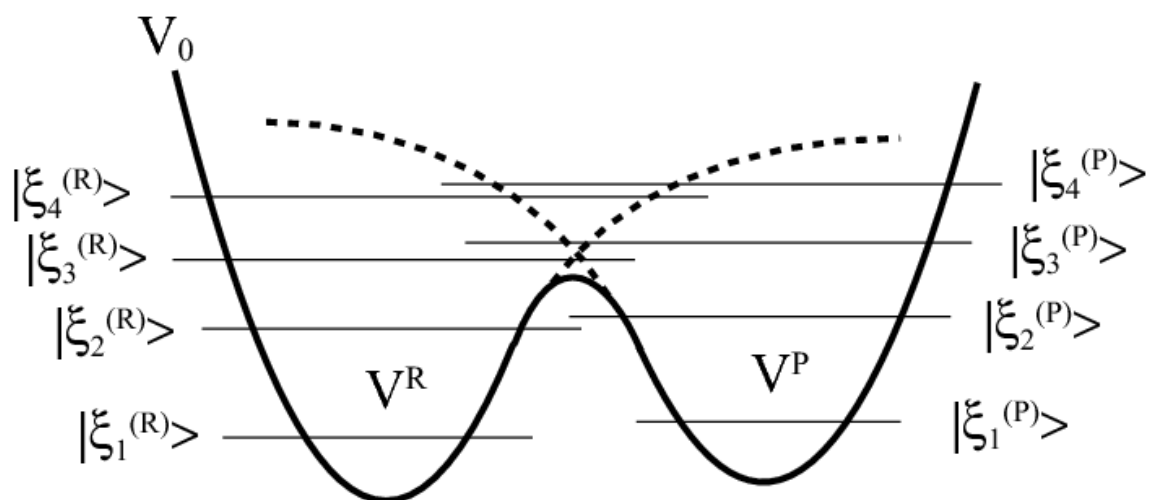


FIG. 2-1. A schematic picture for adiabatic potential energy curve V_0 (thick solid line), reactant and product potential energy wells V^R and V^P with added dotted lines, respectively. Vibrational states in the reactant well, $\{|\xi_n^{(R)}\rangle\}$, and those in the product well, $\{|\xi_n^{(P)}\rangle\}$, are also shown (thin solid lines).

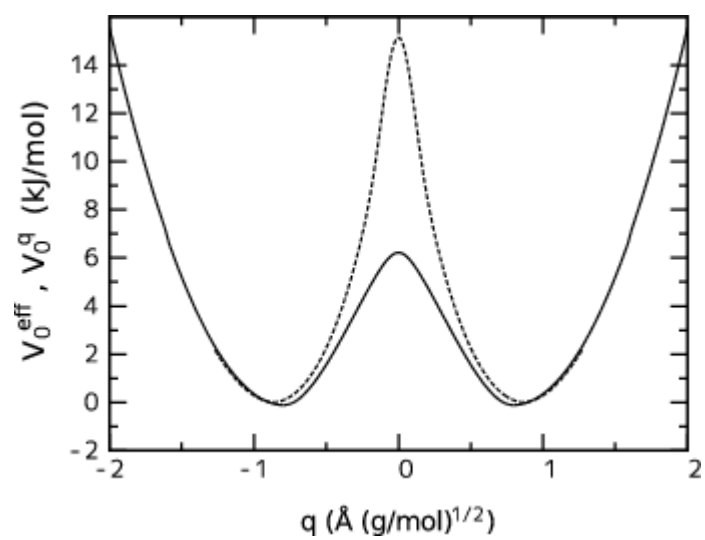


FIG. 2-2. Potential energy curve, V_0^q , (dotted line) along the IRC represented by q and effective one-dimensional potential energy curve, V_0^{eff} , (solid line) for malonaldehyde in vacuum.

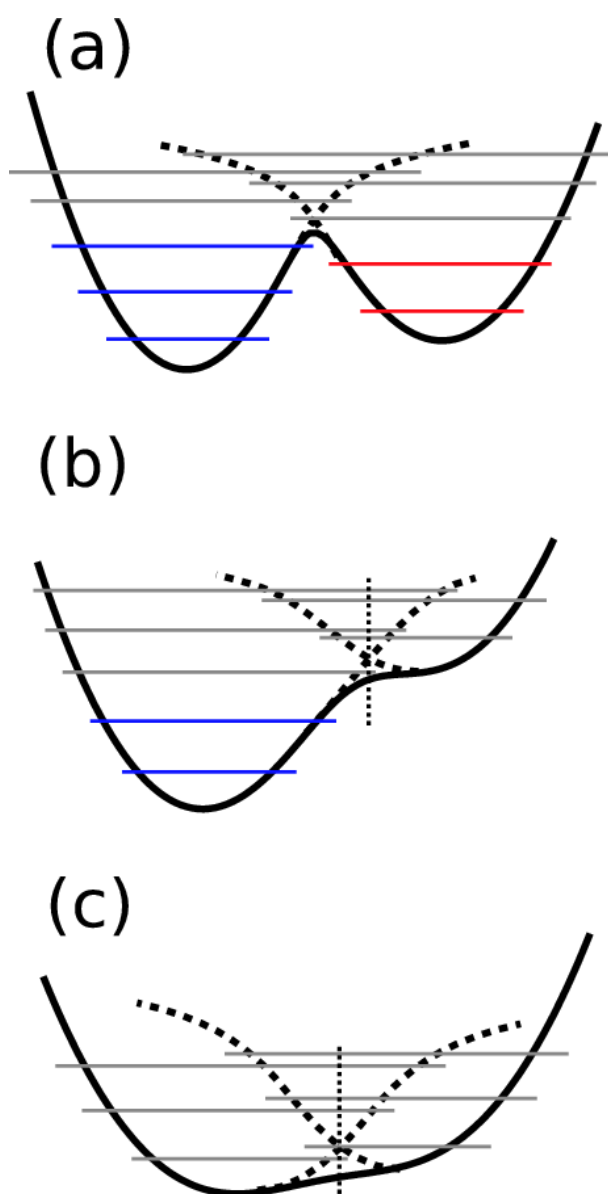


FIG. 2-3. Three types of adiabatic potential energy curves V_0 (thick solid lines) typically found in the trajectories of QCMD. Reactant and product wells V^R and V^P , respectively, with added broken lines are determined according to the guidelines described in the text. Among the vibrational energy levels (horizontal lines), where blue and red lines represent reactant and product vibrational states, respectively, when, for example, the system was initially in the left well, and gray lines transient states. The figures show: (a) double-well, which has two deep potential wells such that ZPEs in both wells are below the barrier, (b) strongly-asymmetric-single-well, which has a deep well on one side

such that the ZPE is found below the barrier (or an effective barrier whose position is indicated by the vertical dotted line) while a shallow well (or no well) on the opposite side does not give the ZPE below the barrier (or the effective barrier), and (c) quasi-symmetric-single-well, which has no more than shallow well or no wells divided by the barrier (or an effective barrier whose position is indicated by the vertical dotted line).

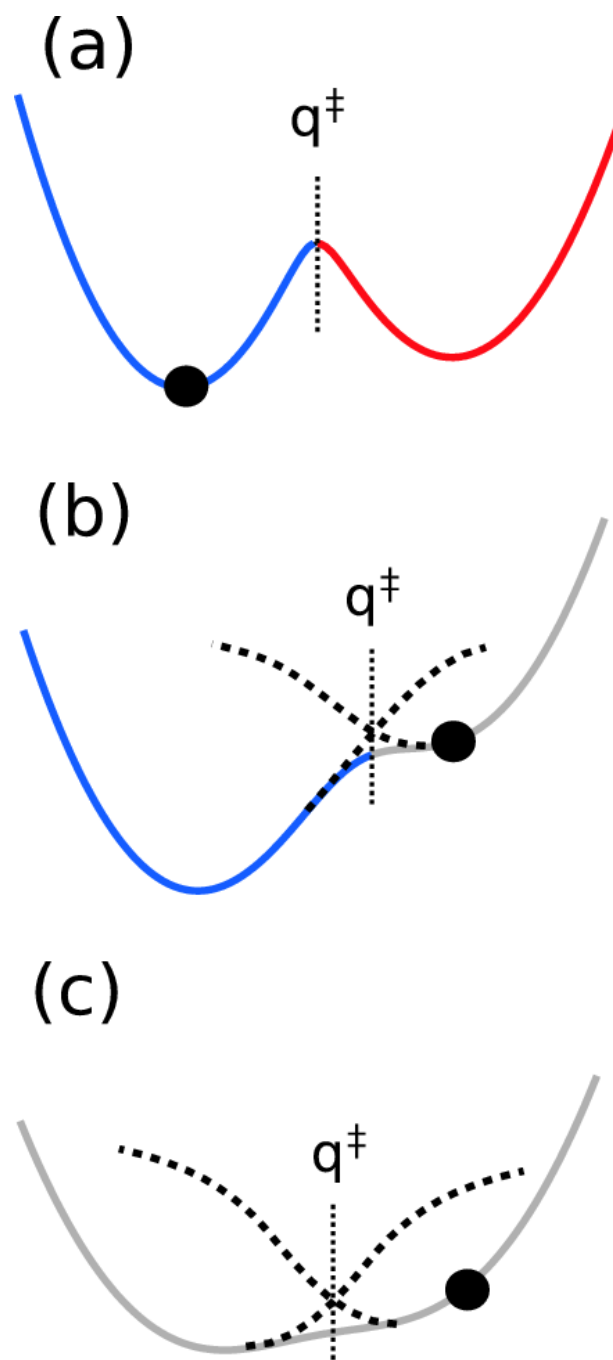


FIG. 2-4. Three types of adiabatic potential energy curves V_0 typically found in the trajectories of FCMD. Black broken lines in (b) and (c) are added to the reactant well V^R and the product one V^P according to the guideline in the text. Vertical dotted line at q^\ddagger divides the reactant and product wells. Reactant, product, and transient states are colored in red, blue, and gray, respectively. These figures indicate: (a) double-well, which has two deep potential wells divided by a high barrier (\geq

$kT/2$ for both wells), (b) strongly-asymmetric-single-well, which has a deep well on one side divided by a barrier (or an effective barrier) higher than $kT/2$ measured from the minimum on this side while a shallow well (or no well) on the opposite side with the barrier (or the effective barrier) lower than $kT/2$, and (c) quasi-symmetric-single-well, which has no more than shallow wells or no wells divided by the barrier (or an effective barrier) higher than $kT/2$ for each side.

III. AN IMPROVED TORSIONAL FORCE FIELD FOR CIS-ENOL MALONALDEHYDE

A. Introduction

Previously, the rotamers of the cis-enol form of malonaldehyde have been studied in detail by *ab initio* molecular orbital (MO) calculations [56-58]. Delchev *et al.* calculated the conformational potential energy curve along the several reaction paths among the planar rotamers in vacuum at Hartree-Fock (HF) level [56]. Then, energy of the rotamers as well as the barrier height of the paths has also been calculated by *ab initio* methods at HF, MP2, BLYP, and B3LYP levels [57,58]. However, our purpose is to obtain the torsional potential energy function for the use of molecular dynamics calculation that covers the whole 2D potential surface including all paths among all rotamers and the function is not available yet.

In this chapter, in order to obtain refined force field of *cis*-enol malonaldehyde with respect to torsional potential energy, we calculated two-dimensional potential energy surface in vacuum based on the *ab initio* calculation at MP2/6-31G** level as a function of the two dihedral angles, ϕ_1 and ϕ_2 (see Figure 1-2) and then fitted it to a potential function where cross terms of the two dihedrals are added to the ordinary single cosine terms of the OPLS-aa type.

B. *Ab initio* molecular orbital calculations

Totally, 1296 conformations were prepared for two dihedral angles, ϕ_1 and ϕ_2 , every 10° ranging from 0° to 350°. *Ab initio* calculations have been done at the level of MP2/6-31G** using Gaussian 03 program package [59]. Energy minimization was performed for each conformation fixing ϕ_1 and ϕ_2 . The value of atomic point charge was evaluated, too, by ESP method [60].

Procedure of parameter fitting is described in subsection II A 1 in detail.

C. Results and discussion

The potential energy surface obtained by the present *ab initio* calculations, $\Delta E_{MO}(\phi_1, \phi_2)$, is shown in Figure 3-1 (a). This surface has symmetry with respect to the point, $(180^\circ, 180^\circ)$, coming from the molecular structure of the malonaldehyde molecule. The energy minima found on the potential surface correspond to the four planar rotamers, see Figure 1-2, where rotamer I at $(0^\circ, 0^\circ)$ is most stable. We adopt the energy of this rotamer to be zero as a reference.

The force field parameters evaluated in this study are shown in Table 3-1. Table 3-1 (a) presents the point charges on the atoms of *cis*-enol malonaldehyde. The original values of the OPLS-aa force field [52-55] were adopted for the point charge on the hydrogen atoms, since the difference is negligible between the original value and the present one. The equilibrium bond length shown in Table 3-1 (b) has only small difference from the original OPLS-aa parameters. The difference is as small as 10^{-2} Å. The equilibrium bond angle at 0-1-2 and 2-3-4 shown in Table 3-1 (c) is smaller than the standard OPLS-aa value by 6.4° and 6.5° , respectively, while other bond angles have only negligible difference from the original values. The parameters of the torsional potential for the extended OPLS-aa force field are shown in Table 3-1 (d). The single cosine function terms, $V_n^{(i)}$, for $n=2$ are the largest, 14.546 and 9.910 kJ/mol, for ϕ_1 and ϕ_2 , respectively, and the values for $n=1$, -8.724 and -3.133 kJ/mol, for ϕ_1 and ϕ_2 , respectively, show the second contribution. The values for $n=3$, -2.076 (for ϕ_1) and -0.435 (for ϕ_2), have less contribution. For $n=4$, the extended terms, the value for ϕ_1 is -0.143 kJ/mol, which is very small compared with the others, while, the value for ϕ_2 , -0.470 kJ/mol, is larger than $V_3^{(2)}$. Parameters of the cross terms, $V_{n,m}$, show the largest value for $n=m=2$, -0.395 kJ/mol. $V_{2,1}$ and $V_{1,2}$ are second and third largest, 0.357 and 0.326 kJ/mol, respectively. Other cross terms show only very small contribution. Thus, wave number of 1 and 2 is particularly important for both of the single cosine function and the cross term.

The potential energy surface calculated by the present extended OPLS-aa force field model,

$\Delta E_{\text{EX-OPLS}}(\phi_1, \phi_2)$, is shown in Figure 3-1 (b). $\Delta E_{\text{EX-OPLS}}$ is in good agreement with ΔE_{MO} in the whole region. The standard deviation of $\Delta E_{\text{EX-OPLS}}$ from ΔE_{MO} is as small as 1.9 kJ/mol. It is smaller than that by the original functional form ΔE_{OPLS} , 3.3 kJ/mol. In the case of the model with the first and second terms in the right hand side in Eq. (2-2) and without the cross terms, the standard deviation is 3.2 kJ/mol, showing the importance of the cross term. The function with the cross term but without the first and second terms in the right hand side in Eq. (2-2), shows the standard deviation of 2.1 kJ/mol, which reproduces ΔE_{MO} better than ΔE_{OPLS} but still has a larger error than $\Delta E_{\text{EX-OPLS}}$.

In order to test the performance of the present force field, the calculated energy difference between the rotamers I and II as well as the potential barrier along the reaction path from the rotamer I to the rotamer II, i.e. the height of the saddle point (104°,333°) from the rotamer I is compared in Table 3-2 with that of several *ab initio* calculations reported so far [56-58] together with the original OPLS-aa. As clearly shown in the table, the present force field reproduces well the accurate *ab initio* calculation at MP2/6-31G** level by Buemi *et al.* [58], the same electron correlation and basis set level as the present calculation. The present force field also shows a good correspondence to the ones by density functional theory calculations. However, the energies by the low quality calculations without electron correlation are a little different from the above ones. In particular, the energies, i.e. the energy of the rotamer II and the barrier height calculated from the original OPLS-aa force field is considerably different from the *ab initio* results with high accuracy. Thus, the performance of the present force field is satisfactory for the use of molecular dynamics calculation.

Further comparison of the extended OPLS-aa model, $\Delta E_{\text{EX-OPLS}}$, with the original OPLS-aa, ΔE_{OPLS} , is presented in Figure 3-3 for various linear paths given in Figure 3-2. ΔE_{MO} is also given in the figure. The original OPLS-aa model does not reproduce well the result of the MO calculation. Its barrier height along A (Figure 3-3 (a)) and B (Figure 3-3 (b)) and the energy of the rotamer IV

(Figure 3-3 (c),(d)) show great difference from the MO calculation. On the other hand, the extended OPLS-aa model reproduces them very well. However, the barrier height along E and E' has some difference from those by the MO calculation. The energy of the four rotamers and the potential barrier height along the paths in Figure 3-2 are shown in Table 3-3 (a) and (b), respectively, for ΔE_{OPLS} and $\Delta E_{\text{EX-OPLS}}$. The values in the parentheses in the table indicate the difference from ΔE_{MO} . All the energies of the rotamers and the barriers for ΔE_{OPLS} are less than those of ΔE_{MO} with the error in the range of -0.4 ~ -12.4 kJ/mol. In particular, the error is large for the rotamer IV, -7.0 kJ/mol, and at the top of the barrier along the paths A and B, the error is -10.9 and -12.4 kJ/mol, respectively. On the other hand, the error of $\Delta E_{\text{EX-OPLS}}$ is very small, i.e. at most 3.4 kJ/mol at the top of the barrier along the path E. The error in the other regions is small, i.e. less than 1.3 kJ/mol.

To summarize, the two-dimensional conformational potential energy surface of the *cis*-enol malonaldehyde has been calculated by *ab initio* method at MP2/6-31G** level. This potential energy surface can not be reproduced accurately by the ordinary torsion potential function, the sum of single cosine functions of the dihedral angles. This can be increasingly improved by adding the cross term of cosine functions of the dihedral angles.

TABLE 3-1. Parameters of the extended OPLS-aa force field. (a) Point charge on the atom, (b) equilibrium bond length (Å), (c) equilibrium bond angle (degree), and (d) torsional parameter (kJ/mol). The integers in the left column in (a), (b), and (c) indicate the atom as defined in Figure 1-2.

(a)		(b)		(c)	
Atom	Point charge	Bond	Equilibrium bond length(Å)	Angle	Equilibrium bond angle(degree)
1	0.4180	1-2	0.969	1-2-3	106.61
2	-0.5410	2-3	1.344	2-3-4	120.24
3	0.2297	3-4	1.342	2-3-7	116.14
4	-0.4903	4-5	1.447	3-4-5	113.49
5	0.7265	5-6	1.235	3-4-8	122.84
6	-0.5729	3-7	1.083	4-5-6	122.72
7	0.1150	4-8	1.080	4-5-9	116.55
8	0.1150	5-9	1.104	6-5-9	120.73
9	0.0000			7-3-4	123.62
				8-4-5	123.68

(d)				
<i>i</i>	Torsional parameter of single cosine term (kJ/mol)			
	$V_1^{(i)}$	$V_2^{(i)}$	$V_3^{(i)}$	$V_4^{(i)}$
1	-8.724	14.546	-2.076	-0.143
2	-3.133	9.910	-0.435	-0.470

<i>n</i>	Torsional parameter of cross cosine term (kJ/mol)			
	$V_{n,1}$	$V_{n,2}$	$V_{n,3}$	$V_{n,4}$
1	-0.052	0.326	0.026	-0.087
2	0.357	-0.395	-0.006	0.091
3	0.019	-0.043	-0.061	-0.051
4	-0.014	0.029	-0.028	0.022

TABLE 3-2. Comparison of energies of the rotamer II and the saddle point on the path from the rotamer I to II by the present extended OPLS-aa force field with those by the electronic calculations. The unit is in kJ/mol.

	ΔE of the rotamer II	Potential energy barrier from the rotamer I to II
Present force field	59.7	77.6
OPLS-aa	58.2	67.8
MP2/6-31G** [58]	58.6	82.1
B3LYP/6-31G** [58]	62.8	87.8
B3LYP/D95** [57]	63	85
BLYP/6-311G** [57]	60	87
HF/6-311G** [57]	49	64
HF/6-21G** [56]	51.2	66.1
HF/STO-3G** [56]		64.9

TABLE 3-3. (a) Potential energies of the four rotamers in vacuum obtained by the MO calculation (ΔE_{MO}), the ordinary OPLS-aa force field model (ΔE_{OPLS}), and the extended OPLS-aa force field model ($\Delta E_{EX-OPLS}$). The value in the parentheses represents the difference from ΔE_{MO} . (b) Potential energy barriers between the rotamers. The notation of the path between the rotamers is given in Figure 3-2. The unit is in kJ/mol.

(a)

	Rotamer			
	I	II	III	IV
ΔE_{MO}	0.00	58.6	44.6	46.8
ΔE_{OPLS}	0.00	58.2	41.4	39.8
	(0.00)	(-0.4)	(-3.3)	(-7.0)
$\Delta E_{EX-OPLS}$	0.00	59.7	45.5	47.0
	(0.00)	(+1.1)	(+0.8)	(+0.2)

(b)

	Path					
	A	B	C	D	E	E'
ΔE_{MO}	80.2	79.6	25.4	22.9	101.2	94.3
ΔE_{OPLS}	69.3	67.1	20.1	20.1	102.8	90.6
	(-10.9)	(-12.4)	(-5.3)	(-1.1)	(-1.6)	(-3.7)
$\Delta E_{EX-OPLS}$	81.1	79.6	24.1	22.3	104.6	91.8
	(+0.9)	(-0.0)	(-1.3)	(-0.6)	(+3.4)	(-2.5)

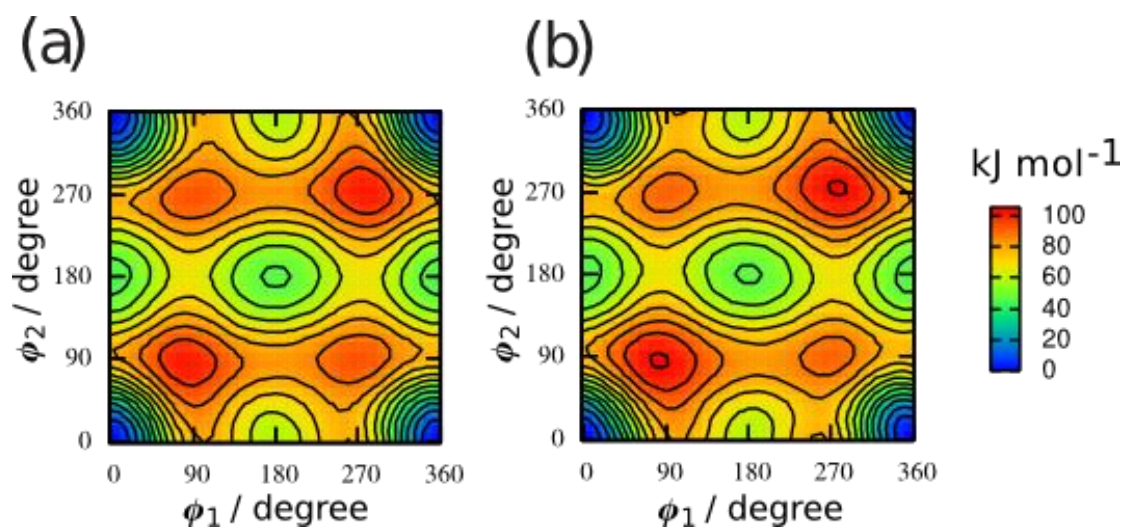


FIG. 3-1. Two-dimensional potential energy surface in vacuum as a function of ϕ_1 and ϕ_2 . (a) The original MO calculations (ΔE_{MO}) and (b) the calculated one from the extended OPLS-aa force field ($\Delta E_{\text{EX-OPLS}}$). The energy at $(0^\circ, 0^\circ)$ is set to be 0 kJ/mol, and the contour lines are drawn for every 8 kJ/mol.

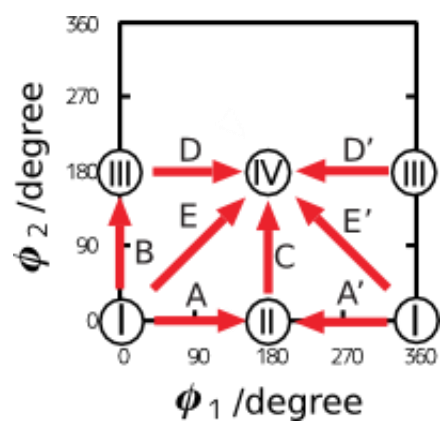


FIG. 3-2. Various linear paths between the rotamers. A and A' represent the paths from I to II, B the path from I to III, C the path from II to IV, D and D' the paths from III to IV, and E and E' the paths from I to IV. The symbols with a prime denote the paths that ϕ_1 moves toward the minus.

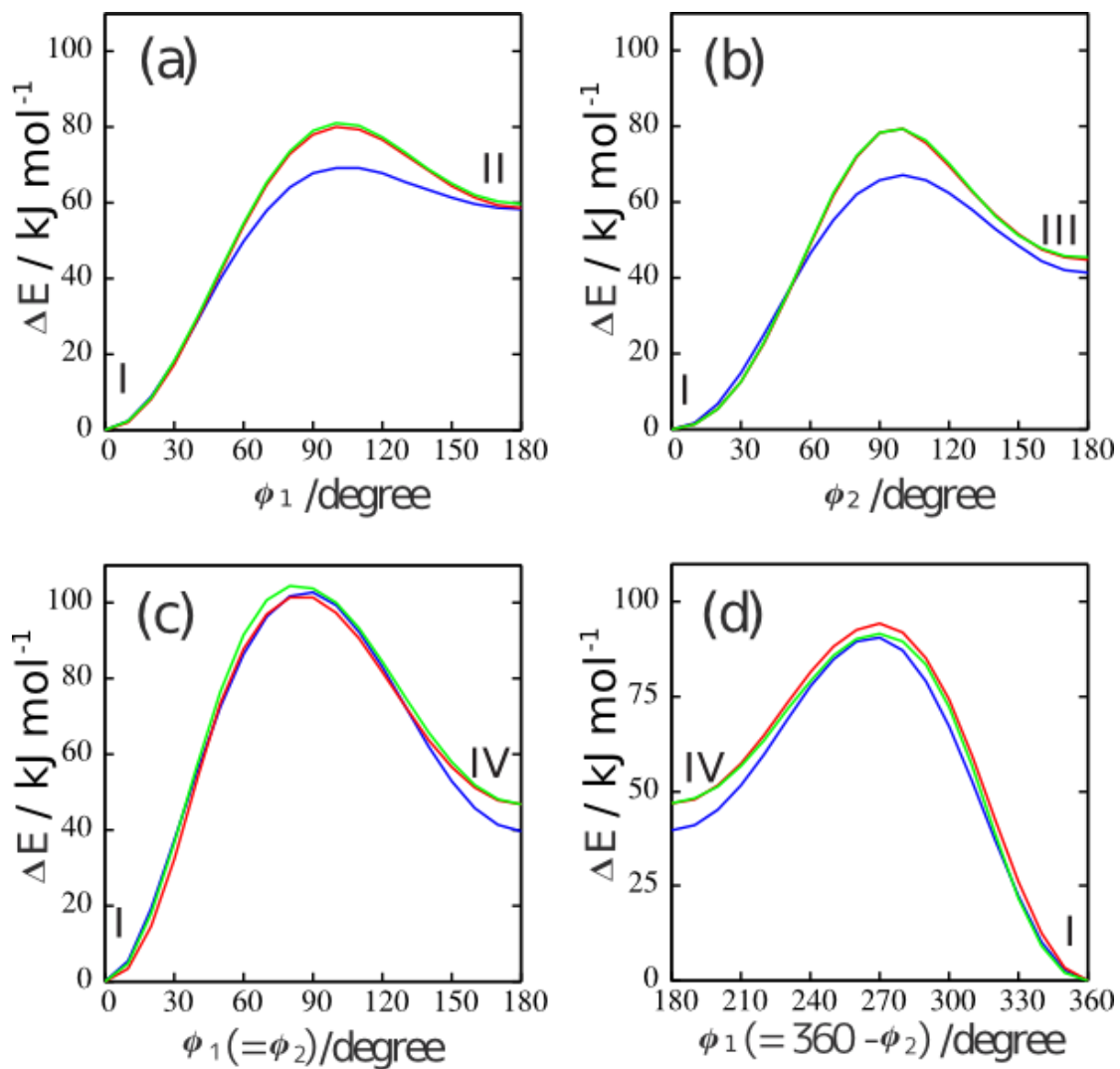


FIG. 3-3. The potential energy curves of the original MO calculation (ΔE_{MO} , red line), the ordinary OPLS-aa model (ΔE_{OPLS} , blue line), and the extended OPLS-aa model ($\Delta E_{\text{EX-OPLS}}$, green line) along the paths (a) A, (b) B, (c) E, and (d) E'.

IV. FREE ENERGY SURFACE FOR ROTAMERS OF *CIS*-ENOL MALONALDEHYDE IN WATER

A. Introduction

In this chapter, in order to investigate the thermodynamic stability of the rotamer I, which forms intramolecular hydrogen bonding structure, between the rotamers in water, we calculated two-dimensional free energy surface $\Delta G(\phi_1, \phi_2)$ as a function of two dihedral angles, ϕ_1 and ϕ_2 shown in Fig. 1-2, based on a series of MD calculations. Two models of malonaldehyde, flexible and rigid models, were investigated, where the former allows intramolecular vibrations and the latter constrains the intramolecular degrees of freedom except for ϕ_1 and ϕ_2 . The free energy surfaces have been evaluated by umbrella sampling method, and the free energy surface for the rigid model used as a biasing potential for the umbrella sampling calculation has been calculated preliminarily by the thermodynamic integration method. Occurrence of the hydrogen transfer reaction in the hydrogen bonding structure in water is discussed by the free energy barrier separating the rotamer I from other rotamers. Contribution of the intramolecular vibrations of malonaldehyde to the free energy surface is also presented.

B. Molecular dynamics calculations

Free energy calculation methods, umbrella sampling method and thermodynamic integration method, which were employed in this study, are described in section A. 2 of chapter II. In this section, details of calculations are presented.

Free energy surface, $\Delta G_{US}(\phi_1, \phi_2)$, is obtained from probability distribution of molecular conformation sampled by umbrella sampling MD calculations using artificial biasing potential. In general, it is difficult to find an efficient biasing potential which smoothes the potential energy

surface of a system of interest to the flat one. In this study, the biasing potential, ΔU_{bias} , was chosen to be the minus of conformational free energy surface for rigid model, $\Delta G_{\text{TI}}^{(\text{rigid})}(\phi_1, \phi_2)$, obtained by the thermodynamic integration method. The extended torsional potential function, Eqs. (1-1) and (1-2), was used for the function of ΔU_{bias} , where the parameters were fitted to reproduce $-\Delta G_{\text{TI}}^{(\text{rigid})}(\phi_1, \phi_2)$. For comparison, free energy surface for the rigid model has been calculated using the umbrella sampling method, too.

Considering the mirror symmetry of malonaldehyde, $\Delta G(\phi_1, \phi_2)$ must be the same as $\Delta G(360^\circ - \phi_1, 360^\circ - \phi_2)$. Thus, in the free energy calculations based on thermodynamics integration method, mean forces were calculated every 10° for the half of the ϕ_1 and ϕ_2 space. Then, total 648 points of ϕ_1 and ϕ_2 were investigated. Starting from the initial configurations, MD calculations have been performed for 230 ps for equilibration. After then, 300 ps-long MD calculations have been carried out to obtain satisfactory statistics for the mean force. In these calculations, all bond lengths, bond angles, and torsion angles of the double bond for malonaldehyde as well as torsion angles ϕ_1 and ϕ_2 were constrained.

In the umbrella sampling calculations, 24 independent equilibrated configurations with different ϕ_1 and ϕ_2 were prepared. Then, NPT ensemble MD calculation was carried out for 2 ns for each initial configuration. The calculations have been done for both rigid and flexible malonaldehyde. The bond lengths relevant to the hydrogen atoms were constrained even for the flexible model.

One malonaldehyde molecule and 725 water molecules were contained in a cubic simulation box with the periodic boundary condition. TIP4P model was adopted for water molecule and an extended OPLS-aa force field model which has increasingly improved torsional potential energy function, which was constructed in chapter III, was adopted for malonaldehyde molecule. The equation of motion was integrated by RESPA method [61] with a time step of 1 fs. The

temperature and pressure were controlled at 298.15 K and 1 atm, respectively, using the algorithm proposed by Martyna *et al.* [62]. Ewald method [47] was used to calculate the long range Coulombic interaction. Lennard-Jones interaction was cut off at 1.2 nm. The SHAKE/RATTLE and RATTLE/ROLL algorithms [47] were used for the constraints of the intramolecular degrees of freedom of water and malonaldehyde.

C. Results and discussion

1. Reliability of the free energy calculations

Table 4-2 shows the free energy differences between the rotamer I and IV, $\Delta G_{II}^{(rigid)}(180^\circ, 180^\circ)$, integrated along six different paths, I \rightarrow III \rightarrow IV, I' \rightarrow III' \rightarrow IV, I \rightarrow II \rightarrow IV, I \rightarrow IV, I' \rightarrow IV as shown in Fig. 4-1. The values agree well with each other indicating that the integration is independent of the paths as expected. The agreement shows a high reliability of our present free energy calculations by the thermodynamic integration method.

Further, the resultant distribution of ϕ_1 and ϕ_2 generated by the umbrella sampling calculation for the flexible and the rigid models is presented in Fig. 4-2. The figures clearly show that the whole configuration space with respect to ϕ_1 and ϕ_2 was sampled satisfactorily in both calculations. This guarantees a reliability of the resultant free energy surface for the rotamers.

Accuracy of the free energy calculation may also be examined by comparing the calculated free energy of the rotamers and the free energy barrier height among them between thermodynamic integration method and umbrella sampling method. The difference was less than 1 kJ/mol both for the free energy of the rotamers and the free energy barrier height among them.

Thus, we consider that our free energy calculations are highly reliable such that stability of the rotamers can be discussed quantitatively.

2. Contribution of intramolecular vibrations to the free energy

The calculated free energy curves between the rotamers I and II, I and III, and I and IV for the rigid and flexible models by the umbrella sampling method are shown in Fig. 4-3 together with the potential energy curve in vacuum. The curves for the two models agree well with each other, showing that the contribution of the intramolecular vibrations of malonaldehyde to the free energy surface is not significant. The difference between $\Delta G_{US}^{(rigid)}$ and $\Delta G_{US}^{(flexible)}$ is at most 2.6 kJ/mol, which is in the order of thermal energy. The intramolecular vibrations decrease the free energy difference slightly for most of the conformations.

3. Stability in water and in vacuum

Now, we consider the potential energy surface in vacuum, $\Delta E_{EX-OPLS}$, and the free energy surfaces in water, $\Delta G_{US}^{(flexible)}$ and $\Delta G_{US}^{(rigid)}$, shown in Figs. 4-1, 4-3, and 4-4. The figures show that the rotamer I is most stable both in vacuum and in water, and the other three rotamers are in local minima. The barriers from the rotamer I in water are lower than those in vacuum. The difference between $\Delta G_{US}^{(flexible)}$ and $\Delta E_{EX-OPLS}$ represents the contribution of the solvation to the free energy difference ignoring the intramolecular vibrations. The solvation decreased free energy difference as shown in Table 4-1(a) for the rotamers II, III and IV by -40.3, -22.0 and -26.9 kJ/mol, respectively, and lowered the barriers, too, as shown in Table 4-1(b) along the paths, I \rightarrow II, I \rightarrow III, II \rightarrow IV, III \rightarrow IV, I \rightarrow IV, and I' \rightarrow IV by -31.3, -20.3, +7.5, -4.6, -34.7, and -22.6 kJ/mol, respectively, showing strong effect on the stability. The solvation lowers all the barriers except for the path II \rightarrow IV. The contribution of the direct interaction with water solvent to the free energy differences are great. The order of the stability of the rotamers changes from I, III, and IV, II in vacuum to I, II, IV, and III in water. The order of the barrier heights from the rotamer I also changes

from the paths I \rightarrow III, I \rightarrow II, I' \rightarrow IV, and I \rightarrow IV in vacuum to I \rightarrow II, I \rightarrow III, I' \rightarrow IV, and I \rightarrow IV in water.

Difference in energy of three rotamers II, III, and IV in water from that of rotamer I was 33.19 kJ/mol, 30.38 kJ/mol, and 15.72 kJ/mol, respectively based on the PCM calculations [44]. This shows that the rotamer I is the most stable among the rotamers. This is the same as the present study. However, order of the stability of the three rotamers is different between two calculations. Further, the value of the energy is different by 4 – 14 kJ/mol. This may be caused by the fact that molecular structure of solvent was not taken into account in the PCM model.

4. Stability of the rotamer I

Now, we discuss about possibility of the proton transfer in water from the viewpoint of kinetic stability of the rotamer I. We have shown that, in the free energy surface of the rotamers, the rotamer I is surrounded by the free energy barriers which are higher than 50 kJ/mol as shown in Figs. 4-1, 4-3, and 4-4. Further, the energy barrier from the enol to the keto form in water cluster has been reported to be 47.3 kJ/mol [43]. This is not the result in bulk water, but indicates that the barrier height between enol and keto form is as high as the free energy barrier among the rotamers. In contrast, the height of free energy barrier for the proton transfer reaction in water is 8.8 kJ/mol according to the calculation by *ab initio* MD [63]. This is considerably lower than the torsional and isomerizing free energy barriers. This implies that the rotamer I can keep its conformation in water for much longer time than the time scale of the proton transfer reaction. Thus, the rotamer I may be used as a basic structure for which reaction coordinate of the proton transfer reaction is constructed.

D. Conclusion

Conformational free energy surfaces of the *cis*-enol malonaldehyde in water have been

evaluated by MD calculations. We showed that stability of the rotamers and free energy barriers to the different rotamers are significantly influenced by solvation. However, the rotamer I which has an intramolecular hydrogen bond and, thus, shows intramolecular proton transfer reaction is the most stable conformation among the rotamers in the *cis*-enol form both in water and in vacuum. Further, on the free energy surface, the rotamer I is surrounded by the very high free energy barriers. This means that the rotamer I is stable in water for a time much longer than the time scale of the proton transfer.

TABLE 4-1. (a) Potential energy of four rotamers in vacuum shown by the extended OPLS-aa force field ($\Delta E_{\text{EX-OPLS}}$) and the calculated free energy of the four flexible rotamers in water evaluated by umbrella sampling method ($\Delta G_{\text{US}}^{(\text{flexible})}$). The energies in water by PCM model at MP2/6-31G(p,d) level (ΔE_{PCM}) [44] are also shown. The potential energy and free energy of the rotamer at (0°,0°) are set to be 0 kJ/mol. (b) The potential energy and free energy barrier height $\Delta\Delta E_{\text{EX-OPLS}}$ and $\Delta\Delta G_{\text{US}}^{(\text{flexible})}$, respectively, among the rotamers. The errors show 90 % confidence interval.

(a)

	Rotamer			
	I	II	III	IV
$\Delta E_{\text{EX-OPLS}}$ (kJ/mol)	0	59.7	45.5	47.0
$\Delta G_{\text{US}}^{(\text{flexible})}$ (kJ/mol)	0	19.4±0.4	23.5±0.2	20.1±0.3
ΔE_{PCM} [44] (kJ/mol)	0	33.19	30.38	15.72

(b)

	Path					
	I → II	I → III	II → IV	III → IV	I → IV	I' → IV
$\Delta\Delta E_{\text{EX-OPLS}}$ (kJ/mol)	81.1	79.6	24.1	22.3	104.6	91.8
$\Delta\Delta G_{\text{US}}^{(\text{flexible})}$ (kJ/mol)	49.8±0.4	59.3±0.4	31.6±0.8	17.7±0.6	69.9±0.5	69.2±0.3

TABLE 4-2. The calculated free energy differences between the rotamer I and IV,

$\Delta G_{II}^{(rigid)}(180^\circ, 180^\circ)$, obtained by integrating six different paths.

Path	$\Delta G_{II}^{(rigid)}(180^\circ, 180^\circ)$ (kJ/mol)
I \rightarrow III \rightarrow IV	23.2
I' \rightarrow III' \rightarrow IV	23.1
I \rightarrow II \rightarrow IV	23.5
I' \rightarrow II \rightarrow IV	23.1
I \rightarrow IV	23.3
I' \rightarrow IV	23.4

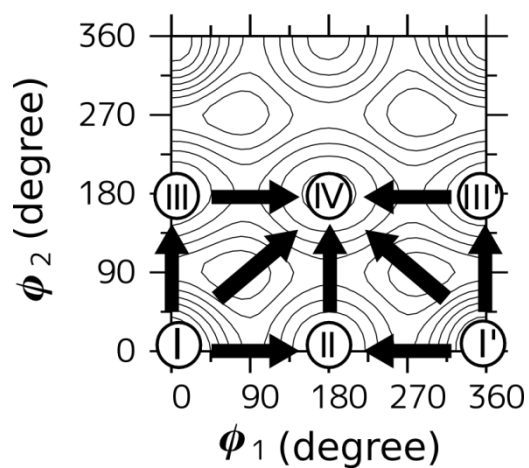


FIG. 4-1. The calculated free energy surface of the rotamers as a function of ϕ_1 and ϕ_2 . The rotamers I, II, III, and IV are located in free energy minima. Saddle points are found at the intermediates of the arrows, I \rightarrow II, I \rightarrow III, III \rightarrow IV, and II \rightarrow IV. Arrows, I \rightarrow IV and I' \rightarrow IV, cross mountains. Interval of the contours is 8 kJ/mol.

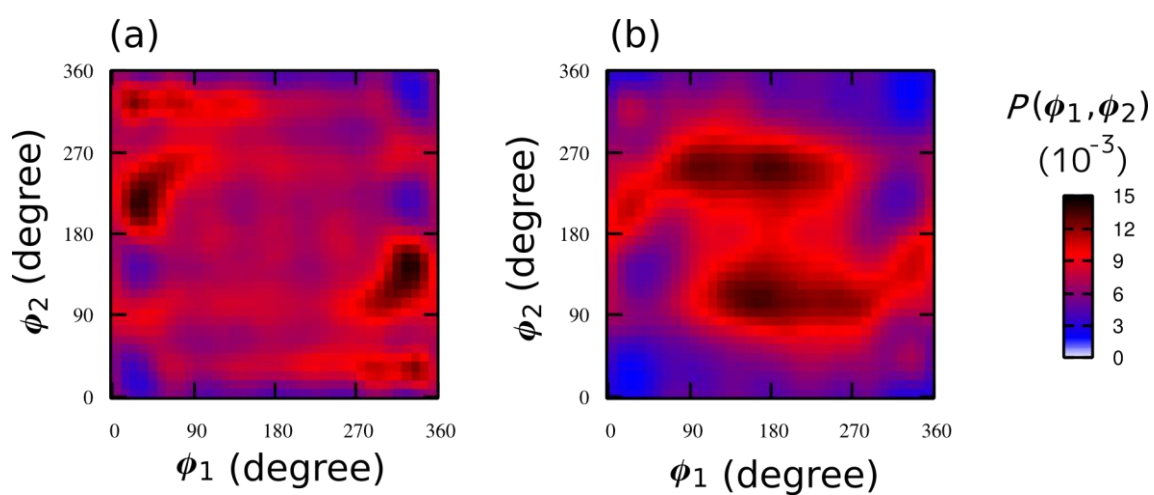


FIG. 4-2. The calculated two-dimensional distribution of ϕ_1 and ϕ_2 obtained by the umbrella sampling calculations for (a) rigid malonaldehyde and (b) flexible one.

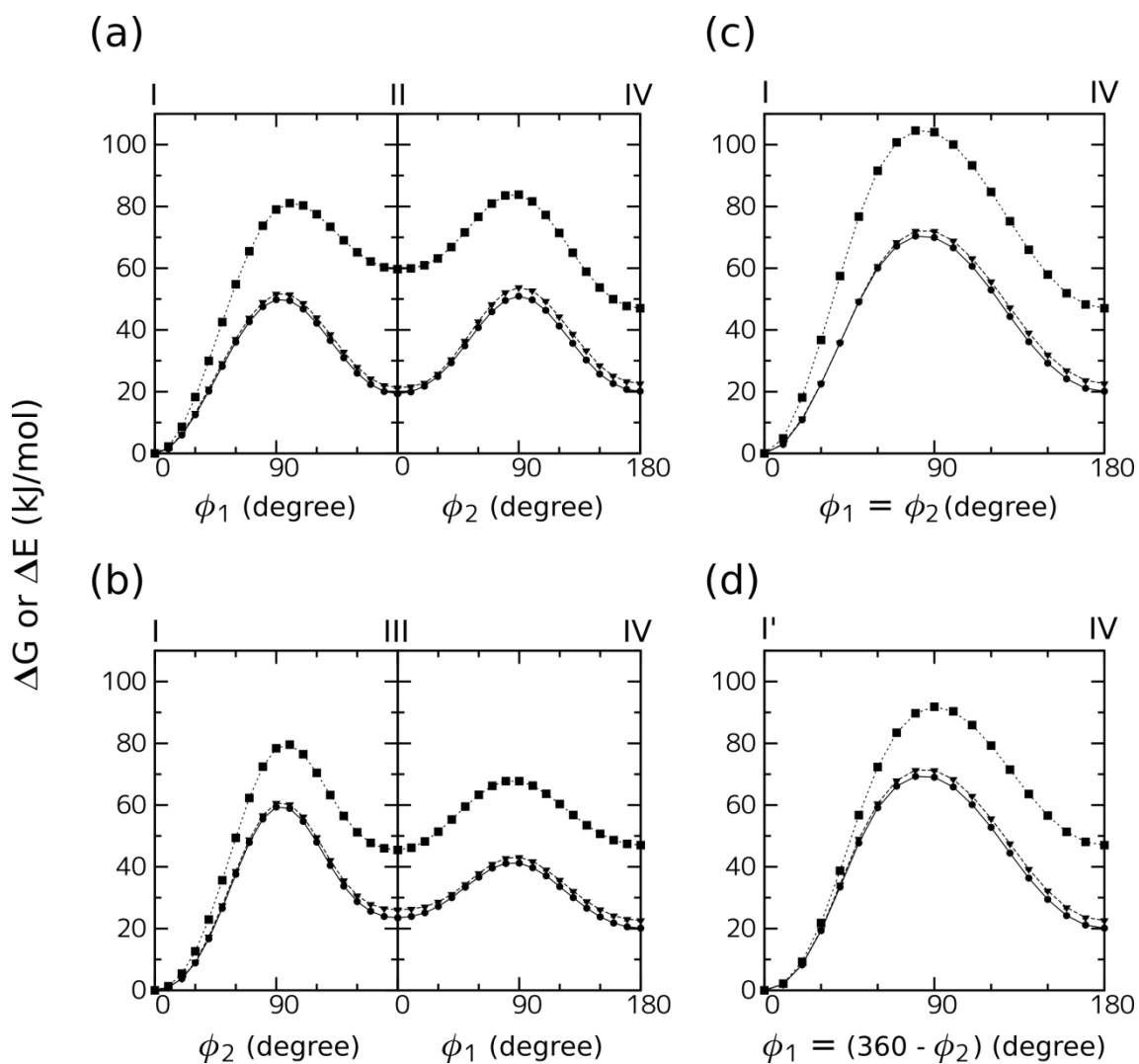


FIG. 4-3. Potential energy in vacuum (■) and the calculated free energy in water by umbrella sampling method (●: flexible malonaldehyde and ▼: rigid malonaldehyde) for rotamers as a function of ϕ_1 and ϕ_2 .

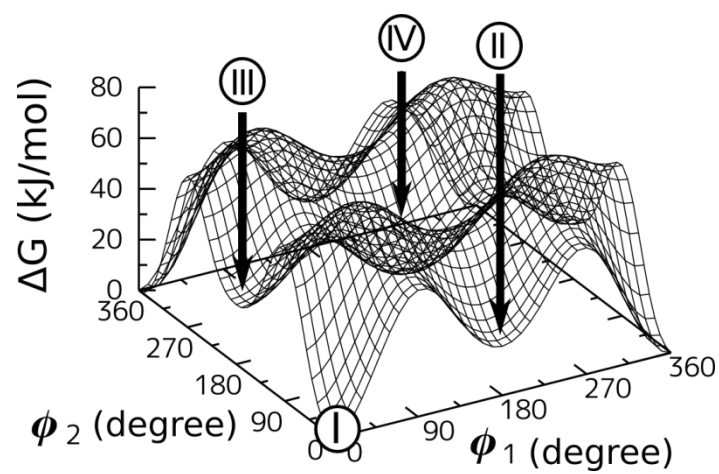


FIG. 4-4. Three dimensional description of $\Delta G(\phi_1, \phi_2)$, which corresponds to the contour map given in Fig. 4-1.

V. INTRAMOLECULAR PROTON TRANSFER REACTION OF MALONALDEHYDE IN WATER

A. Introduction

In this chapter, molecular dynamics calculation based upon mixed quantum-classical approximation (QCMD) for the proton transfer reaction of malonaldehyde (see Fig. 1-1) in water, that is protic polar solvent, have been carried out. Three reaction mechanisms, i.e. tunneling, thermal activation, and barrier vanishing reactions, have been analyzed in detail. Statistical analyses of the reaction rate and its mechanisms have also been investigated. The results are compared with the reaction obtained from quantum wave packet simulations in vacuum and full classical molecular dynamics (FCMD) calculations in solution in order to examine quantum effect as well as solvent effect on the reaction.

B. Molecular dynamics calculations

QCMD and FCMD calculations methods, definitions of state and reaction mechanisms and type of potential energy curve along the reaction coordinate, and analysis of the calculations are described in section II B. In this section, calculation conditions for the system of proton transfer reaction in water are described.

In the calculations, the flexible-SPC model [64,65] with the intramolecular vibrational degrees of freedom is adopted for water molecule. The intramolecular vibrational modes of the solvent molecule are very important for the vibrational excitation and relaxation of the solute even if some arbitrariness is included in the vibrational frequency of the model.

Fifty initial configurations where malonaldehyde molecule was immersed in solvent water consisting of 721 water molecules contained in a cubic cell with the side length of 28 Å in the

periodic boundary condition were prepared each for QCMD and FCMD. After equilibration run for the solvent at 298.15 K, QCMD and FCMD calculations were carried out in NVE ensemble for 110 ps, that is, total of 5.5 ns for each simulation. The initial 10 ps trajectories were excluded from the analysis, and then, total of 5 ns were used for the analysis. Equations of motion for the classical atoms in QCMD and FCMD were solved with a time step of 0.1 fs, while the equation of motion for the quantum system in QCMD was integrated with a time step of 0.0005 fs. The intermolecular potential was cut-off for the non-bonded pair whose distance is longer than 13 Å, where switching function was applied between 12 and 13 Å.

Time evolution of the wave function on the effective one-dimensional potential curve in vacuum was obtained by solving the equation of motion given by Eq. (A-5) with Hamiltonian of the solute presented by Eq. (2-7) [27]. Initial states of the calculation will be explained in Results and Discussion section.

C. Results and discussion

1. Examples of trajectory of reaction

First of all, we describe typical trajectories obtained from our calculations. Characteristics of the dynamical behavior of various proton transfer reaction mechanisms in FCMD and QCMD are examined in relation to solute-solvent interactions.

1-1. FCMD calculation

An example of the time evolution of $q(t)$ for 20 ps obtained from FCMD is shown in Fig. 5-1(a). Position of q^\ddagger in vacuum was defined to be zero in the figure. Then, proton transfer reaction may be described by crossing $q=0$. In solution, q^\ddagger changes as a function of t and is not always located at $q = 0$. But the change is small such that we can define the reaction in solution by q^\ddagger

crossing zero value in the same way as the case in vacuum. As shown in the figure, the reaction occurs frequently in solution. However, successive crossings occur in pico or subpico second as found, for example, around $t=7$ ps. That is, the system moves from the reactant well to the product one once, but it returns quickly back to the reactant well without stabilization of the product state. This is recrossing. In contrast, in vacuum, the trajectory of $q(t)$ for 20 ps obtained at 298.15 K, which is one-dimensional motion on $V_0^{eff}(q)$, presented in Fig. 5-1 (b) shows that reaction does not occur. This is because the kinetic energy at room temperature, about 1.3 kJ/mol, is less than the barrier height of about 6.3 kJ/mol of V_0^{eff} . The solvent, thus, facilitates proton transfer reaction significantly.

1-1-1. Thermal activation reaction

Trajectory of the classical system for 2 ps from $t=75$ ps to 77 ps is presented in Fig. 5-2. Fig. 5-2(a) shows the time evolution of $q(t)$. The $q(t)$ moved from the left well to the right one at 76.1 ps (the vertical dotted line) and stayed there. Time evolution of the barrier heights $\Delta V(t)$ measured from the minimum of the left well (blue) and right one (red) is presented in Fig. 5-2(b), and the energy difference $V_0(q^P) - V_0(q^R)$ between the two minima is drawn in black, too, such that it is positive if the left well is more stable than the right one and negative vice versa. The left well, that is, the reactant state at 75.0 ps was more stable than the right well, the product state, by 10 kJ/mol, then, the barrier heights from the right and left wells were 10 kJ/mol and 0 kJ/mol, respectively. For $t = 75.1 \sim 75.5$ ps, energy difference between the left and right wells fluctuated significantly such that the left well is sometimes more stable and at other times less stable. Then, the barrier height from the left well ranged from 1 kJ/mol to 10 kJ/mol. However, the reaction did not occur because the kinetic energy of the solute was small. After $t = 75.5$ ps, the left well was stabilized comparing the right one and the barrier height from the left well increased. The potential

curve at $t=75.75$ ps is shown in Fig. 5-2(a-1). After $t=75.75$ ps, but before the reaction, $q(t)$ fluctuated more in the left well (Fig. 5-2(a)). According to the present definition of the potential curve, interactions of the system of interest with the environment are all included in the potential energy curve. Then, no external force acts on the system. Change in the potential curve as a function of time drives the motion of $q(t)$. Thus, the large amplitude of $q(t)$ found above indicates that the system was activated by the interaction with the environment through the change in the potential curve. Then, the barrier height from the left well decreased by chance. Figure 5-2(c) shows the time evolution of the distance between two minimum points q^R and q^P . Until $t=76.0$ ps, the distance fluctuated around the value which is the same as that in vacuum, $1.6 \text{ \AA}(\text{g/mol})^{1/2}$ (a horizontal dotted line), however, from $t=76.0$ ps, the minima decreased their distance from 1.8 to $1.0 \text{ \AA}(\text{g/mol})^{1/2}$, which is much shorter than the one in vacuum. Then, the barrier height from the left well was lowered to 5-10 kJ/mol. The lowering of the barrier was enough for the activated system in the left well to move to the right well overcoming the barrier. Thus, thermally activated reaction took place (Fig. 5-2(a-2) and (a-3)). Around $t=76.6$ ps after the reaction, the product state was stabilized by the solvation by about 10 kJ/mol (Fig. 5-2(a-4)). Unplotted region in the figures around $t=76.7$ ps and 76.8 ps represents strongly-asymmetric-single-well potential energy curve.

1-1-2. Barrier vanishing reaction

An example of the trajectory of barrier vanishing reaction obtained from FCMD is shown in Fig. 5-3, where $q(t)$, the barrier heights and the energy difference $\Delta V(t)$, and the distance between two wells d are plotted as a function of time in Fig. 5-3(a), (b) and (c), respectively, in the same way as the previous example shown in Fig. 5-2. The right well represents the reactant state for small t which was more stable than the left one until $t = 38.4$ ps (see the black line in Fig. 5-3(b) and Fig. 5-3(a-1)). In this time region, reaction did not occur due to the deep well of the right

reactant well produced by solvation. After $t = 38.4$ ps, the barrier height from the right well (the red line in Fig. 5-3(b)) decreased and energy level of the two wells became equal. The distance between two stable points (Fig. 5-3(c)) greatly changed for $t = 38.5 - 38.6$ ps. The distance significantly decreased from $2.0 \text{ \AA}(\text{g/mol})^{1/2}$ to $0.5 \text{ \AA}(\text{g/mol})^{1/2}$ and, at the same time, the barrier from the wells vanished, and then, the reaction took place at $t = 38.6$ ps (Fig. 5-3(a-2)). This is the barrier vanishing reaction. After the reaction, the distance between the two wells increased forming again a double-well. The left well was then stabilized more than the right one after $t = 39.0$ ps (Fig. 5-3(a-3)). Unplotted region in the figures represents strongly-asymmetric-single-well potential curve.

1-2. QCMD calculation

1-2-1. Tunneling reaction

First example of trajectory obtained from QCMD is presented in Fig. 5-4. The gray solid and dotted lines in Fig. 5-4(a) represent energy levels of the vibrational state in the left and right wells, respectively. Colored line represents the occupied vibrational state and change in color from red to blue shows the change in the occupied state from the right well to the left well, respectively.

Tunneling transfer from vibrational ground state in the right well to the ground state in the left well was found at $t = 11.517$ ps (the vertical dotted line in Fig. 5-4). The figure was expanded around $t = 11.5$ ps in order to observe the tunneling in more detail (see the inset (a-i) in Fig. 5-4(a)). When the transition occurred, the energy levels were very close between reactant and product states. The small energy difference between them, about 0.1 kJ/mol , was absorbed by the solvent.

Difference between two ZPE levels in the right and left wells ($= \epsilon_1^{(P)} - \epsilon_1^{(R)}$) in the trajectory is presented by the black line in Fig. 5-4(b). This is positive if the ZPE in the left well is lower than the one in the right well and negative vice versa. Blue and red lines represent the barrier

heights measured from the ZPEs in the left and right wells, respectively. The figure shows that the black line was negative at small t , that is, energy of the vibrational ground state occupied by the system was lower than that in the unoccupied left well until $t = 11.0$ ps (Fig. 5-4(a-1)). The energy difference began to decrease (Fig. 5-4(a-2)) and, at $t = 11.5$ ps, the energy level was almost the same between the two wells. Then, the tunneling transfer occurred when the barrier height was about 5 kJ/mol (Fig. 5-4(a-3)). This indicates that the thermal fluctuation by the solvent helped the tunneling reaction adjusting the energy level of the two wells. After the reaction, energy of the left well was lowered by about 10 kJ/mol compared with the right well (Fig. 5-4(a-4)) by solvation here, too.

Figure 5-4(c) shows the distance d between two minima of the wells ($=q^P - q^R$). In this trajectory, the distance fluctuates around the value in vacuum, $1.6 \text{ \AA} (\text{g/mol})^{1/2}$, which indicates that the distance between two wells is not very important for the tunneling reaction.

1-2-2. Thermal activation reaction

Second example of trajectory obtained from QCMD is presented in Fig. 5-5 in a similar way to Fig. 5-4. Blue and green colors represent the state in the left well and red and orange colors in the right well. Initially, the system was found in the ground state in the left well (blue line) and, then, vibrational excitation to the first excited state (green line) occurred around $t = 91.1$ ps. The system was relaxed to the ground state in the same well around $t = 91.2$ ps. In this case, the reaction did not occur. After then, the solute stayed in the ground state in the left well stabilized by solvation (Fig. 5-5(a-1)). The barrier began to decrease its height at about $t = 91.7$ ps. The vibrational excitation to the first excited state occurred again (green line) (Fig. 5-5(a-i) and (a-2)). Energy difference of about 3.8 kJ/mol required for the vibrational excitation was provided by the surrounding solvent. It was followed by transition from the first excited state in the left well (green line) to the first excited state in the right well (orange line) at $t = 92.01$ ps as shown in Fig. 5-5(a-ii) and (a-3). The barrier

height was as low as about 3 kJ/mol, which is lower than the energy levels of the excited states as presented in Fig. 5-5(b). This is thermally activated reaction. Above the barrier, wave functions of the two states overlap sufficiently to give a high probability that the transition occurs. After the transition to the right well occurred, the right well was stabilized by the solvation. During this stabilization, the system was tentatively relaxed to the ground state (red line) around $t = 92.1$ ps and, then, vibrational relaxation from the first excited state (orange line) to the ground state (red line) occurred in the right well at $t = 92.22$ ps as shown in Fig. 5-5(a-4) and (a-iii). The right well was stabilized further as shown in Fig. 5-5(a-5). The reaction was then completed. The relaxation energy of 3.1 kJ/mol was absorbed by the solvent. The distance between two wells shown in Fig. 5-5(c) fluctuated around the value in vacuum (horizontal dotted line), which indicates that the distance is not important for the thermal activation reaction.

1-2-3. Barrier vanishing reaction

Third example obtained from QCMD is presented in Fig. 5-6. Initially, the solute was in the ground state of the left well stabilized by solvation as shown in Fig. 5-6(a-1) and (b). The barrier was lowered from $t = 81.75$ ps to 82.25 ps, though reaction did not occur. The system was excited twice to the first excited state in the left well at $t = 82.4$ ps and 82.55 ps (green lines) though the system was relaxed to the ground state. At $t = 82.6$ ps, the left well began to become shallow and the barrier was lowered. And, finally, it became negative as shown in Fig. 5-6(b), that is, the barrier was below the ZPEs. Then, the transition from the ground state in the left well to the ground state in the right well occurred (vertical dotted line). Shape of the potential was then quasi-symmetric-single-well. This is the barrier vanishing reaction. The reaction is clearly shown in the inset (a-i) of Fig. 5-6. Difference between two energy levels, the reactant and product states, was 0.05 kJ/mol. This small energy was provided by the solvent. After the reaction, the product state was

stabilized by the solvent reorganization by about 10 kJ/mol compared with the reactant one.

As clearly found in Fig. 5-6 (b) and (c), a correlation is found between the barrier height and the distance between two potential energy minima. When the barrier is high, for example, at $t = 82.3$ ps and 82.5 ps, the distance is long, and in contrast, when the barrier is low, for example, at $t = 82.2$ ps and 82.9 ps, the distance is short. In particular, when the barrier disappeared at the reaction at $t = 82.735$ ps, the distance was as short as $0.5 \text{ \AA}(\text{g/mol})^{1/2}$, which is much shorter than the value in vacuum, $1.6 \text{ \AA}(\text{g/mol})^{1/2}$. Thus, short distance between the two wells is closely related to the low barrier, giving rise to proton transfer reaction due to high transition probability coming from the large overlap of wave functions between the reactant and product states.

As shown in the above examples of three reaction mechanisms found in the trajectory, quantum effect and thermal fluctuation of the reaction potential energy curve caused by solute-solvent interaction are both very important for proton transfer reaction in solution.

2. Statistics of the reaction

In this subsection, statistics of the reactions is investigated with respect to the reaction mechanisms of QCMD and FCMD shown in the previous subsection, then, quantum and solvent effects are discussed.

2-1. Potential energy curve in solution and its thermal fluctuation

First, shape of the potential energy curve in solution, V_0 , is examined. The shape of the potential curve was classified into three, i.e. double-well, strongly-asymmetric-single-well, and quasi-symmetric-single-well already presented in Fig. 2-3(a), (b), and (c), respectively. Ratio of these three averaged over all trajectories obtained by QCMD is listed in Table 5-1. The table shows that the double-well was most frequently found in the trajectories, i.e. 61%, and the ratio of the

strongly-asymmetric-single-well was 38%. The quasi-symmetric-single-well was scarcely found, i.e. only 1.3%, the relevant state being regarded as the transient state from the viewpoint of chemical reaction.

The calculated distribution of difference in the level of ZPE between occupied and unoccupied wells, $\varepsilon_1^{(unocc)} - \varepsilon_1^{(occ)}$, is presented in Fig. 5-7, where red, green, and blue lines represent the probability density distributions found for the double-well, strongly-asymmetric-single-well, and quasi-symmetric-single-well, respectively. The energy difference in vacuum is 0 by definition, whereas, for the double-well in solution, peak of the distribution is found at about 4.1 kJ/mol and the distribution is not symmetric with respect to 0 ranging from -12 kJ/mol to 25 kJ/mol. This implies that the occupied potential well is stabilized by solvation but has fluctuation which is large enough for the unoccupied potential well to be often lower than the occupied well. Peak of the distribution for the strongly-asymmetric-single-well is found at about 10 kJ/mol and the distribution ranges from -15 kJ/mol to 30 kJ/mol. The energy difference between ZPEs for the strongly-asymmetric-single-well is, thus, greater than that for the double-well. A dip in the distribution for the strongly-asymmetric-single-well at 0 kJ/mol comes from the definition of the potential well type, because the potential curve for which difference in ZPE is zero is classified into the quasi-symmetric-single-well. The distribution of the quasi-symmetric-single-well has a peak at 0 kJ/mol.

The calculated distribution of barrier height measured from the ZPE in the occupied well, ($= V_0(q^\ddagger) - \varepsilon_1^{(occ)}$), is shown in Fig. 5-8, where red and green lines show the probability density distribution for the double-well and the strongly-asymmetric-single-well, respectively. Peak of the distribution is found at about 6.5 and 9.0 kJ/mol for the former and the latter, respectively. The barrier height from the occupied well in solution is higher than that in vacuum by about 4.6 kJ/mol. This is due to the stabilization of the occupied well by solvation, which is the same as the case of

energy difference between ZPEs shown in Fig. 5-7.

Thus, solute - solvent interactions stabilize potential well of the occupied state leading to asymmetric shape with high barrier. Thermal fluctuation of the solute-solvent interactions significantly affect the potential energy curve as a function of time, which facilitates proton transfer reaction compared with the one in vacuum.

2-2. Reaction rates

Here, we investigate proton transfer reaction rate. Distribution of time interval between a transfer and the succeeding one from a state to the other defined in subsection II B 4 is plotted logarithmically in Fig. 5-9(a), where the red and green plots indicate the results obtained from QCMD and FCMD, respectively. Total numbers of proton transfer found in the whole trajectories for 5 ns were 24109 and 5784 for QCMD and FCMD, respectively. Both distributions decrease with increasing time interval between the succeeding transfers. If these transfers are independent of each other, that is, the Poisson process, they must show an exponential distribution. Then, they must show a linear line in the logarithmic plot in Fig. 5-9(a). Though the plots follow linear lines for large t_{interval} , non-linear behavior for small t_{interval} indicates that the proton transfers with short intervals are not independent of each other. One example is recrossing. In particular, very frequent back and forth transitions between reactant and product states are found for the quantum excited state near the barrier height. Similar behavior is also found for both classical and quantum systems when the barrier itself is near the ZPE and classical thermal energy, respectively. The recrossing is not regarded as reaction. In the figure, a border is found at $t_{\text{interval}} = 150$ fs between non-linear and linear regions. Period of classical oscillation in an effective potential well in vacuum is about 130 fs, which supports the above choice that the transfers shorter than 150 fs are not counted as reaction. Logarithmic plot of the observed time interval of the reaction excluding the frequent back and forth

transfers is presented in Figs. 5-9(b). We can see from Fig. 5-9(b) that the plots show linear lines for both QCMD and FCMD. Thus, the proton transfer reactions presented in Fig. 5-9(b) follow the Poisson process and are independent of each other. Now, we can consider that these are all reactive transfers.

In Table 5-2, total number of reactions found in 5 ns-long simulations, average interval, and reaction rate are listed for quantum and classical systems in water. Relevant quantities for the reaction in vacuum are presented, too. The total number of reactions were 3511 and 1790 for QCMD and FCMD, respectively. Then, on average, reaction takes place every 1.4 ps and 2.8 ps in QCMD and FCMD, respectively. The reaction rate are given to be 0.70 ps^{-1} and 0.36 ps^{-1} for QCMD and FCMD, respectively. The reaction rate is about 2 times greater for the quantum system than that for the classical one, indicating that the quantum effect is great for the proton transfer reaction.

Reaction time and reaction rate in vacuum at room temperature were estimated as follows. One-dimensional quantum wave packet calculations were carried out starting from four initial states, i.e. each of the lowest four vibrational states in the reactant well. Time needed for the transition from one side to the other in the double-well, that is, the reaction time, was measured. The average time was defined to be the Boltzmann average of the four times at room temperature. The reaction rate is, then, given by the reciprocal of the average reaction time. The calculated reaction time was 3.72 ps. In contrast, the average time interval obtained from QCMD in solution was 1.4 ps, which is 2.5 times shorter than that in vacuum. This indicates that the reaction is enhanced significantly by the solvent. As shown in Fig. 5-8, peak position of the distribution of potential barrier height in solution is higher than that in vacuum. Taking this observation solely into account, reaction in solution should be more difficult to occur than in vacuum. However, the calculations show the opposite result that the reaction rate is greater in solution than in vacuum. Figure 5-8 clearly shows that the barrier height distributes broadly in solution, too, according to which very low barriers, for example < 2

kJ/mol, are very frequently observed. Then, the system easily get over the barrier. The large thermal fluctuation by the solvent can give many opportunities for the system to give rise to reactions.

2-3. Reaction mechanisms

As discussed above, proton transfer reaction has three mechanisms, that is, tunneling reaction, thermal activation reaction, and barrier vanishing reaction. Contribution of these three to the total reaction for 5 ns is presented in Table 5-3. The number of tunneling reactions in QCMD was 1168 and its ratio was 33%. This shows significant contribution. However, the thermal activation reactions occurred 1625 and 1399 times in QCMD and FCMD, respectively, showing the largest contribution among the various mechanisms. The thermal activation reaction in QCMD is more frequently found than that in FCMD. The difference may be caused by the presence of the ZPE in QCMD. The number of barrier vanishing reactions in QCMD and FCMD were 718 and 391, respectively. They are both about one fifth of the total reactions and shows small contribution. Further, barrier vanishing reactions are found more frequently in QCMD than in FCMD. This comes not only from the ZPE in QCMD but also from the difference in the definition of vanishment of the barrier between QCMD and FCMD. Vanishment of the barrier in QCMD was defined by comparing the barrier height with the ZPE (~ 1.55 kJ/mol). In contrast, in FCMD, the barrier height was compared with the thermal energy $kT/2$ (~ 1.26 kJ/mol). Thus, the barrier vanishing reaction in QCMD may be easier to occur than in FCMD.

Now, reaction mechanism of quantum tunneling effect is analyzed in detail. Calculated probability density distribution of the barrier height measured from the ZPE in the reactant well when the tunneling reaction is going to occur is shown by solid black line in Fig. 5-10. The barrier height from ZPE in the occupied well in the double well sampled from the whole trajectory of QCMD is shown, too, by dotted black line. This corresponds to the normalized distribution of the

red line in Fig. 5-8. The figure shows that tunneling reactions occur dominantly from ZPE when the barrier height is lower than 5 kJ/mol in spite of the fact that the distribution of the barrier height sampled all over the trajectories of the whole QCMD is very broad as shown by the dotted line in Fig. 5-10. This implies that the tunneling reactions occur selectively for the state having low barrier height. When the height of the barrier measured from the occupied state of interest is low, overlap of the wave functions of the reactant and product states is large. This gives high tunneling probability to the system.

Number of reactions other than tunneling, that is, summation of thermal activation reaction and barrier vanishing reaction, are 2343 and 1790 in QCMD and FCMD, respectively. The ratio between them is 0.76. This can be roughly explained by the ZPE which is taken into account solely in QCMD. Using the transition state theory, the difference in the energy level between QCMD and FCMD, i.e. the ZPE, 1.55 kJ/mol, gives the ratio of 0.54.

D. Conclusion

Mixed quantum-classical MD calculations have been applied to intramolecular proton transfer reaction of malonaldehyde in solution. Trajectories obtained from the calculations have been analyzed. The reaction was classified into three, i.e. tunneling reaction, thermal activation reaction, and barrier vanishing reaction. The trajectories presented a microscopic view for the reaction which utilizes thermal fluctuation by the solvent. In particular, barrier height and energy difference between the reactant and product wells play a very important role in the reaction. In other words, solute-solvent interactions are essential for the reaction. Ratios of contribution of three reaction mechanisms were calculated quantitatively. This clearly shows that the tunneling and thermal activation reactions are very important. In addition to the mixed quantum-classical calculation, the fully classical calculation in solution and quantum wave packet calculation in vacuum have been

carried out for reference and the reaction rate was investigated. The calculations showed that the quantum and solvent effects promote the reaction. The reaction in solution is likely that the quantum and solvent effects give rise to complexity in the reaction. In particular, the thermal fluctuation, which is not found in the gas phase, plays an essential role in the reaction.

In the framework of mixed quantum-classical calculations, the surface-hopping approximation has been adopted here. The approximation simplifies the view of reactions. However, quantum coherence between vibrational states remained to be solved. The real systems must show more complicated behavior, where loss and recovery of the coherence between the states occur simultaneously and continuously. In order to describe such systems, further understanding of the decoherence and further development of the quantum simulation methods are required. This is a subject to be solved in future.

In the next chapter, we show calculation results for the intramolecular proton transfer reaction in non-polar solvent. Comparing the reaction in neon with the reaction in water, diversity of the reaction mechanism in the different solvents can be seen. Further, comparing the calculations with the theory such as Marcus theory and experimental results, we can make more detailed discussions for quantum and solvent effects for the proton transfer reactions in solution.

TABLE 5-1. The calculated ratio of the potential wells found in the trajectories of QCMD. The statistical error represents 90% confidence interval.

Potential well	Ratio(%)
Double-well	61 ± 1
Strongly-asymmetric-single-well	38 ± 1
Quasi-symmetric-single-well	1.3 ± 0.1

TABLE 5-2. Number of reactions in 5 ns-long trajectories, average time interval between reactions, and reaction rate in solution, and the average reaction time and reaction rate in vacuum at 298.15 K.

The statistical error represents 90% confidence interval.

	Quantum	Classical
In solution		
Total number of reactions	3511	1790
Average interval (ps)	1.4 ± 0.1	2.8 ± 0.1
Reaction rate (ps^{-1})	0.70 ± 0.02	0.36 ± 0.02
In vacuum		
Average interval (ps)	3.72	(no reaction)
Reaction rate (ps^{-1})	0.27	(no reaction)

TABLE 5-3. Number of reactions for three reaction mechanisms in solution. The ratios are presented in the brackets with the statistical errors given by 90% confidence interval.

	QCMD	FCMD
Tunneling reaction	1168 (33 ± 2 %)	-
Thermal activation reaction	1625 (46 ± 3 %)	1399 (78 ± 3 %)
Barrier vanishing reaction	718 (21 ± 1 %)	391 (22 ± 1 %)

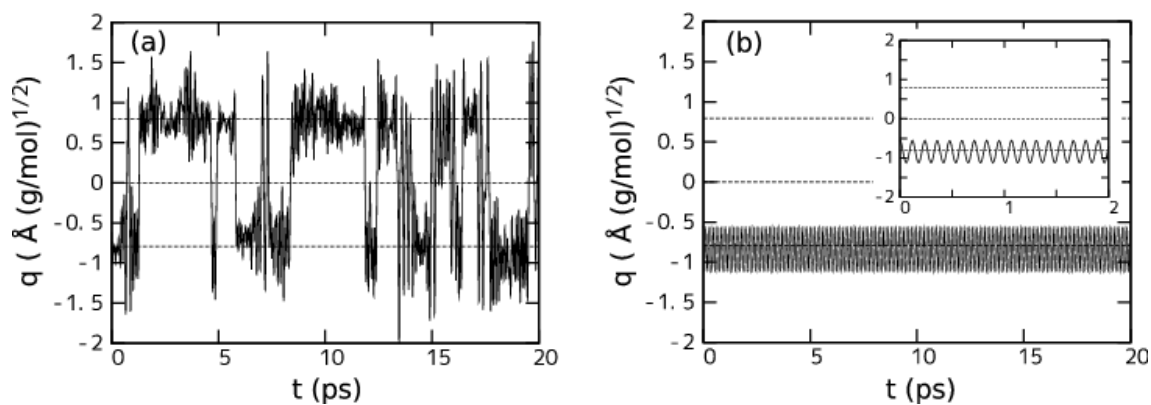


FIG. 5-1. (a) Time evolution of $q(t)$ obtained by FCMD in solution (solid line) and (b) time evolution of $q(t)$ obtained by classical simulation in vacuum (solid line). Stable point in the reactant well ($q = q^R = -0.8 \text{ \AA}(\text{g/mol})^{1/2}$), the one in the product well ($q = q^P = 0.8 \text{ \AA}(\text{g/mol})^{1/2}$), and the transition state ($q = 0 \text{ \AA}(\text{g/mol})^{1/2}$) in vacuum are also indicated by the dotted lines.

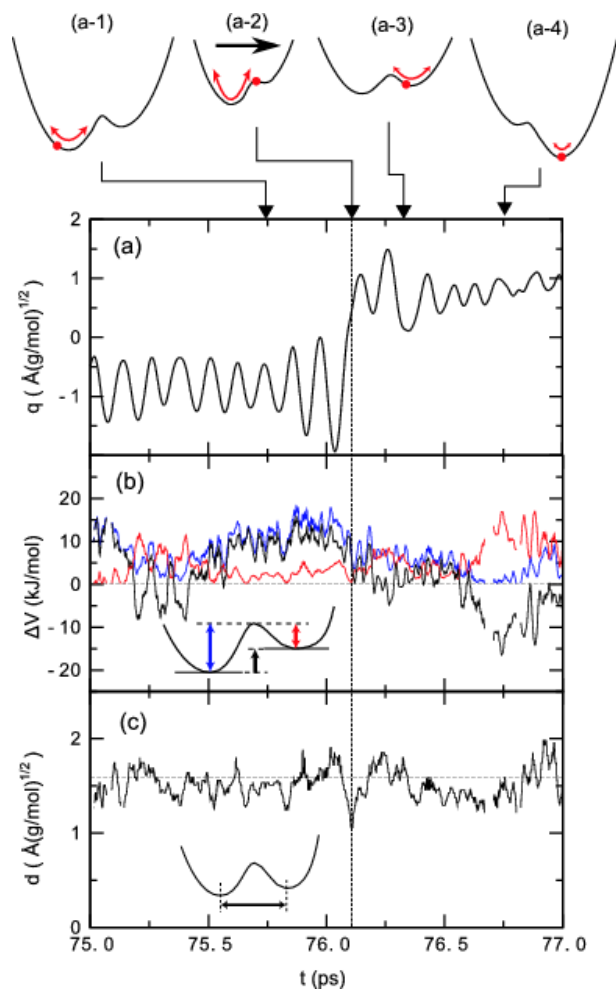


FIG. 5-2. An example of thermal activation reaction found in FCMD. (a) $q(t)$, (b) the barrier heights measured from the minimum in V^R and V^P (blue and red lines, respectively), and the energy difference from the minimum in the left well to the one in the right well (black line), and (c) the distance d between the minima in two wells.

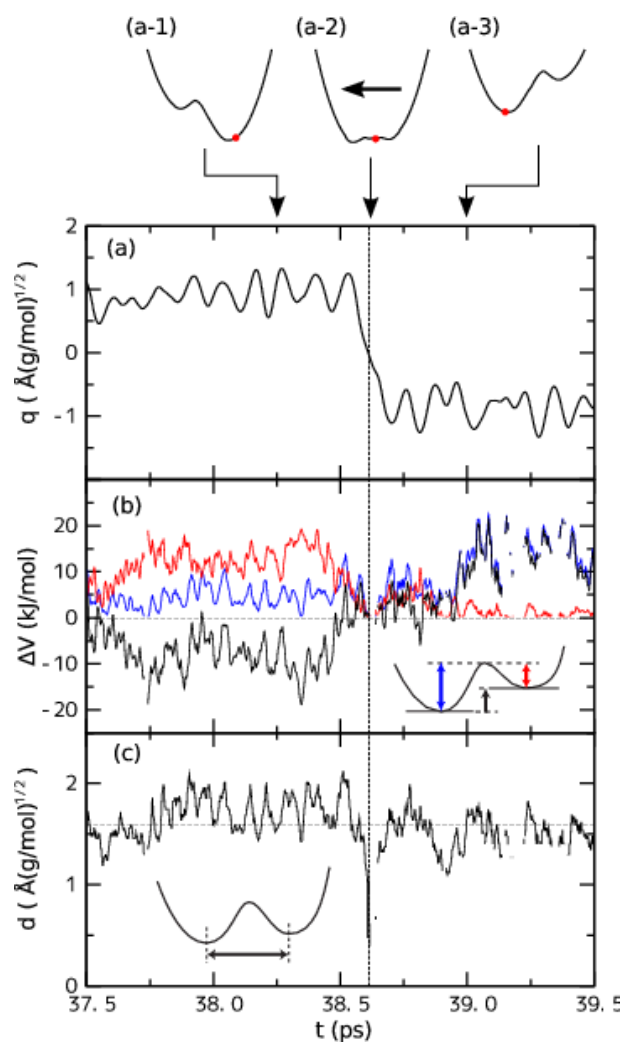


FIG. 5-3. An example of the barrier vanishing reaction found in FCMD. (a) $q(t)$, (b) the barrier heights measured from the minimum in V^R and V^P (blue and red lines, respectively), and the energy difference from the minimum in the left well to the one in the right well (black line), and (c) the distance d between the minima in two wells.

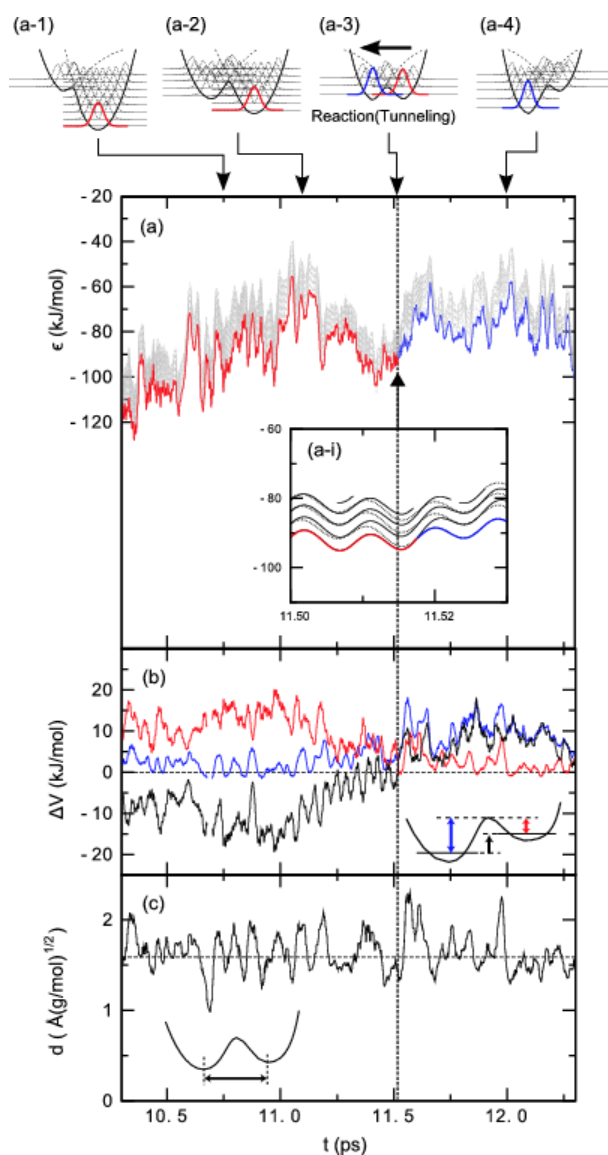


FIG. 5-4. An example of tunneling reaction found in QCMD. (a) Time evolution of the energy level of the vibrational state. Gray solid and dotted lines indicate the vibrational state in V^R and V^P , respectively. The color represents the occupied vibrational state (blue: vibrational ground state in the left well and red: vibrational ground state in the right well). The color changes on the transition. (b) Barrier height measured from the ZPEs in V^R and V^P (blue and red lines, respectively), and energy difference $\epsilon_1^{(P)} - \epsilon_1^{(R)}$ from the ZPE in the left well to the one in the right well (black line). (c) Distance $d(=q^P - q^R)$ between the minima in two wells.

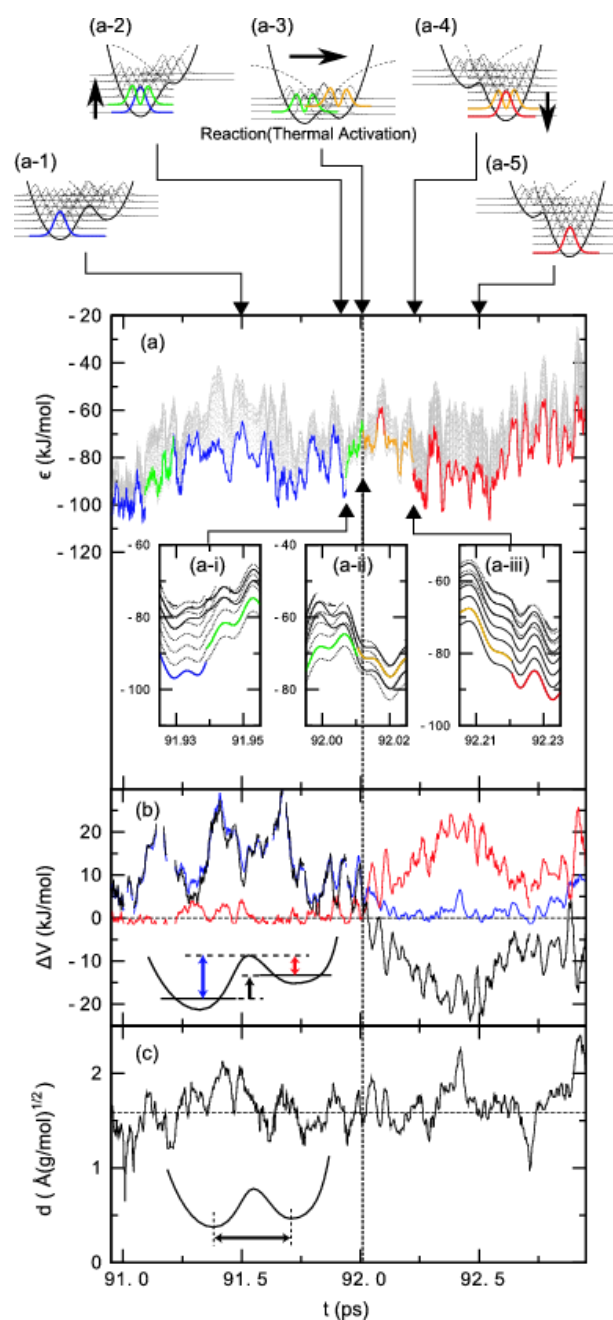


FIG. 5-5. An example of thermal activation reaction found in QCMD. (a) Time evolution of the energy level of the vibrational state. Gray solid and dotted lines indicate the vibrational state in V^R and V^P , respectively. The color represents the occupied vibrational state (blue and green: vibrational ground and excited states in the left well, respectively, and red and orange: vibrational ground and excited states in the right well, respectively). The color changes on the state transition. (b) Barrier

height measured from the ZPEs in V^R and V^P (blue and red lines, respectively), and energy difference $\varepsilon_1^{(P)} - \varepsilon_1^{(R)}$ from the ZPE in the left well to the one in the right well (black line). (c) Distance $d(=q^P - q^R)$ between the minima in two wells.

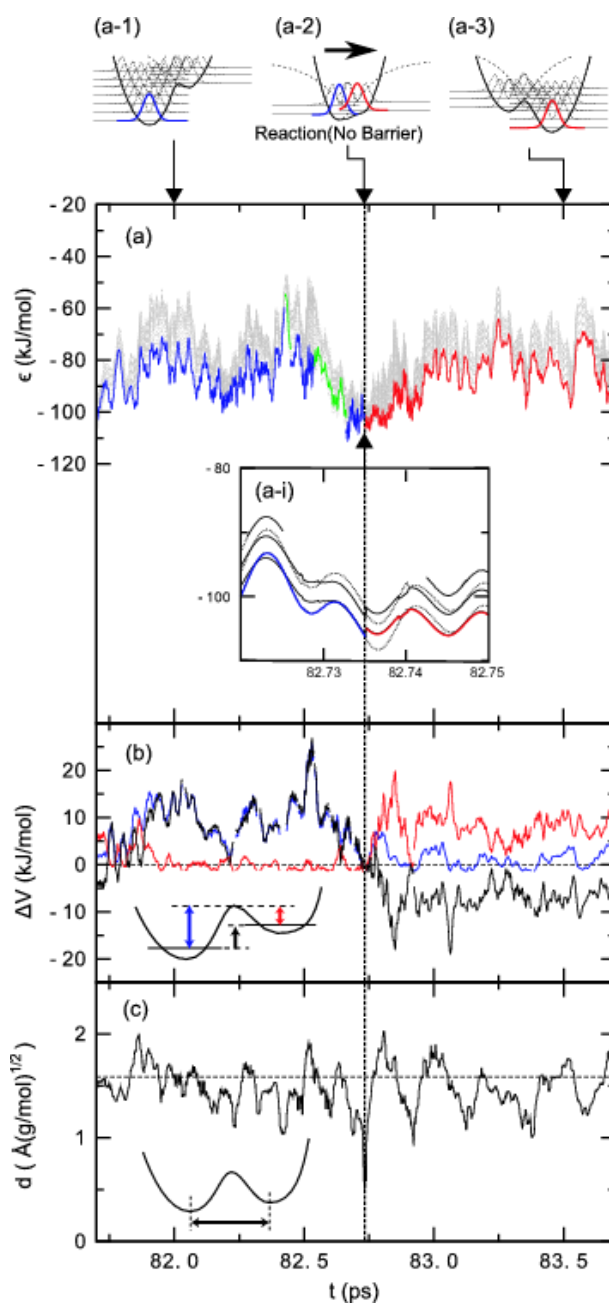


FIG. 5-6. An example of the barrier vanishing reaction found in QCMD. (a) Time evolution of the energy level of the vibrational state. Gray solid and dotted lines indicate the vibrational state in V^R and V^P , respectively. The color represents the occupied vibrational state (blue and green: vibrational ground and excited states in the left well, respectively, and red: vibrational ground state in the right well). The color changes on the transition. (b) Barrier height measured from the ZPEs in V^R and V^P (blue and red lines, respectively), and energy difference $\epsilon_1^{(P)} - \epsilon_1^{(R)}$ from the ZPE in the left

well to the one in the right well (black line). (c) Distance $d(=q^P - q^R)$ between the minima in two wells.

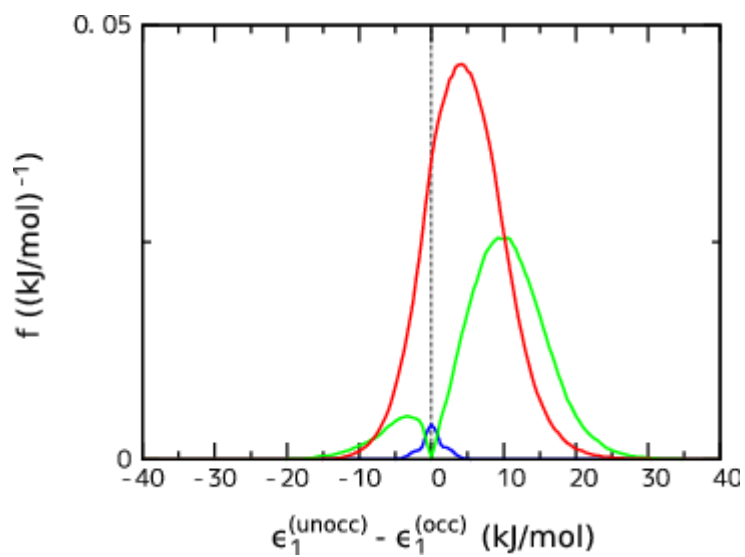


FIG. 5-7. Normalized probability density distributions of the energy difference $\epsilon_1^{(\text{unocc})} - \epsilon_1^{(\text{occ})}$ between ZPEs in two wells of the double-well (red), strongly-asymmetric-single-well (green), and quasi-symmetric-single-well (blue). Here, the energy difference is defined to be positive if the well of the occupied state is more stable than the unoccupied state.

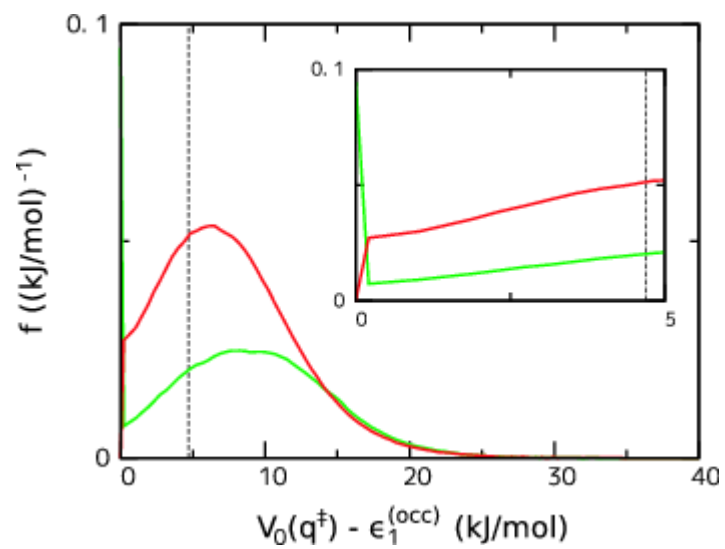


FIG. 5-8. Normalized probability density distributions of the barrier height $V_0(q^\ddagger) - \epsilon_1^{(\text{occ})}$ measured from ZPE in the well of the occupied state for the double-well (red) and strongly-asymmetric-single-well (green).

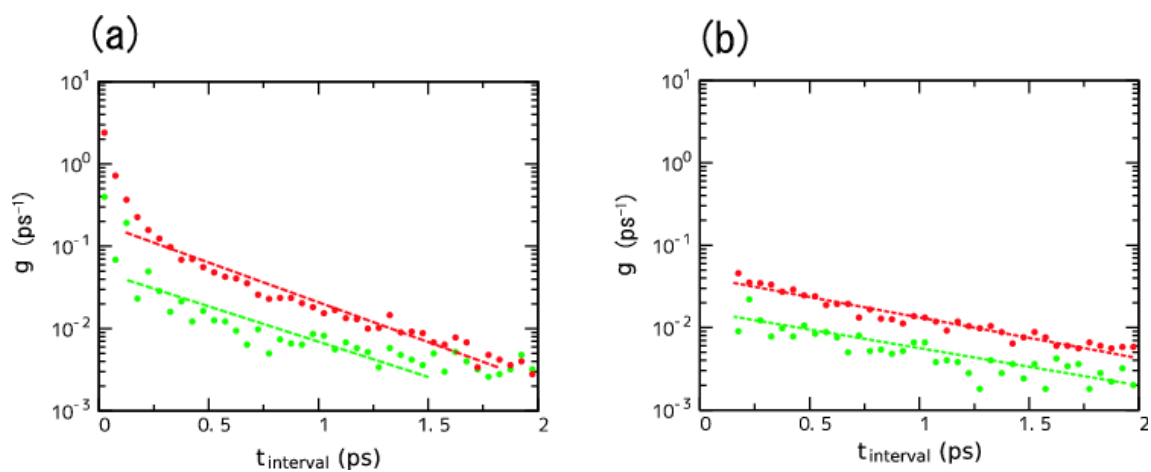


FIG. 5-9. Logarithmic plots of the distribution of the time interval, t_{interval} , between succeeding transfers obtained by QCMD (red) and FCMD (green). (a): the calculated distribution including recrossings and (b): the distribution where shorter time intervals than 150 fs is excluded. Lines are guides for the eye.

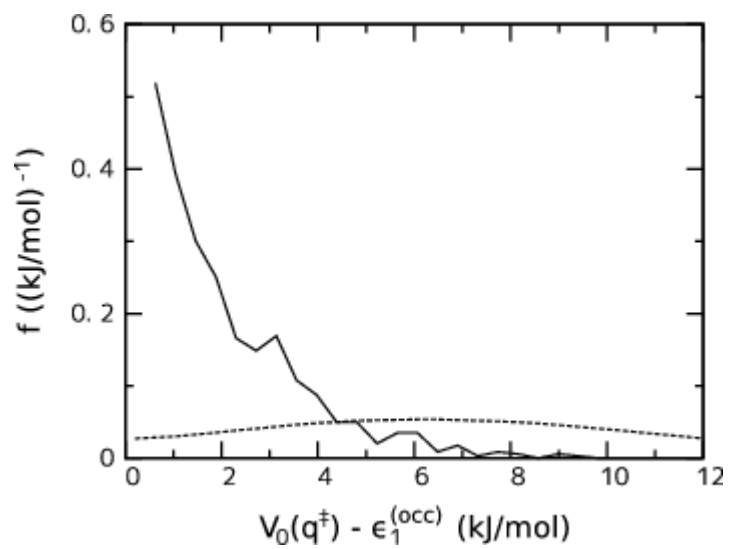


FIG. 5-10. Normalized probability density distributions of the barrier height measured from the ZPE in the reactant well of the tunneling where the tunneling is going to occur (solid line), and distribution of the barrier height measured from the ZPE in the occupied well sampled all over the trajectories in QCMD (dotted line).

VI. INTRAMOLECULAR PROTON TRANSFER REACTION OF MALONALDEHYDE IN NON-POLAR SOLVENT.

A. Introduction

In this chapter, we perform QCMD and FCMD calculations for the proton transfer reaction of malonaldehyde (see Fig. 1-1) in non-polar solvent, neon. By comparing the obtained reaction in neon with that in water in chapter V, the reaction mechanism depending on the solvent is discussed. Further, validity of our calculations is discussed comparing our calculated reaction rates with the theories and experimental data. Molecular mechanisms which cannot be obtained only from the theories and experiments are presented.

B. Molecular dynamics calculations

QCMD and FCMD calculations methods, definitions of state and reaction mechanisms and type of potential energy curve along the reaction coordinate, and analysis of the calculations are described in section B of chapter II. In this section, calculation conditions of the reaction system in neon are described.

To investigate the difference in reaction mechanism caused by the difference in solvent, calculation conditions for QCMD and FCMD for intramolecular proton transfer reaction of malonaldehyde in neon in the present case were set to be the same as those adopted in water. One malonaldehyde molecule and 721 neon molecules were contained in a cubic cell with side length of 28 Å in the periodic boundary condition. The number density of the solvent molecules in the present system was the same as that in water. Lennard-Jones parameters of the OPLS-aa force field [64] were adapted for neon. The intermolecular interactions were cut off at distances greater than 13 Å by using a switching function between 12 and 13 Å. Equations of motion in QCMD and FCMD

were integrated using the Gear method and the RESPA method, respectively. The time step was 0.1 fs for the classical degrees of freedom in QCMD and FCMD and 0.1/200 fs for the quantum degree of freedom in QCMD. Fifty independent equilibrated initial configurations at 298.15 K were prepared for both QCMD and FCMD; then, a 110-ps-long calculation was executed in the NVE ensemble starting from each initial configuration. After an equilibration run for 10 ps, a total of 5.0 ns (= 100 ps × 50) of trajectory was analyzed for each QCMD and FCMD.

C. Results and discussion

1. Reaction trajectories

1-1. FCMD

The thermal activation reaction in neon observed in FCMD is presented. Most of the proton transfer reactions in FCMD for malonaldehyde in neon are thermal activation reactions. Almost no barrier vanishing reactions occurred in neon.

An example of the calculated trajectory for the thermal activation reaction in neon found in FCMD is presented in Fig. 6-1. Figure 6-1(a) shows the time evolution of $q(t)$ over 2 ps. First, the system was found in the right well, the reactant state (Fig. 6-1(a-1)), and then it transferred to the left well, the product state, at $t = 12.85$ ps (vertical dotted line, Fig. 6-1(a-2)) by the thermal activation reaction. After the reaction, $q(t)$ stayed in the left well (Figs 6-1(a-3), (a-4)). At $t = 12.0$ – 12.85 ps, the amplitude and frequency of the fluctuation of $q(t)$ did not change much in the right well. The calculated potential barrier heights measured from the minima of the right (red) and left (blue) wells are presented in Fig. 6-1(b). The barrier heights fluctuate around 6 kJ/mol, which is almost the same as the height in vacuum. The energy difference between the two minima of the wells, drawn in black in Fig. 6-1(b), fluctuated around 0 kJ/mol, which means that stabilization by solvation is small. Figure 6-1(c) shows the time evolution of the distance between the two minima of

the wells. The distance fluctuated around $1.6 \text{ \AA}(\text{g/mol})^{1/2}$, which is almost the same as that found in vacuum (horizontal dotted line). At $t = 12.85 \text{ ps}$, when the reaction occurred, the barrier height from the reactant well was lowered slightly to 5.0 kJ/mol and the distance between the two minima also reduced slightly, that is, to about $1.5 \text{ \AA}(\text{g/mol})^{1/2}$. At $t = 12.85\text{--}13.55 \text{ ps}$ after the reaction, both the barrier height and the distance fluctuated around the values found in vacuum, although the $q(t)$ fluctuations were larger than those before the reaction. The amplitude of $q(t)$ became small at $t = 13.55 \text{ ps}$ (Fig. 6-1(a-4)). At the same time, the barrier height from the left well became larger, ranging from about 3 to 8 kJ/mol , and the distance became as short as $1.4 \text{ \AA}(\text{g/mol})^{1/2}$. This clearly indicates that the excess energy obtained by the reaction was transferred from the solute to the solvent by the solute–solvent interactions.

1-2. QCMD

Trajectories of the tunneling and thermal activation reactions observed in the QCMD calculations are presented and are compared with those in water.

1-2-1. Tunneling reaction

A trajectory of a tunneling reaction in neon found in a QCMD calculation is presented in Fig. 6-2. Figure 6-2(a) shows the time evolution of the vibrational energy levels in the right (solid gray line) and left (dotted gray line) wells, and the currently occupied vibrational energy level in the surface-hopping calculations is colored red for the right well and blue for the left well. As shown in the figure, the vibrational ground state in the right well was occupied at $t = 81.6\text{--}82.88 \text{ ps}$ (red lines in Figs 6-2(a), (a-1)). At $t = 82.88 \text{ ps}$, a transition of the system to the vibrational ground state in the left well occurred by a tunneling mechanism (Figs 6-2(a-2), (a-i)). The solute then released the excess energy of 0.3 kJ/mol to the solvent. After the reaction, the system stayed in the

left well without transitions (blue lines in Figs 6-2(a), (a-3)). Figure 6-2(b) shows the barrier heights from the ZPEs and the energy difference between the ZPEs of the two wells. Before the reaction, the energy difference between the ZPEs was almost 0 kJ/mol, indicating that the reaction potential energy curve was of the almost symmetric double-well potential type without stabilization of the occupied well by solvation. As discussed earlier, this is caused by the weak solute–solvent interactions in neon. Then, the vibrational levels in the two wells were close to each other, indicating that the condition of energy conservation is satisfied constantly. At $t = 82.88$ ps, the barrier heights from the two wells were lowered simultaneously to almost 2.5 kJ/mol from about 4.5 kJ/mol. The tunneling reaction then occurred. Figure 6-2(c) shows the time evolution of the distance between the minima of the two wells. The distance fluctuated around an average value similar to that found in vacuum, $1.6 \text{ \AA}(\text{g/mol})^{1/2}$ (horizontal dotted line). However, when the reaction occurred, the distance became significantly shorter, $1.3 \text{ \AA}(\text{g/mol})^{1/2}$. Thus, the overlap of the wave functions of the vibrational states in the two wells was great. Then, the transition probability increased and the tunneling reaction occurred. The distance shortened again at $t = 83.2$ ps. However, the transition probability is still small because of the difference in vibrational energy levels between the two wells. In this case, no reaction occurred.

1-2-2. Thermal activation reaction

A trajectory of a thermal activation reaction in neon observed in the QCMD calculations is presented in Fig. 6-3 in the same way as in Fig. 6-2. In Fig. 6-3(a), the blue and green lines represent the energy levels of the currently occupied vibrational state in the left well, and the red and orange lines represent those in the right well. The quantum system of interest is found in the vibrational ground state in the left well at $t = 36.600\text{--}37.785$ ps (blue line, Fig. 6-3(a-1)). At $t = 37.785$ ps, vibrational excitation from the ground state to the first excited state was observed (green

line, Figs 6-3(a-2), (a-i)). Then, the system absorbed energy of 3.3 kJ/mol from the solvent to conserve energy. In this case, the first excited state may be considered to be the transient state, that is, the energy level of the first excited state is higher than that of the barrier. At $t = 37.795$ ps, 0.01 ps after the excitation, the system transferred to the first excited state in the right well (orange line) above the barrier (Figs 6-3(a-3), (a-i)). The system stayed in the first excited state in the right well for 0.4 ps, and, then, the vibrational relaxation to the ground state occurred at $t = 38.19$ ps (red line, Figs 6-3(a-4), (a-ii)), where the solute released energy of 3.2 kJ/mol to the solvent. After the relaxation, the solute stayed in the ground state in the right well (Fig. 6-3(a-5)). This is the thermal activation reaction. Transitions from the left well to the right well above the barrier may occur easily because of the high overlap of the wave functions between the two wells.

1-2-3. Comparison with the fluctuations in water

The trajectories of the quantum system in neon shown in Figs 6-1, 6-2, and 6-3 can be compared with the trajectories in water (Figs 5-2(a), (b), and (c) in chapter V). From the figures, we can easily find that the fluctuation of the potential for the present system in neon is very small because the solute–solvent interactions are weak. In contrast, the fluctuation is large in water. Further, reorganization of the hydration structure and the resultant stabilization of the occupied well by the hydration are clearly found in water. This is because the solute–solvent interactions are strong. The solvation effect is small in neon, as discussed above. Furthermore, the rate of fluctuation is slow in the present case compared with that found in water. This is because the mass of neon is much greater than that of hydrogen in water. The reaction trajectories found in neon and in water are, thus, very different.

2. The reaction potential energy curve in neon

The reaction potential energy curve in solution, $V_0(q)$, is essential for the reaction because the time variation of $V_0(q, t)$ causes transitions of the system and leads the system to the reaction. In this subsection, V_0 in neon found in QCMD calculations is analyzed statistically. It is then compared with that in water reported previously in chapter V to investigate the characteristics of the reaction mechanisms in the different solvents.

2-1. Shape

The shape of the reaction potential curve in solution, V_0 , may be classified into double-well, strongly-asymmetric-single-well, and quasi-symmetric-single-well. The calculated distribution of the shape is presented in Table 6-1 for malonaldehyde in neon and water, as observed in QCMD calculations. In neon, the proportion of the double-well was 99.8%, while it was 0.2% for the strongly-asymmetric-single-well and almost 0% for the quasi-symmetric-single-well. Summation of the ratios for the latter two was less than 1%, showing that these shapes are scarcely found in neon. In contrast, in water, the proportions for the three were 61.2%, 37.5%, and 1.3%, respectively. The sum of the proportions of the latter two was as great as 36.8%. As discussed above, the difference in the distribution comes from the difference in the solute–solvent interactions.

2-2. Barrier height and ZPE difference

The difference between the two ZPEs of the double well, $\Delta\epsilon_1$, is defined by subtracting the ZPE in the occupied well $\epsilon_1^{(\text{occ})}$ from the ZPE in the unoccupied well $\epsilon_1^{(\text{unocc})}$, i.e., $\Delta\epsilon_1 = \epsilon_1^{(\text{unocc})} - \epsilon_1^{(\text{occ})}$. The calculated distributions of the energy difference for the solute in neon and water are shown in Fig. 6-4. The distribution of $\Delta\epsilon$ for the double well in neon (red solid line) has a peak at 0 kJ/mol and is symmetric with respect to the peak. It ranges from -2.5 kJ/mol to 2.5 kJ/mol.

Since $\Delta\epsilon_1$ is 0 kJ/mol in vacuum, the observation implies that the occupied well is not much stabilized by solvation and the fluctuation is as small as $k_B T$ (~ 2.5 kJ/mol).

The calculated distribution in water is different from that in neon. As shown in Fig. 6-4, the distribution of $\Delta\epsilon_1$ for the double well in water (blue broken line) has a peak at 4.1 kJ/mol. This means that the shape of V_0 in water is asymmetric because of the stabilization of the occupied well by hydration. Further, more than 99% of the double-wells show $\Delta\epsilon_1$ ranging from -12 kJ/mol to 25 kJ/mol. The distribution at the negative $\Delta\epsilon_1$ indicates that even destabilization of an occupied well by hydration sometimes occurs within thermal fluctuations. The width of the distribution in water is more than 37 kJ/mol. This is significantly larger than that in neon, 5 kJ/mol.

Figure 6-5 shows the calculated distribution of the barrier height from the ZPE in the occupied well, $\Delta V_b = V_0(q^\ddagger) - \epsilon_1^{(\text{occ})}$, in neon (red solid line) and water (blue broken line), where q^\ddagger is the q coordinate at the barrier. The distribution in neon has a peak at 4.4 kJ/mol for the double-well, which is slightly lower than the value in vacuum, 4.7 kJ/mol (black broken line). This implies that the system in the occupied well is not much stabilized by solvation.

In water, the distribution has a peak at 6.5 kJ/mol for the double-well. Unlike in neon, the occupied well in water is stabilized by hydration, and, on average, the barrier from the reactant well is higher than that from the product well. Further, the wide distribution from 0 kJ/mol to 20 kJ/mol represents strong fluctuations that produce both occupied deep well by stabilization and occupied shallow well by destabilization.

Information obtained by the statistical analysis for the proton transfer reaction potential curve in neon and water is summarized schematically in Figs 6-6(a) and (b), respectively. The potential curve in neon is almost symmetric and has small fluctuations (Fig. 6-6(a)). In contrast, in water, it is asymmetric and the occupied well is, on average, stabilized by hydration and the fluctuation is so strong that even destabilizations by hydration are sometimes found. These must influence the proton

transfer reaction in solution significantly, both the reaction rate and the mechanism.

3. Reaction rate

3-1. Definition of reaction

Reaction rates were evaluated from the trajectories. Figure 6-7(a) shows the logarithmic plots of the number of reactions as a function of the time interval, t_{interval} , between successive reactions in neon observed in QCMD (red points) and FCMD (green points) calculations. When the successive reactions are independent of each other, an exponential distribution should be found, i.e., the Poisson distribution. In this case, the logarithmic plot should give a straight line. As discussed in detail in our previous paper, the plot for the proton transfer reaction in water gives a straight line for long t_{interval} , but not for short t_{interval} . This implies that short-time recrossings occurred frequently. Since the plots deviated from straight lines at about $t_{\text{interval}} = 150$ fs, we excluded the reactions having t_{interval} shorter than 150 fs. Then, straight lines were obtained for all values of t_{interval} . In the present analysis for the reaction in neon, the same threshold of 150 fs was adopted as for the reaction in water. Neglect of the recrossings with periods shorter than 150 fs gives rise to an increase in period of the reactions longer than 150 fs, although the number of reactions does not change. The resultant distribution of t_{interval} is presented in Fig. 6-7(b) for the reactions observed in QCMD and FCMD calculations in neon. The plots show straight lines for the whole range of t_{interval} , indicating that the reactions analyzed here are all independent of each other. It must be noted here that the calculated value of the reaction rate depends on the threshold according to the present analysis, including some arbitrariness. However, we believe that the analysis can provide valuable information about the proton transfer reaction in solution, at least qualitatively.

3-2. Reaction rate

Table 6-2 shows the number of reactions, the average time interval between reactions, and the reaction rate obtained from QCMD and FCMD calculations over 5 ns in neon in the present calculations and in water. Values in vacuum are also shown in the table. The values of water and vacuum are cited from chapter V. Here, the average time interval was defined as the number of reactions divided by the whole simulation time. The reaction rate is given by the inverse of the average time interval. The reaction rates in neon were 0.15 ps^{-1} and 0.89 ps^{-1} for FCMD and QCMD, respectively. The corresponding rates in water were 0.36 ps^{-1} and 0.70 ps^{-1} . In both solvents, the rates observed in QCMD calculations are greater than those in FCMD calculations. In particular, in neon, the rate in the former calculations was about 6 times larger than that found in the latter. This demonstrates that the quantum effect is important in the reaction. In FCMD, the rate in neon was smaller than that in water, whereas in QCMD, the rate in neon was greater than that in water. Further, the rate in QCMD in both solvents was greater than that in vacuum, 0.27 ps^{-1} . We compare these reactions in detail in terms of polarity of the solvent, and then compare them with the reaction rate theories and the experiments.

The calculated reaction rate from FCMD trajectories may be compared with that from classical transition-state theory. According to the theory, the reaction rate k may be written [5]:

$$\ln(k) \approx \frac{\beta}{4\pi\epsilon_0} \left(\frac{\epsilon_s - 1}{2\epsilon_s + 1} \right) \left(\frac{\mu_{\ddagger}^2}{r_{\ddagger}^3} - \frac{\mu_A^2}{r_A^3} \right) + \alpha', \quad (6-1)$$

where $\beta = 1/k_B T$, ϵ_0 is the dielectric constant of vacuum, ϵ_s is the relative dielectric constant of solvent, r_A and r_{\ddagger} are the radiuses of the solute at the reactant state and the transition state, respectively, and μ_A and μ_{\ddagger} are the dipole moments of the solute in the reactant state and the transition state, respectively. α' is a constant depending on the solute. The value of r_A was taken as 3.0 \AA and r_{\ddagger} was assumed to be the same as r_A . The dipole moments, $\mu_A = 11.0 \times 10^{-30} \text{ C} \cdot \text{m}$ and $\mu_{\ddagger} = 11.6 \times 10^{-30} \text{ C} \cdot \text{m}$, give $\mu_{\ddagger}^2 - \mu_A^2 > 0$. ϵ_s of neon and water, 1.33336 (at 20 K) and

80.100 (293.2 K) [67], respectively, give the value of the first term of the right-hand side of Eq. (6-1) to be 0.54 for water and 0.10 for neon. The reaction rate is higher in water than in neon because water gives greater stabilization of the transition state than neon does. This stabilization reduces the energy barrier and results in the larger reaction rate for the former than for the latter. The reaction is promoted by the solute–solvent interactions. The calculated reaction rate from FCMD is qualitatively in good agreement with this theoretical prediction.

Next, we compare the reaction rate from QCMD trajectories with that from the Marcus theory, the reaction rate theory based on quantum mechanics. Since the free energy difference between reactant and product state is almost zero because the structures of the solute in the two states are the same and, further, in our model, the solvent molecule does not change its dipole moment by the reaction of the solute molecule, the quantum reaction rate given by the Marcus theory may be written as [6]

$$k \propto \sqrt{\frac{1}{E_r}} \exp\left[-\beta \frac{E_r}{4}\right], \quad (6-2)$$

$$E_r = \alpha \left(1 - \frac{1}{\epsilon_s}\right), \quad (6-3)$$

where α is a solute-dependent parameter. The equations show that the reaction rate decreases with increasing ϵ_s . According to the Marcus theory, the reaction rate in neon should be greater than that in water. This is qualitatively in good agreement with the present result. Thus, our calculations are consistent with the reaction rate theories.

The calculated reaction rates obtained from FCMD and QCMD calculations may also be compared with experiments. The experimental reaction rate for the photoexcited proton transfer reaction from N,N-dimethylaniline to 2-chlorobenzophenone in eight solvents [45] is plotted in Fig. 6-8(a) as a function of the solvent dielectric constant ϵ_s . The calculated reaction rates for the present malonaldehyde in neon and water are also plotted in Fig. 6-8(b). The figure clearly shows that the

reaction rate decreases with increasing solvent dielectric constant both for the present QCMD calculations and in the experiments. These observations are in good agreement with the Marcus theory.

We plotted the experimental reaction rate as a function of the heat capacity, which might be related to the energy fluctuation of the solvent. However, no correlation was found between the heat capacity and the reaction rate.

However, the ϵ_s dependence obtained from FCMD calculations is opposite to those described above. This implies that the quantum effect of the proton on the proton transfer reaction rate is large, and its neglect leads to a wrong result. Thus, the present QCMD calculations are consistent with the experiments as well as the Marcus theory.

4. Reaction mechanism

The reaction rate may be measured experimentally. However, it is very difficult to investigate the reaction mechanism only by experiments. In this subsection, the proton transfer reaction mechanism for malonaldehyde in neon is analyzed in detail based on the present calculations. Further, the mechanism is compared with that found in water. The quantum effect is also discussed by comparing the QCMD calculations with the FCMD calculations. Table 6-2 shows the number of tunneling, thermal activation, and barrier vanishing reactions found in the QCMD and FCMD calculations for the two solvents. The proportions are also presented for each mechanism in parentheses.

4-1. Tunneling reaction

As shown in Table 6-2, the tunneling reaction makes the largest contribution among the mechanisms, 63.4%, to the reaction rate in neon. This means that the quantum effect is very

important. The proportion of the tunneling reaction is also great in water, 33.3%. The numbers of tunneling reactions in neon and water were 2811 and 1168, respectively, in the present calculations. The former is two and a half times greater than the latter. This implies that the mechanism depends on the solvent. We discuss this tunneling mechanism based on the analysis of the shape of V_0 and its fluctuations.

Figure 6-9(a) shows the calculated distribution of the energy difference between the ZPEs, $\Delta\epsilon_1 = \epsilon_1^{(\text{unocc})} - \epsilon_1^{(\text{occ})}$, defined by subtracting the ZPE in the occupied well from that in the unoccupied well in the QCMD calculations. The red circles represent the distribution of $\Delta\epsilon_1$, which was measured when the tunneling reaction occurred in neon. The distribution has a sharp peak at 0 kJ/mol, indicating that the tunneling reaction occurs most often when V_0 is of symmetrical shape. This is because the transition probability between the two states is high only when the energy level of the two states is the same or very similar, i.e., the energy conservation law.

The blue triangles in Fig. 6-9(a) show the distribution of the energy difference $\Delta\epsilon_1$ between the ZPEs in water defined in the same way as that in neon. A similar peak is found at 0 kJ/mol in water. However, the peak is broad. As shown earlier in Fig. 6-4, the distribution of $\Delta\epsilon_1$ averaged over all trajectories in water has a peak at 4.1 kJ/mol. Thus, the proton transfer reaction occurred only when the energy conservation law was satisfied, although this condition was rarely satisfied in water. This may be caused by the stabilization of the occupied well by hydration. Since it is difficult for the solvent water to absorb a large energy gap between the reactant and product states, the tunneling reaction hardly occurred in water. This is quite different from the reaction in neon.

Figure 6-9(b) shows the calculated distribution of the barrier height from the ZPE in the occupied well, $\Delta V_b = V_0(q^\ddagger) - \epsilon_1^{(\text{occ})}$, which was measured when the tunneling reaction occurred. For neon, the distribution has a clear peak. It is asymmetric with respect to the maximum. It decreases very rapidly for larger $\Delta V_b = V_0(q^\ddagger) - \epsilon_1^{(\text{occ})}$, the right-hand side of the distribution. This

is because the overlap of the wave function between the reactant and product states is larger when the barrier is low, so that the transition occurs easily.

In contrast, the barrier height in water is distributed over a lower region than that in neon. However, this condition could not be satisfied so often considering the very broad distribution located in the higher barrier region presented in Fig. 6-5 averaged over all trajectories. The low barrier makes it easy for the tunneling reaction to occur. However, the large $\Delta\epsilon_1$ for the solute in water presented in Fig. 6-9(a) significantly lowers the transition probability. The difference in the shape of V_0 is caused by the difference in the solute–solvent interaction.

Table 6-2 also shows the reaction rate in vacuum at 298.15 K estimated for a one-dimensional model of malonaldehyde (see chapter V for details). The reaction occurred 1350 times during the calculations. The reactions observed are all tunneling reactions. The tunneling reaction in neon occurred 2.4 times more frequently than that in vacuum, while that in water occurred only 0.87 times as frequently. As shown above, the condition for the tunneling reaction is the close energy level between the reactant and product states, as well as the low barrier. In neon, the vibrational energy level of the reactant and product states is always close, as it is in vacuum. Further, the lower barriers are found frequently. Thus, the tunneling reaction occurs more frequently than in vacuum. In contrast, in water, the barrier is high from the reactant state by hydration and, further, the energy level is different between the reactant and the product wells. The tunneling reaction thus occurs less frequently than in vacuum.

4-2. Thermal activation reaction and barrier vanishing reaction

In this subsection, the thermal activation reaction and the barrier vanishing reaction are discussed. In neon, the numbers of thermal activation and barrier vanishing reactions in QCMD and in FCMD were 1622 and 768, respectively. The ratio is 2.1:1. The quantum effect is clearly caused

by the lowering of the barrier height by ZPE. According to the transition-state theory, the ratio of the rates with and without the ZPE effect is 1.9:1, where the ZPE was assumed to be about 1.55 kJ/mol. This value is in good agreement with that obtained from our QCMD and FCMD calculations. Thus, the difference between QCMD and FCMD can be explained by the ZPE effect. As shown in chapter V, the ratio in water can also be explained by the ZPE effect, although the value is a little different, 1.3:1. Comparing the two solvents, there are more thermal activation reactions and barrier vanishing reactions in water than in neon in both the FCMD and QCMD calculations. However, the order of the numbers of these reactions in the two solvents does not change because of the quantum effect. Thus, solute–solvent interaction is the dominant factor that determines the reaction rates. The barrier vanishing reaction seldom occurs in neon in either the FCMD or QCMD calculations because the obtained V_0 is almost of double-well shape, as shown in Table 6-1.

The shape of the potential energy curve was measured when the thermal activation reactions occurred in neon. Figure 6-10 presents the calculated distribution of the energy difference $\Delta\epsilon_1 = \epsilon_1^{(\text{unocc})} - \epsilon_1^{(\text{occ})}$ between the ZPEs and the barrier height $\Delta V_b = V_0(q^\ddagger) - \epsilon_1^{(\text{occ})}$ from the ZPE of the occupied state. The distributions found in Fig. 6-10 for neon and water are similar to those found in Fig. 6-9. This implies that the thermal activation reactions can occur when the solute is in similar circumstances to those for the tunneling reactions.

4-3. Hydration structure

We showed that stabilization of the occupied well was not found when the tunneling reaction occurs. This should be related to the hydration structure around the malonaldehyde molecule.

Number densities of the oxygen atom of water is presented in Fig. 6-11 as a function of the radial distance between the oxygen atom and the proton of malonaldehyde. Position of the proton was chosen to be the most stable position in vacuum. The density calculated from all trajectories

from the reactant position (red broken line) has a peak at 3.5 Å. However, it is not found in the density profile from the product position (blue broken line). This clearly shows that the occupied state is solvated.

For the solvation structure where the reaction is going to occur, the calculated radial number densities are shown in Fig. 6-11. The density from the reactant position (red solid line) does not have a peak at 3.5 Å where a peak is found in the density calculated for all trajectory. The density profile is similar to the one from the product position (blue solid line). This shows that the solvation structure of the reactant proton and the product proton is similar to each other when the reaction occurs.

D. Conclusions

In this study, the microscopic behavior of the intramolecular proton transfer reaction of malonaldehyde in neon has been investigated using QCMD and FCMD calculations. The results were compared with those in water. The differences in the reaction mechanism in the different solvents have been investigated from the statistical analyses of the reaction trajectories. The calculated reaction rate in water in FCMD calculations was greater than that in neon. In contrast, the reaction rate in neon was greater than that in water in QCMD calculations. The quantum effect is, thus, essential for the proton transfer reaction in solution.

The calculated reaction rate from FCMD is qualitatively in good agreement with that from the classical transition-state theory, and that from QCMD is in good correspondence with that from the Marcus theory, as well as that from experiments.

The opposite trend found between FCMD and QCMD calculations is caused by the more frequent tunneling reactions in neon than in water. This can be explained by the shape of the potential energy curve along the reaction coordinate and its fluctuations. They are significantly different between the two solvents because of the different interactions with the solute. The

tunneling reaction in water is relatively more difficult compared with that in neon because the vibrational energy level is different between the reactant and product states. This is clearly caused by stabilization of the reactant well by solvation. The reaction in water occurs when the reactant well is destabilized by large thermal fluctuations and the energy levels of the reactant and product states approach each other. No such solvation effect was found in neon. There, the reaction occurs more frequently because the reaction potential curve is nearly symmetric and the difference in energy levels between the two states is very small. The situation is similar to that in vacuum. The thermal activation reaction and the barrier vanishing reaction are accelerated by the ZPE. The reaction rate based on these mechanisms is greater in water than in neon in both the FCMD and QCMD calculations. This trend is caused by the strong interaction of the solute with solvent water.

TABLE 6-1. The calculated proportions of potential wells found in the trajectories of QCMD. The values of water are cited from chapter V. The statistical error represents the 90% confidence interval.

Potential well	Proportion (%)	
	Neon	Water
Double-well	99.8 ± 0.1	61 ± 1
Strongly-asymmetric-single-well	0.2 ± 0.1	38 ± 1
Quasi-symmetric-single-well	~ 0.0	1.3 ± 0.1

TABLE 6-2. Number of total reactions in 5-ns-long trajectories, average time interval between reactions, reaction rates, number of reactions by tunneling, number of reactions by thermal activation, and number of reactions by barrier vanishing mechanisms in neon, water, and vacuum. The values of water and vacuum are cited from chapter V. The statistical error represents the 90% confidence interval.

	Neon		Water		Vacuum
	QCMD	FCMD	QCMD	FCMD	
Total number of reactions	4433	768	3511	1790	1350
Average interval (ps)	1.1 ± 0.1	6.5 ± 0.5	1.4 ± 0.1	2.8 ± 0.1	3.72
Reaction rate (ps^{-1})	0.89 ± 0.02	0.15 ± 0.01	0.70 ± 0.02	0.36 ± 0.02	0.27
Tunneling reactions	2811 ($63 \pm 3\%$)	...	1168 ($33 \pm 2\%$)	...	1350 (100%)
Thermal activation reactions	1616 ($36 \pm 2\%$)	763 ($99 \pm 12\%$)	1625 ($46 \pm 3\%$)	1399 ($78 \pm 3\%$)	...
Barrier vanishing reactions	6 ($0.1 \pm 0.1\%$)	5 ($0.7 \pm 0.5\%$)	718 ($21 \pm 1\%$)	391 ($22 \pm 1\%$)	...

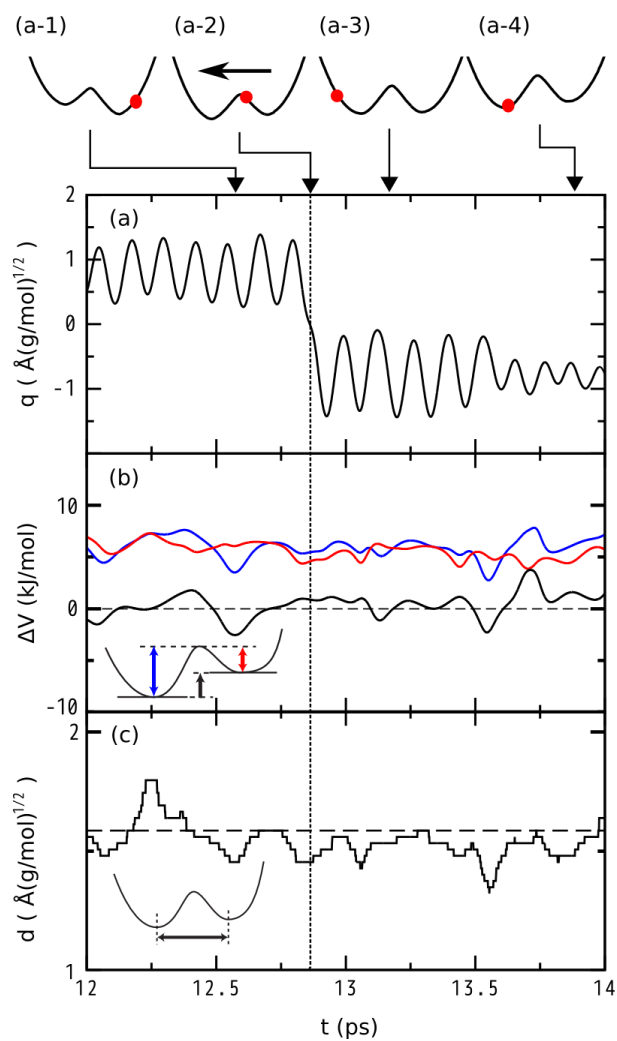


FIG. 6-1. An example of a thermal activation reaction in neon observed in FCMD. (a) $q(t)$. (b) The barrier heights measured from the minimum in the left well (blue line) and that in the right well (red line), and the energy difference between the minima of the two wells (black line). The horizontal black broken line indicates 0 kJ/mol. (c) The distance between the minima of the two wells. The horizontal black broken line indicates the distance in vacuum, $1.6 \text{ \AA}(\text{g/mol})^{1/2}$. The vertical black dotted line represents the time when the thermal activation reaction occurred.

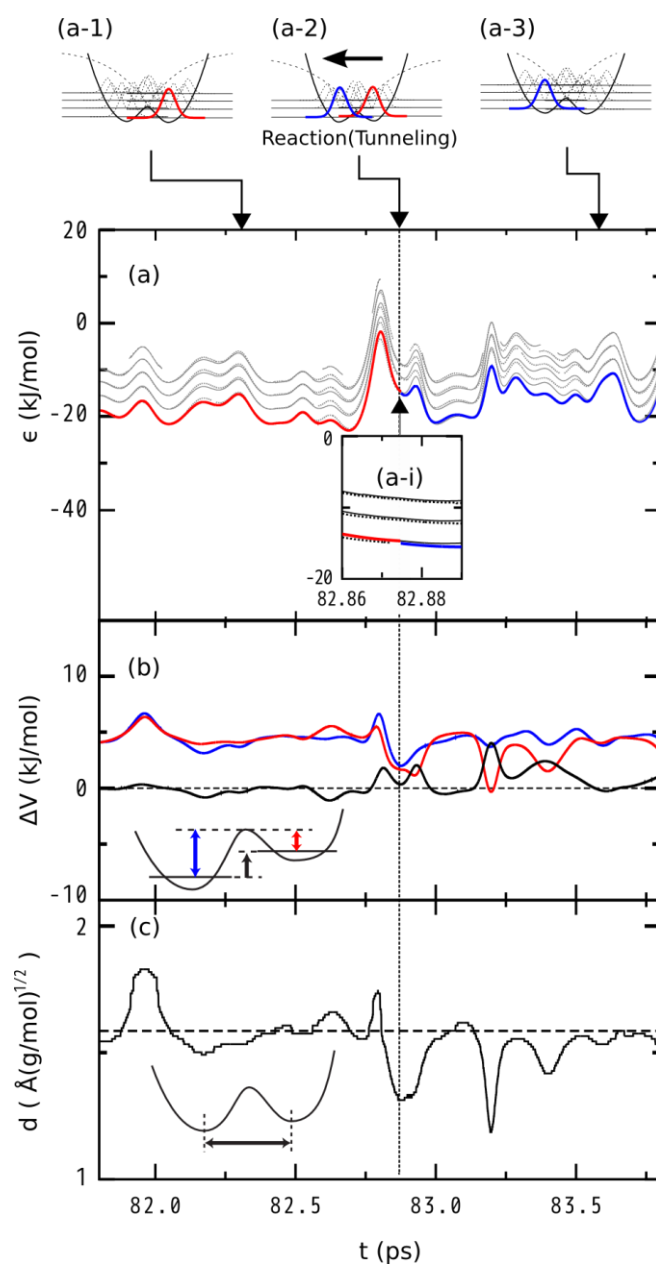


FIG. 6-2. An example of tunneling reaction in neon observed in QCMD. (a) Time evolution of the energy level of the vibrational state. Gray solid and dotted lines indicate the vibrational state in V^R and V^P , respectively. The color represents the occupied vibrational state (blue: vibrational ground state in the left well and red: vibrational ground state in the right well). The color changes on the transition. (b) Barrier heights from the ZPEs in V^R and in V^P (blue and red lines, respectively), and energy difference, $\epsilon_1^{(P)} - \epsilon_1^{(R)}$, between ZPEs in the left well and the one in the right well (black line). (c) Distance, $d (= q^P - q^R)$, between the minima of the two wells.

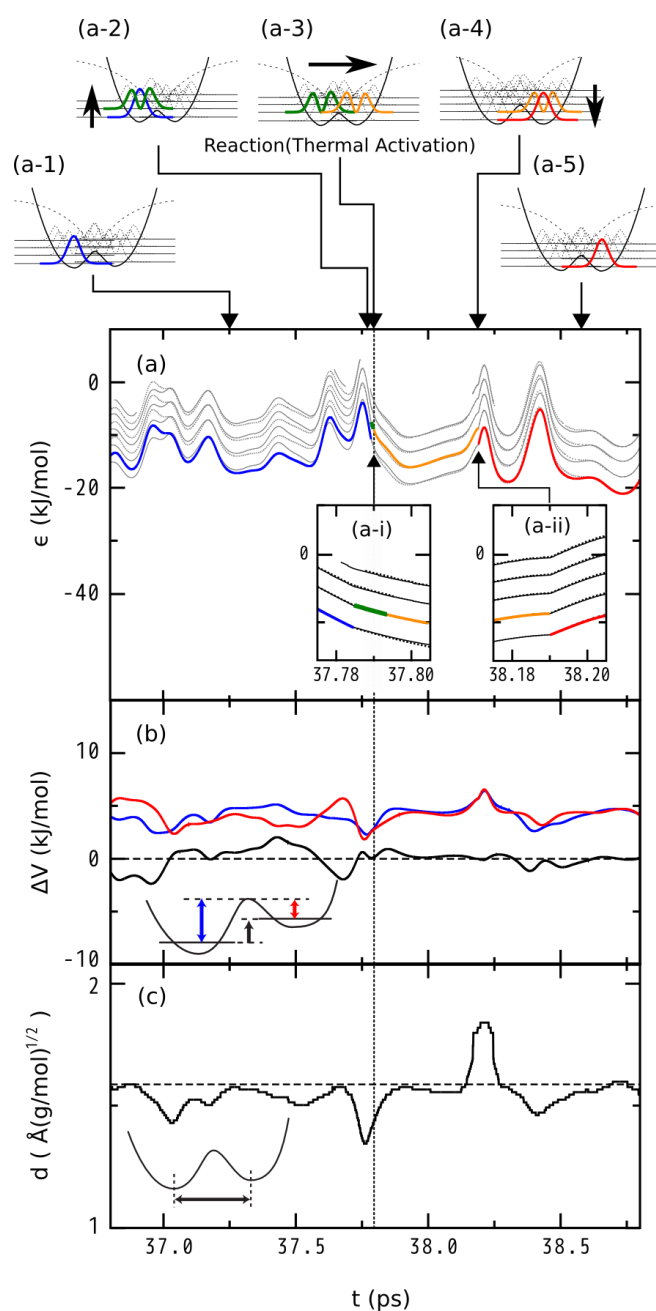


FIG. 6-3. An example of thermal activation reaction in neon observed in QCMD. (a) Time evolution of the energy level of the vibrational state. Gray solid and dotted lines indicate the vibrational state in V^R and V^P , respectively. The color represents the occupied vibrational state (blue and green: vibrational ground and excited states in the left well, respectively, and red and orange: vibrational ground and excited states in the right well, respectively). (b) Barrier heights from the ZPEs in V^R and in V^P (blue and red lines, respectively), and energy difference, $\epsilon_1^{(P)} - \epsilon_1^{(R)}$, between ZPEs in

the left well and the one in the right well (black line). (c) Distance $d (= q^P - q^R)$ between the minima of the two wells.

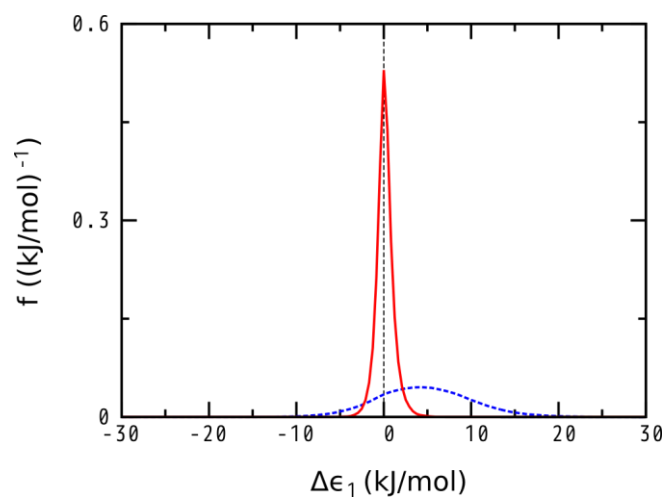


FIG. 6-4. Normalized probability density distribution of the energy difference $\Delta\epsilon_1 = \epsilon^{(\text{unocc})} - \epsilon^{(\text{occ})}$ between ZPEs in the two wells for V_0 of double-well shape in neon (red solid line) and in water (blue broken line). Vertical black broken line indicates 0 kJ/mol, which is the value in vacuum.

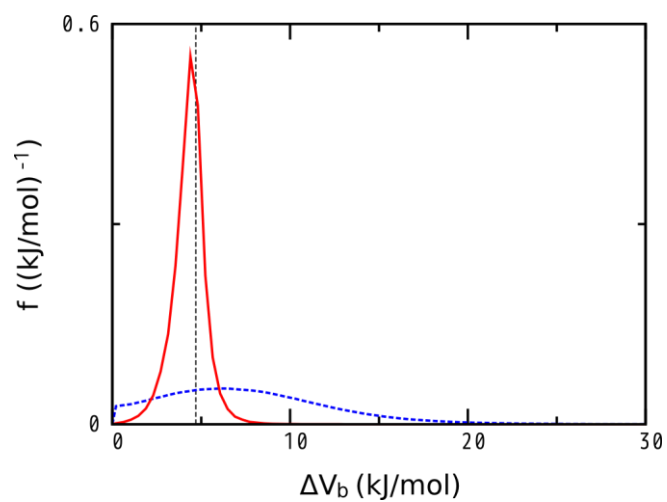


FIG. 6-5. Normalized probability density distributions of the barrier height, $\Delta V_b = V_0(q^\ddagger) - \epsilon_1^{(\text{occ})}$, measured from ZPE in the well of the occupied state for V_0 of double-well shape in neon (red solid line) and in water (blue broken line). Vertical black broken line indicates 4.7 kJ/mol, which is the value in vacuum.

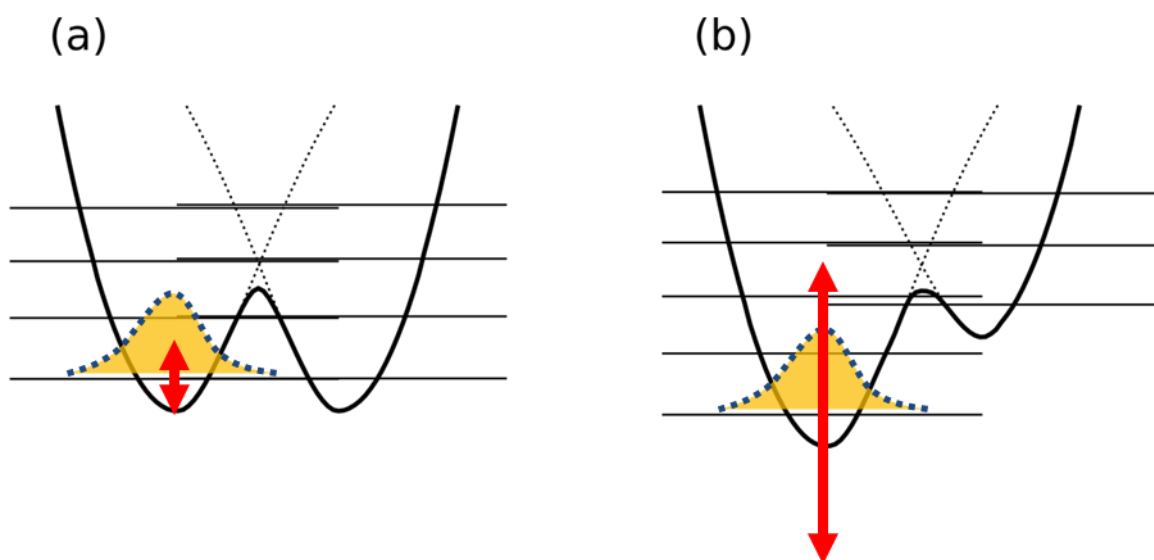


FIG. 6-6. Schematic pictures of the reaction potential energy curve V_0 in (a) neon and (b) water when the current state is in the left well. The vertical red arrows represent the fluctuations of the reactant well.

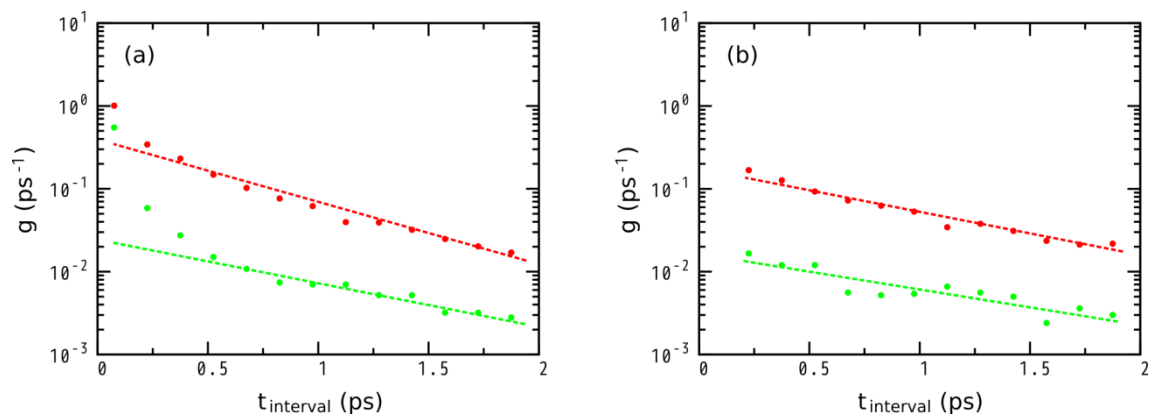


FIG. 6-7. Logarithmic plots of the distribution of the time interval, t_{interval} , between successive transfers obtained by QCMD (red) and FCMD (green). (a) The calculated distribution including recrossings and (b) the distribution when shorter time intervals than 150 fs are excluded. Lines are visual guides.

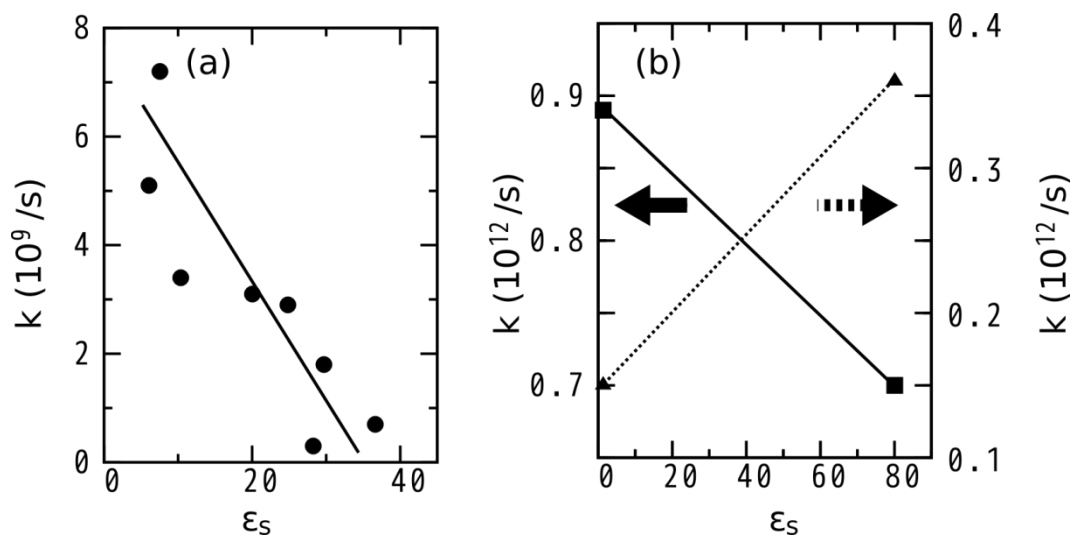


FIG. 6-8. (a) Experimental reaction rate k (circle) as a function of relative dielectric constant ϵ_s of the solvent for 2-chlorobenzophenone [45]. The solvents used in the experiment are tetrahydrofuran ($\epsilon_s = 7.56$), ethyl acetate ($\epsilon_s = 6.0814$), 1,2-dichloroethane ($\epsilon_s = 10.36$), pentanenitrile ($\epsilon_s = 20.04$), butanenitrile ($\epsilon_s = 24.83$), N,N-dimethylformamide ($\epsilon_s = 28.25$), propanenitrile ($\epsilon_s = 29.7$), and acetonitrile ($\epsilon_s = 36.63$). The values of ϵ_s are from Ref. [67]. (b) The calculated reaction rate in the present QCMD (square) and FCMD (triangle). Lines are visual guides.

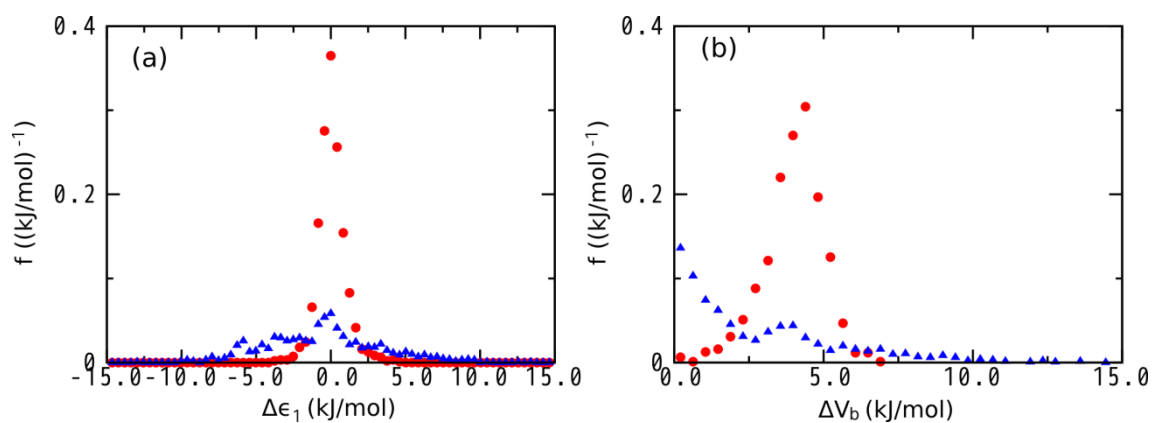


FIG. 6-9. Normalized probability density distributions of (a) the energy difference, $\Delta\epsilon_1 = \epsilon_1^{(\text{unocc})} - \epsilon_1^{(\text{occ})}$, between the ZPEs in two wells and (b) the barrier height, $\Delta V_b = V_0(q^\ddagger) - \epsilon_1^{(\text{occ})}$, from ZPE in the well of the occupied state in the double well, which were measured when the tunneling reaction occurred in neon (red circle) and in water (blue triangle).

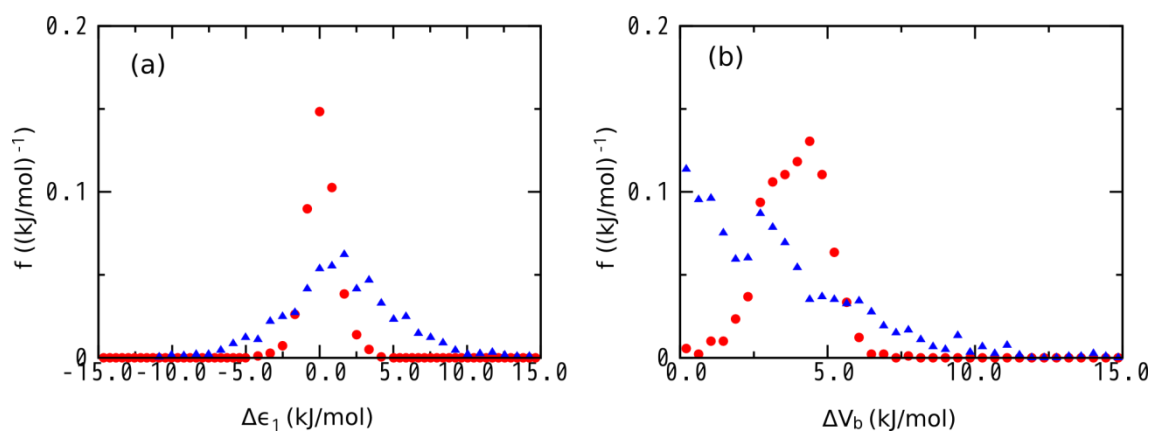


FIG. 6-10. Normalized probability density distribution of (a) the energy difference, $\Delta\epsilon_1 = \epsilon_1^{(\text{unocc})} - \epsilon_1^{(\text{occ})}$, between ZPEs in the two wells and (b) the barrier height, $\Delta V_b = V_0(q^\ddagger) - \epsilon_1^{(\text{occ})}$, from ZPE in the well of the occupied state for V_0 of the double-well shape. These were measured when the thermal activation reaction occurred in neon (red circle) and in water (blue triangle).

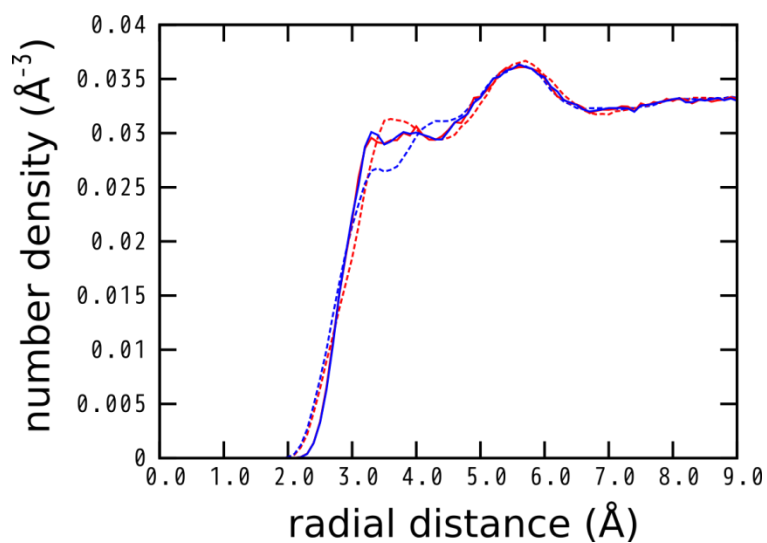


FIG. 6-11. Radial number densities of the oxygen atom of water as a function of the distance from the proton of malonaldehyde. Position of the proton is assumed to be at the most stable position in vacuum. The density observed from proton (red line) and from the position where the proton is going to transfer (blue line). Broken lines represent the density profile calculated for all trajectories including the ones when the tunneling reaction is not going to occur and solid lines represent the density profile when the reaction is going to occur.

VII. CONCLUSION

In order to figure out microscopic picture of proton transfer reaction in solution and its molecular mechanisms, a series of molecular dynamics calculation studies has been performed. First, an improved torsional force field of malonaldehyde has been presented. Then, using this force field, free energy surface has been calculated as a function of two dihedral angles by umbrella sampling method combined with molecular dynamics calculations. After then, mixed quantum-classical molecular dynamics calculations in water, a protic polar solvent, and in neon, non-polar solvent, have been carried out to investigate quantum and solvent effects on intramolecular proton transfer reaction.

In chapter III, two-dimensional conformational potential energy surface of *cis*-enol malonaldehyde was calculated based on *ab initio* molecular orbital method where cross terms of cosine functions have been added to conventional torsional potential function. Error of the potential energy surface by the extended force field from that by the *ab initio* calculation was much smaller than that by the conventional functions.

In chapter IV, conformational free energy surfaces of the *cis*-enol malonaldehyde in water have been evaluated as a function of two dihedral angles by MD calculations. The results show that solvation significantly influences the stability of rotamers and free energy barriers between two rotamers. However, the rotamer with intramolecular hydrogen bonding is still the most stable conformation among the rotamers in the *cis*-enol form both in water as well as in vacuum. It was also found that the rotamer with intramolecular hydrogen bonding is surrounded by the very high free energy barriers, at least 49.8 kJ/mol, which means that the rotamer can keep the structure much longer than the time scale of the proton transfer in water and the conformational change would not influence the proton transfer reaction.

In chapter V, quantum and solvent effects on intramolecular proton transfer reaction in

malonaldehyde in water has been investigated by applying mixed quantum-classical MD calculations method. From the trajectories, microscopic view for the reaction which utilizes thermal fluctuation by the solvent was presented. They show that barrier height and energy difference between the reactant and product wells were fluctuated by solute-solvent interactions, which are essential for the reaction. Then, the reaction was classified into three, i.e. tunneling reaction, thermal activation reaction, and barrier vanishing reaction and ratios of contribution of these reaction mechanisms were obtained. This clearly shows importance of the tunneling and thermal activation reactions. Comparing the result of the mix quantum-classical MD calculations with the quantum wave packet calculation in gas phase and the fully classical MD calculation in water, it was shown that the quantum and the solvent effects are great promoting the reaction. In particular, the thermal fluctuation caused by interaction with solvent, which is not found in the gas phase, plays an essential role in the reaction in water.

In chapter VI, in order to clarify solvent dependence of the intramolecular proton transfer reaction of malonaldehyde, simulations in neon have been carried out. The results were compared with those in water presented in chapter V, showing that quantum effects promotes the reaction rate in neon and that it was greater than that in water. This is mainly due to more frequently found tunneling reactions in neon than in water. Difference in the reaction mechanism between two solvents was discussed from the point of view of the shape of the potential energy curve along the reaction coordinate and its fluctuations. The difference was found to be significant. Great stabilization of the reactant well by water causes a large gap of the vibrational energy level between the reactant and product states. This results in a difficulty of the tunneling reaction compared with that in neon in which little stabilization is found. In contrast, the thermal activation and barrier vanishing reactions are greater in water than in neon with and without the quantum effect. This trend is from the strength of the solute-solvent interaction. The reactions are accelerated by the ZPE in

both solvents, showing the importance of quantum effect.

In this study, the proton transfer reaction occurs both in protic polar solvent and in non-polar solvent. When the reaction occurs, the energy difference between the vibrational ground state of the reactant state and the product state is nearly zero. That is to say, if this situation does not appear, proton transfer reaction is difficult to occur. From this study, the two factors which vary reactive potential curve are the stabilization of reactant state by solvation, e.g. dielectric constant, and the destabilization of reactant state by energy fluctuation.

In a series of the present studies, conformational stability of the hydrogen bonding structure of malonaldehyde in water and microscopic picture of the intramolecular proton transfer reaction in solutions have been clarified based on the molecular dynamics calculations. We hope that our research contributes to fundamental science and engineering such as molecular design of artificial biomolecules for information transportation and efficient energy production.

In this study, the intramolecular proton transfer reaction has been investigated. However, important proton transfer reactions are mainly intermolecular ones, e.g. the reaction in the fuel cell or in the proton pump. To investigate these reactions, improvement of the method is needed. For example, translation and rotation of the donor and acceptor molecules must be taken into account. Then, the transferring proton should be described in the Cartesian coordinate. Further, in the intermolecular proton transfer reactions, reactive pair may change as a function of time and one proton donor molecule, e.g. water, has a few candidates for the acceptor. These are subjects to be solved in the next step of the investigation.

ACKNOWLEDGEMENTS

I would like to show my greatest appreciation to Prof. S. Okazaki for his kindness and valuable discussion and guidance during the course of this work. I am also deeply grateful to Dr. A. Yamada for his helpful discussion and encouragement. I give my thanks to Dr. W. Shinoda, Dr. N. Yoshii, Dr. Y. Andoh, and Dr. K. Fujimoto for their encouragement and discussion. I want to thank all members of Okazaki group.

I thank the Center for Computational Sciences, the Supercomputer Center, the Institute for Solid State Physics, the University of Tokyo, the Research Institute for Information Technology, Kyushu University, and the Research Center for Computational Science, Okazaki, Japan, for the use of supercomputers.

APPENDIX

A. Equation of motion of mixed quantum-classical molecular dynamics

In the mixed quantum-classical approximation, degree of freedom, q , is treated quantum mechanically, while \mathbf{R} classical mechanically. Thus, q and p_q in Eq. (2-7) are operators, q and $-i\hbar \frac{\partial}{\partial q}$, respectively, whereas \mathbf{R} is dealt with a time dependent parameter, $\mathbf{R}(t)$ for the quantum system. This evolves following the classical equation of motion. Details of the calculation method have been described in Ref. [26,27].

Adiabatic potential energy curve of the solute in solution

$$V_0(q; \mathbf{R}(t)) = V_q^{eff}(q) + V_I(\mathbf{r}(q); \mathbf{R}(t)) \quad (1)$$

was divided into reactant potential, $V^R(q; \mathbf{R}(t))$, and product potential, $V^P(q; \mathbf{R}(t))$, every time step as shown in Fig. 2-1. Then, the vibrational eigen states in the reactant and product potential wells, $\{|\xi_n^{(R)}\rangle\}$ and $\{|\xi_n^{(P)}\rangle\}$, respectively, are obtained from

$$\left[-\frac{\hbar^2}{2} \frac{\partial^2}{\partial q^2} + V^R(q; \mathbf{R}(t)) \right] |\xi_n^{(R)}(q; \mathbf{R}(t))\rangle = \varepsilon_n^{(R)}(\mathbf{R}(t)) |\xi_n^{(R)}(q; \mathbf{R}(t))\rangle \quad (2)$$

$$\left[-\frac{\hbar^2}{2} \frac{\partial^2}{\partial q^2} + V^P(q; \mathbf{R}(t)) \right] |\xi_n^{(P)}(q; \mathbf{R}(t))\rangle = \varepsilon_n^{(P)}(\mathbf{R}(t)) |\xi_n^{(P)}(q; \mathbf{R}(t))\rangle, \quad (3)$$

respectively, where $\{\varepsilon_n^{(R)}\}$ and $\{\varepsilon_n^{(P)}\}$ are the n -th vibrational eigen energies in the reactant and product wells, respectively. The wave function may be expanded by the vibrational eigen functions in the reactant and product wells,

$$|\Psi(t, q; \mathbf{R}(t))\rangle = \sum_n C_n^{(R)}(t) |\xi_n^{(R)}(q; \mathbf{R}(t))\rangle + \sum_n C_n^{(P)}(t) |\xi_n^{(P)}(q; \mathbf{R}(t))\rangle, \quad (4)$$

where $C_n^{(R)}$ and $C_n^{(P)}$ are the expansion coefficients for the n -th vibrational state within the reactant well and the product one, respectively. Here, we must be careful that the eigen functions $|\xi_n^{(R)}\rangle$ and $|\xi_n^{(P)}\rangle$ are not normal to each other, this has been discussed in detail in Ref [26,27]. Substituting Eq.

(A-4) into the time-dependent Schrödinger equation, the equation of motion for the quantum system

is obtained by

$$i\hbar\dot{\mathbf{C}} = \mathbf{S}^{-1}[\mathbf{H} - i\hbar\mathbf{D}]\mathbf{C}, \quad (5)$$

where

$$\mathbf{C} = \begin{bmatrix} C_1^{(R)} \\ C_2^{(R)} \\ \vdots \\ C_1^{(P)} \\ C_2^{(P)} \\ \vdots \end{bmatrix}, \quad (6)$$

$$\mathbf{S} = \begin{bmatrix} \langle \xi_1^{(R)} | \xi_1^{(R)} \rangle & \langle \xi_1^{(R)} | \xi_2^{(R)} \rangle & \cdots & \langle \xi_1^{(R)} | \xi_1^{(P)} \rangle & \langle \xi_1^{(R)} | \xi_2^{(P)} \rangle & \cdots \\ \langle \xi_2^{(R)} | \xi_1^{(R)} \rangle & \langle \xi_2^{(R)} | \xi_2^{(R)} \rangle & \cdots & \langle \xi_2^{(R)} | \xi_1^{(P)} \rangle & \langle \xi_2^{(R)} | \xi_2^{(P)} \rangle & \cdots \\ \vdots & \vdots & \ddots & \vdots & \vdots & \ddots \\ \langle \xi_1^{(P)} | \xi_1^{(R)} \rangle & \langle \xi_1^{(P)} | \xi_2^{(R)} \rangle & \cdots & \langle \xi_1^{(P)} | \xi_1^{(P)} \rangle & \langle \xi_1^{(P)} | \xi_2^{(P)} \rangle & \cdots \\ \langle \xi_2^{(P)} | \xi_1^{(R)} \rangle & \langle \xi_2^{(P)} | \xi_2^{(R)} \rangle & \cdots & \langle \xi_2^{(P)} | \xi_1^{(P)} \rangle & \langle \xi_2^{(P)} | \xi_2^{(P)} \rangle & \cdots \\ \vdots & \vdots & \ddots & \vdots & \vdots & \ddots \end{bmatrix}, \quad (7)$$

$$\mathbf{H} = \begin{bmatrix} \langle \xi_1^{(R)} | H | \xi_1^{(R)} \rangle & \langle \xi_1^{(R)} | H | \xi_2^{(R)} \rangle & \cdots & \langle \xi_1^{(R)} | H | \xi_1^{(P)} \rangle & \langle \xi_1^{(R)} | H | \xi_2^{(P)} \rangle & \cdots \\ \langle \xi_2^{(R)} | H | \xi_1^{(R)} \rangle & \langle \xi_2^{(R)} | H | \xi_2^{(R)} \rangle & \cdots & \langle \xi_2^{(R)} | H | \xi_1^{(P)} \rangle & \langle \xi_2^{(R)} | H | \xi_2^{(P)} \rangle & \cdots \\ \vdots & \vdots & \ddots & \vdots & \vdots & \ddots \\ \langle \xi_1^{(P)} | H | \xi_1^{(R)} \rangle & \langle \xi_1^{(P)} | H | \xi_2^{(R)} \rangle & \cdots & \langle \xi_1^{(P)} | H | \xi_1^{(P)} \rangle & \langle \xi_1^{(P)} | H | \xi_2^{(P)} \rangle & \cdots \\ \langle \xi_2^{(P)} | H | \xi_1^{(R)} \rangle & \langle \xi_2^{(P)} | H | \xi_2^{(R)} \rangle & \cdots & \langle \xi_2^{(P)} | H | \xi_1^{(P)} \rangle & \langle \xi_2^{(P)} | H | \xi_2^{(P)} \rangle & \cdots \\ \vdots & \vdots & \ddots & \vdots & \vdots & \ddots \end{bmatrix}, \quad (8)$$

$$\mathbf{D} = \begin{bmatrix} \langle \xi_1^{(R)} | \dot{\xi}_1^{(R)} \rangle & \langle \xi_1^{(R)} | \dot{\xi}_2^{(R)} \rangle & \cdots & \langle \xi_1^{(R)} | \dot{\xi}_1^{(P)} \rangle & \langle \xi_1^{(R)} | \dot{\xi}_2^{(P)} \rangle & \cdots \\ \langle \xi_2^{(R)} | \dot{\xi}_1^{(R)} \rangle & \langle \xi_2^{(R)} | \dot{\xi}_2^{(R)} \rangle & \cdots & \langle \xi_2^{(R)} | \dot{\xi}_1^{(P)} \rangle & \langle \xi_2^{(R)} | \dot{\xi}_2^{(P)} \rangle & \cdots \\ \vdots & \vdots & \ddots & \vdots & \vdots & \ddots \\ \langle \xi_1^{(P)} | \dot{\xi}_1^{(R)} \rangle & \langle \xi_1^{(P)} | \dot{\xi}_2^{(R)} \rangle & \cdots & \langle \xi_1^{(P)} | \dot{\xi}_1^{(P)} \rangle & \langle \xi_1^{(P)} | \dot{\xi}_2^{(P)} \rangle & \cdots \\ \langle \xi_2^{(P)} | \dot{\xi}_1^{(R)} \rangle & \langle \xi_2^{(P)} | \dot{\xi}_2^{(R)} \rangle & \cdots & \langle \xi_2^{(P)} | \dot{\xi}_1^{(P)} \rangle & \langle \xi_2^{(P)} | \dot{\xi}_2^{(P)} \rangle & \cdots \\ \vdots & \vdots & \ddots & \vdots & \vdots & \ddots \end{bmatrix}. \quad (9)$$

The Newtonian equation of motion

$$m_j \frac{d^2 \mathbf{R}_j}{dt^2} = \mathbf{F}_j \quad (10)$$

is solved to obtain the trajectory of the classical system, where m_j and \mathbf{R}_j represent the mass and position vector of the j -th classical atom, respectively, and \mathbf{F}_j denotes the force on the j -th atom.

Since interaction between the quantum and classical systems is described by the surface-hopping approximation, force on the classical atom j is given by Hellmann-Feynman force from a specified vibrational state of the quantum system, that is, when the quantum system is in the state k in the reactant well,

$$\mathbf{F}_j = - \left\langle \xi_k^{(R)} \left| \frac{\partial V_I}{\partial \mathbf{R}_i} \right| \xi_k^{(R)} \right\rangle - \frac{\partial V_S}{\partial \mathbf{R}_i}, \quad (11)$$

where the first term of the right hand side is the force from the quantum system, and the second term is the force from the classical solvent. The transition from the current state to the other is decided by the transition probability obtained from Eq. (A-5) and a random number according to the fewest-switches algorithm.

B. Potential model

1. Effective one-dimensional potential energy curve of solute

In order to obtain effective one-dimensional potential of the solute molecule $V_0^{eff}(q)$ in Eq. (2-8), we used *ab initio* calculation data of $V_0^q(q)$ and Hessian matrices along the IRC at the MP2/6-31g** level by Yagi *et. al.*[32]. Normal modes perpendicular to q were integrated out assuming that the motion of the normal modes is fast, that is, ZPEs were added to $V_0^q(q)$. This is reasonable because the wave number of the normal modes perpendicular to q , ranges from 280 cm^{-1} to 3560 cm^{-1} , which is greater than that of q , 280 cm^{-1} , around the stable point. The one-dimensional effective potential energy curve was smoothed by the least-square fitting to Morse function in the empirical valence bond model. A constant coupling was assumed in the q region between the saddle point and the stable point and a quadratic function was used in the outer region from the stable point.

Figure 2-2 shows $V_0^q(q)$ by Yagi et al. [32] and the calculated $V_0^{eff}(q)$. Potential barrier height of $V_0^{eff}(q)$ was 6.3 kJ/mol after adding ZPEs, which is significantly lower than that of the original $V_0^q(q)$, 15.1 kJ/mol. The minimum value of $V_0^q(q)$ without ZPEs correction is presented at $q = \pm 0.87 \text{ \AA}(\text{g/mol})^{1/2}$, whereas it is shifted to $q = \pm 0.80 \text{ \AA}(\text{g/mol})^{1/2}$ after the ZPEs correction. The calculated wave number at the stable point of $V_0^{eff}(q)$ is about 250 cm^{-1} . Motion of malonaldehyde molecule along q is a closing motion of the two oxygen atoms from $q = \pm 0.87$ to $q = \pm 0.2 \text{ \AA}(\text{g/mol})^{1/2}$ [32], which is followed by proton transfer between the two oxygen atoms from $q = \pm 0.2$ to $0 \text{ \AA}(\text{g/mol})^{1/2}$. Then, large vibrational energy of O-H stretching mode is dominant in the ZPEs of the normal modes perpendicular to q near the minimum position. In contrast, near the barrier top, energy of the O...O vibrational motion is included in the ZPE instead of the O-H stretching mode. These are the main origin which lowers the barrier of $V_0^q(q)$.

One-dimensional IRC was adopted in the present study, integrating out all other solute degrees of freedom. However, semi-classical calculations of tunneling transfer of malonaldehyde in vacuum at 0 K showed that the IRC did not reproduce the tunneling splitting and that the tunneling occurs along the other path in full dimensional space of malonaldehyde [32,35]. In fact, value of tunneling splitting for our potential model, $V_0^{eff}(q)$, is 3.4 cm^{-1} , whereas the values taking account of the multi-dimensionality using the potential model by Yagi *et al.* [32] is in the range of $13.9 - 30.7 \text{ cm}^{-1}$ [32,35,37]. The latter is closer to the experimental value, 21.6 cm^{-1} [28,29], than our model using the IRC. The difference between our model and the multi-dimensional calculations is $10 - 27 \text{ cm}^{-1}$. This indicates that our model includes an error of this order for the tunneling rate at 0 K for the isolated solute molecule. Potential energy surface in solution changes significantly by the solute-solvent interactions. In fact, as shown later, most frequently observed shape of the potential energy curve in solution is asymmetric double well. This is caused by the stabilization of the reactant well by solvation. When the potential curve is asymmetric, tunneling reaction scarcely occurs

because vibrational energy level is different between the reactant and product wells. The reaction occurs only when the vibrational energy level is close to each other and the barrier height is low as discussed later. The condition is satisfied only occasionally in the trajectory by thermal fluctuation of the solvent. This is the main rate-determining process for the tunneling reaction. On the other hand, considering thermal activation reaction, a model based on the IRC is reasonable. The use of the IRC is a popular choice of practical use due to its simplicity [50].

2. Solute-solvent and solvent-solvent interactions

The Coulomb and LJ interaction parameters of the solute molecule depend much on q . In order to evaluate partial charges on the reacting solute atoms, quantum chemical calculations have been done at the MP2/6-31G** level [51], where ESP point charges were obtained for the solute atoms as a function of q . Smoothed point charge values by a Gaussian window function along q are used in our simulation. With respect to the LJ interaction parameters, OPLS-aa force field parameters [52-55] were used. Linear q dependence of the parameters was assumed between the stable points in the reactant and product wells.

Now, validity of the present model may be examined comparing free energy barrier of intramolecular proton transfer reaction of malonaldehyde in water based on the present model with that calculated by umbrella sampling method using *ab initio* MD based on DFT/B3LYP, 8.8 kJ/mol [63]. The free energy barrier using our force field model was calculated from the distribution of the system along q which was obtained by classical MD simulation, where the full dimensional model of the solute potential function was adopted. This is the same condition with the *ab initio* MD calculation. In our calculation, flexible-SPC model [64,65] with the intramolecular vibrational degrees of freedom is adopted for water molecule. The calculated free energy barrier for the present model was 11.9 kJ/mol. The difference is 3.1 kJ/mol between the two calculations, indicating good

agreement between them. Calculated potential barriers reported by various *ab initio* quantum chemical calculations are different from each other by the order of 10 kJ/mol depending on the methods [68], indicating that the error of our solute-solvent force field model is within the error among the *ab initio* calculations.

C. Division of potential energy curve into reactant and product wells

1. Recipe of the division V_0 into V^R and V^P

Shape of the adiabatic potential energy curve in solution, V_0 , fluctuates by the interaction with the solvent. Three typical shapes of V_0 found in the solution are shown in Figs. 2-3(a), (b), and (c). From these V_0 's, the reactant potential V^R and the product one V^P were obtained as follows (detail of the procedure is given later). First, V_0 was divided at the top of the barrier, i.e. the transition state, into two portions. Each potential curve was further divided into region near the top of the barrier and the other region. The region on the transition state side was fitted to a Morse potential and that on the opposite side to a harmonic potential. For the potential curve shown in Fig. 2-3(a), V^R and V^P were fitted such that (1) each oscillator in V^R and V^P reproduces low-energy vibration in the well of the original adiabatic potential, that (2) wave functions of the excited states in the reactant and product wells must overlap sufficiently with each other at high energy region above the barrier so that transition between the states occur very frequently, and that (3) high energy states above the barrier can be regarded as transient in the reaction process so that we do not care about the detail of the vibrational state in this region [27]. In the case of the single-well potential without barrier as shown in Fig. 2-3(b), the low-energy vibration in the left well must satisfy (1) and the high-energy vibration in the right and left wells must satisfy (2) and (3). Since, in the case of the right well in Fig. 2-3(b) and the right and left wells in Fig. 2-3(c), vibrational states cannot be defined clearly, they may be considered to be transient. We do not care much about them though they

are formally obtained because of the requirement of calculation.

2. Detail of the procedure of the division

First, symbols should be defined to explain the procedure. Tentative border separating the reactant and product wells, q^\ddagger , is defined first. q^\ddagger is the coordinate at the barrier top in the case of double-well potential (see Fig. 2-3(a)). Note q^\ddagger is different from the position of the effective barrier, q^\ddagger , shown as vertical dotted lines in Fig. 2-3. In the case of single-well potential that has a well in one side while no well in the other side (see Fig. 2-3(b)), q^\ddagger is given by two inflection points, whereas q^\ddagger is not given for the case of the single-well potential (see Fig. 2-3(c)). The stable points in the reactant well and the product one in V_0 are denoted by q^R and q^P , respectively ($q^R < q < q^P$) when they are found.

Next, we describe a procedure for the three cases (i), (ii) and (iii) depending on the depth of the reactant potential well, $\Delta V^\ddagger (= V_0(q^\ddagger) - V_0(q^R))$. Then, as described above, the definition of the reactant or product potential wells above the barrier given by the dotted lines in Figs. 2-3(a), (b), and (c) is not important because these regions correspond to the transient states of reaction given by the gray lines in Figs. 2-3(a), (b), and (c). Much effort was not made for this, even if they include some arbitrariness.

(i) In the case of the deep potential well ($\Delta V^\ddagger > 1.2$ kcal/mol (5.0 kJ/mol)) such as the wells shown in Fig. 2-3(a) and the left well in Fig. 2-3(b), V^R , for example, is equal to V_0 for $q < q'$, where q' is the point which divides the distance between q^R and q^\ddagger in the ratio of 3:1 according to the condition (1) shown in Sec.II.2-4. For $q \geq q'$, applying the condition (2), Morse function, $V^R = D(1 - \exp(-\alpha(q - q^R)))^2 + V_0(q^R)$, is adopted to describe V^R for large q , where the curvature, α , and the depth, D , are chosen to connect V^R smoothly at q' . Then, according to the condition (3), high energy region above the barrier is described by extension of the

Morse function. Vibrational state in this energy region is regarded as transient state.

(ii) When the well is shallow (in the case that the value of D obtained in (i) is small), the vibrational energy levels do not exist within the well. Then, the connecting point, q' , is shifted to the point which satisfies $D > D_{low}$, where $D_{low} = \Delta V^\ddagger + 5$ kcal/mol (21 kJ/mol). However, when ΔV^\ddagger is small, too, no q' which satisfies $D > D_{low}$ is found. In this case ($5.0 \geq \Delta V^\ddagger > 0.21$ kJ/mol), V^R is equal to V_0 for $q < q^R$, and Morse function whose the well depth is D_{low} is used for $q \geq q^R$. The value of α is chosen to obtain a good fit of V^R to V_0 for $q^R < q < q'$.

(iii) In the case that there is no barrier ($0.21 \geq \Delta V^\ddagger > 0$ kJ/mol) or that the potential well does not exist (see the right hand side of Fig. 2-3(b) and Fig. 2-3(c)), V^R must be given from the shape of V_0 even if q^R does not exist. Then, defining q'' to be the most flat position on the reactant side in V_0 , V^R is given equal to V_0 for $q < q''$. In the range of $q \geq q''$, V^R is extrapolated from $q = q''$ using a quadratic function. Morse function with $D = D_{low}$ is adopted for $q \geq q^R$, where α is chosen to connect V^R at $q = q^R$ with continuous curvature. However, in order to avoid delocalized vibrational states due to wide V^R , a lower limit value of α , which satisfies that $V^R(q^P) = V_0(q^\ddagger) + 1.5$ kcal/mol, is used instead of a smaller value of α in all cases of (i),(ii) and (iii). Some values which appear in the above procedure were determined by trial and error such that the divided potential energy curve, for example, V^R fits well to the original V_0 and, at the same time, shows smooth line as a function of q . The procedure to obtain V^P is the same as that for V^R .

TABLE A-1. Summary of the definition of state, type of adiabatic potential energy curve V_0 , definition of the reaction and reaction mechanism. Details are described in Section II.4.

		Definition
State	Reactant state and product state	Vibrational state whose energy level is lower than the barrier top.
	Transient state	Vibrational state whose energy level is higher than the barrier top
(Examples are illustrated in Figs. 2-3 and 2-4 in blue and red for the reactant and product states, respectively, and in gray for the transient state)		
Type of V_0	Double-well	Potential curve with a barrier higher than ZPE for QCMD and $kT/2$ for FCMD (see Figs. 2-3(a) and 2-4(a))
	Strongly-asymmetric-single-well	Potential curve without a barrier higher than the above threshold, while one side has a well deeper than the threshold.(see Figs. 2-3(b) and 2-4(b))
	Quasi-symmetric-single-well	Potential curve without a barrier higher than the above threshold, where no deep well is found for each sides. (see Figs. 2-3(c) and 2-4(c))
Reaction		Transition between reactant and product states. Recrossing within 150 fs is not regarded as reaction. (see also subsections V C 2-2 and VI C 3-1)
Reaction mechanism	Tunneling reaction	Direct transition from the reactant state to the product one below the barrier of double-well potential.
	Thermal activation reaction	Transition from reactant state to the product one via the transient state over a barrier higher than the above threshold.
	Barrier vanishing reaction	Transition from reactant state to the product one via the transient state without a barrier or with a barrier lower than the above threshold.

REFERENCES

- [1] D. L. Nelson and M. M. Cox, *Lehninger Principles of Biochemistry 3rd ed.*, (Worth, New York, 2000).
- [2] K.-D. Kreuer, *Proton Conduction in Fuel Cells*. In *Hydrogen-Transfer Reactions*, J. T. Hynes, J. P. Klinman, H. H. Limbach, R. L. Schowen (Eds.), (WILEY-VCH, 2007), Vol. 2, 709-736.
- [3] G. S.-Yfrach, P. A. Liddell, S.-C. Hung, A. L. Moore, D. Gust and T. A. Moore, *Nature* **385**, 239 (1997).
- [4] X. Xie, G. A. Crespo, G. Mistlberger and E. Bakker, *Nature Chem.* **6**, **202** (2014).
- [5] S. Glasstone, K. J. Laidler and H. Eyring, *The Theory of Rate Process; the kinetics of chemical reactions, viscosity, diffusion and electrochemical phenomena*. London: MacGraw-Hill Book Company, Inc. 1964.
- [6] A. Nitzan, *Chemical Dynamics in Condensed Phases*, Oxford: Oxford University Press, 2007.
- [7] J. Gao and D. G. Truhlar, *Annu. Rev. Phys. Chem.* **53**, 467 (2002).
- [8] D. G. Truhlar and Bruce C. Garrett, *Hydrogen-Transfer Reactions*, ed. J. T. Hynes, J. P. Klinman, H. H. Limbach, R. L. Schowen (WILEY-VCH, 2007), Vol. 2, p. 833.
- [9] K.-Y. Wong and J. Gao, *J. Chem. Phys.* **127**, 211103 (2007).
- [10] K.-Y. Wong and J. Gao, *J. Chem. Theo. Comp.* **4**, 1409 (2008).
- [11] J. T. Hynes, J. P. Klinman, H.-H. Limbach, and R. L. Schowen, *Hydrogen-Transfer Reactions*, (WILEY-VCH, 2007), Vol. 1.
- [12] J. P. Bergsma, J. R. Reimers, K. R. Wilson and J. T. Hynes, *J. Chem. Phys.* **85**, 5625 (1986).
- [13] J. P. Bergsma, B. J. Gertner, K. R. Wilson and J. T. Hynes, *J. Chem. Phys.* **86**, 1356 (1987).
- [14] B. J. Gertner, R. M. Whitnell, K. R. Wilson and J. T. Hynes, *J. Am. Chem. Soc.* **113**, 74 (1991).
- [15] P. L. Geissler, C. Dellago, D. Chandler, J. Hutter and M. Parrinello, *Science* **291**, 2121 (2001).
- [16] A. Furuhashi, M. Dupuis and K. Hirao, *Phys. Chem. Chem. Phys.* **10**, 2033 (2008).
- [17] M. Sato, H. Yamataka, Y. Komeiji, Y. Mochizuki, T. Ishikawa and T. Nakano, *J. Am. Chem. Soc.* **130**, 2396 (2008).
- [18] R. Car and M. Parrinello, *Phys. Rev. Lett.* **55**, 2471 (1985).
- [19] P. Bala, B. Lesyng and J. A. McCammon, *Chem. Phys.* **180**, 271 (1994).

- [20] P. Bala, P. Grochowski, B. Lesyng and J. A. McCammon, *J. Phys. Chem.* **100**, 2535 (1996).
- [21] P. Bala, P. Grochowski, K. Nowiński, B. Lesyng and J. A. McCammon, *Biophys. J.* **79**, 1253 (2000).
- [22] D. Borgis, G. Tarjus and H. Azzouz, *J. Chem. Phys.* **97**, 1390 (1992).
- [23] D. Borgis, G. Tarjus and H. Azzouz, *J. Phys. Chem.* **96**, 3188 (1992).
- [24] S. Hammes-Schiffer, J. C. Tully, *J. Chem. Phys.* **101**, 4657 (1994).
- [25] S. Hammes-Schiffer, J. C. Tully, *J. Phys. Chem.* **99**, 5793 (1995).
- [26] A. Yamada and S. Okazaki, *J. Chem. Phys.* **124**, 094110 (2006).
- [27] A. Yamada and S. Okazaki, *J. Chem. Phys.* **128**, 044507 (2008).
- [28] W. F. Rowe, Jr., R. W. Duerst and E. B. Wilson, *J. Am. Chem. Soc.* **98**, 4021 (1976).
- [29] T. Baba, T. Tanaka, I. Morino, K. M. T. Yamada and K. Tanaka, *J. Chem. Phys.* **110**, 4131 (1999).
- [30] P. Schuster, *Chem. Phys. Lett.* **3**, 433 (1969).
- [31] J. Bicerano, H. F. Schaefer III and W. H. Miller, *J. Am. Chem. Soc.* **105**, 2550 (1983). [32] K. Yagi, T. Taketsugu and K. Hirao, *J. Chem. Phys.* **115**, 10647 (2001).
- [33] E. Bosch, M. Moreno and J. M. Lluch, *Chem. Phys.* **159**, 99 (1992).
- [34] T. D. Sewell, Y. Guo and D. L. Thompson, *J. Chem. Phys.* **103**, 8557 (1995).
- [35] G. V. Mil'nikov, K. Yagi, T. Taketsugu, H. Nakamura and K. Hirao, *J. Chem. Phys.* **120**, 5036 (2004).
- [36] Y. Wang, B. J. Braams, J. M. Bowman, S. Carter and D. P. Tew, *J. Chem. Phys.* **128**, 224314 (2008).
- [37] M. D. Coutinho-Neto, A. Viel and U. Manthe, *J. Chem. Phys.* **121**, 9207 (2004).
- [38] K. Wolf, W. Mikenda, E. Nusterer, K. Schwarz and C. Ulbricht, *Chem. Eur. J.* **4**, 1418 (1998).
- [39] K. Wolf, W. Mikenda, E. Nusterer and K. Schwarz, *J. Mol. Struct.* **448**, 201 (1998).
- [40] L. Walewski, P. Bala, M. Elstner, Th. Frauenheim and B. Lesyng, *Chem. Phys. Lett.* **397**, 451 (2004).
- [41] Y. Yang and M. Meuwly, *J. Chem. Phys.* **133**, 064503 (2010).
- [42] S. H. Bertz and G. Dabbagh, *J. Org. Chem.* **55**, 5161 (1990).
- [43] S. Yamabe, N. Tsuchida and K. Miyajima, *J. Phys. Chem. A.* **108**, 2750 (2004).

- [44] G. Buemi, Chem. Phys. **277**, 241 (2002).
- [45] K. S. Peters and G. Kim, J. Phys. Chem. A **108**, 2598 (2004).
- [46] K. S. Peters, *Acc. Chem. Res.* **42**, 89 (2009).
- [47] D. Frenkel and B. Smit, *Understanding Molecular Simulation: From Algorithms to Applications*, 2nd ed. (Academic Press, New York, 2002).
- [48] W. H. Miller, N. C. Handy and J. E. Adams, J. Chem. Phys. **72**, 99 (1980).
- [49] S. Kato and K. Morokuma, J. Chem. Phys. **73**, 3900 (1980).
- [50] J. T. Hynes, J. P. Klinman, H.-H. Limbach, and R. L. Schowen, *Hydrogen-Transfer Reactions* (WILEY-VCH, 2007), Vol. 2.
- [51] M. J. Frisch, G. W. Trucks, H. B. Schlegel *et al.*, Gaussian 03, Revision E.01, Gaussian, Inc., Wallingford CT, (2004).
- [52] W. L. Jorgensen and J. Tirado-Rives, J. Am. Chem. Soc. **110**, 1657 (1988).
- [53] W. L. Jorgensen, D. S. Maxwell and J. Tirado-Rives, J. Am. Chem. Soc. **118**, 11225 (1996).
- [54] N. A. McDonald and W. L. Jorgensen, J. Phys. Chem. B **102**, 8049 (1998).
- [55] W. L. Jorgensen and N. A. McDonald, J. Mol. Struct. (Theochem) **424**, 145 (1998).
- [56] V. B. Delchev and G. S. Nikolov, Monatsh. Chem. **131**, 107 (2000).
- [57] V. B. Delchev and H. Mikosch, Monatsh. Chem. **132**, 223 (2001).
- [58] G. Buemi and F. Zuccarello, J. Mol. Struct. **581**, 71 (2002).
- [59] M. J. Frisch, G. W. Trucks, H. B. Schlegel *et al.*, Gaussian 03, Revision D.01, Gaussian, Inc., Wallingford CT, (2004).
- [60] J. Wang, P. Cieplak, P. A. Kollman, J. Comp. Chem. **21**, 1049 (2000).
- [61] G. J. Martyna, M. E. Tuckerman, D. J. Tobias, and M. L. Klein, Mol. Phys. **87**, 1117 (1996).
- [62] G. J. Martyna, D. J. Tobias and M. L. Klein, J. Chem. Phys. **101**, 4177 (1994).
- [63] Y. Mori and Y. Okamoto, Phys. Rev. E **87**, 023301 (2013).
- [64] O. Teleman, B. Jonsson and S. Engstrom, Mol. Phys. **60**, 193 (1987).
- [65] A. Wallqvist and O. Teleman, Mol. Phys. **74**, 515 (1991).
- [66] J. O. Hirschfelder, C. F. Curtiss and R. B. Bird, *Molecular Theory of Gases and Liquids*, John Wiley, New York (1964).
- [67] R. C. Weast (Ed.), *CRC Handbook of Chemistry and Physics*, 90th ed., (CRC Press, 2009).

[68] G. V. Mil'nikov and H. Nakamura, *Phys. Chem. Chem. Phys.* **10**, 1374 (2008).

LIST OF PUBLICATIONS

Chapter III

An improved torsional force field for cis-enol malonaldehyde

Y. Kurokawa, H. Kojima, A. Yamada and S. Okazaki, Mol. Simul. **38**, 442-447(2012).

Chapter IV

Free energy surface for rotamers of cis-enol malonaldehyde in aqueous solution studied by molecular dynamics calculations

H. Kojima, A. Yamada and S. Okazaki, Mol. Simul., in press.

Chapter V

A molecular dynamics study of intramolecular proton transfer reaction of malonaldehyde in solutions based upon mixed quantum-classical approximation. I. Proton transfer reaction in water

A. Yamada, H. Kojima and S. Okazaki, J. Chem. Phys. **141**, 084509 (2014).

Chapter VI

A molecular dynamics study of intramolecular proton transfer reaction of malonaldehyde in solutions based upon mixed quantum-classical approximation. II. Proton transfer reaction in non-polar solvent.

H. Kojima, A. Yamada and S. Okazaki, submitted.

Other publications

MODYLAS: A highly parallelized general-purpose molecular dynamics simulation program for large-scale systems with long-range forces calculated by fast multipole method (FMM) and highly scalable fine-grained new parallel processing algorithms

Y. Andoh, N. Yoshii, K. Fujimoto, K. Mizutani, H. Kojima, A. Yamada, S. Okazaki, K. Kawaguchi, H. Nagao, K. Iwahashi, F. Mizutani, K. Minami, S. Ichikawa, H. Komatsu, S. Ishizuki, Y. Takeda, and M. Fukushima, J.Chem. Theory and Com., **9**, 7, 3201-3209 (2013).

All-atom molecular dynamics calculation study of entire poliovirus empty capsids in solution

Y. Andoh, N. Yoshii, A. Yamada, K. Fujimoto, H. Kojima, K. Mizutani, A. Nakagawa A. Nomoto, and S. Okazaki, J. Chem. Phys. **141**, 165101 (2014).

MODYLAS: A Highly Parallelized General-Purpose Molecular Dynamics Simulation Program

N. Yoshii, Y. Andoh, K. Fujimoto, H. Kojima, A. Yamada, and S. Okazaki, submitted.